博士論文

Evaluation of Multi-Terminal VSC HVDC Systems by Stability Constrained Optimal Power Flow in a Power System with Large-Scale Wind Power Plants

（大規模風力連系電力系統における安定性制約を考慮した最適潮流計算による多端子自励式直流送電システムの評価）

37-177079
Sangwon Kim
金 相源

Advisor: Professor Akihiko Yokoyama

A dissertation submitted in partial fulfillment of the requirements
of the degree of Doctor of Philosophy in the
Graduate School of Engineering, the University of Tokyo,

November 29th, 2019

ACKNOWLEDGEMENTS

I would like to express my deep appreciation and gratitude sincerely to my advisor, Professor Akihiko Yokoyama for his guidance, invaluable encouragement and support throughout my doctorate course. It has been the great pleasure and honor for me to complete this research under his supervision.

Furthermore, I would like to share this honor with Professor Yasumasa Fujii, Professor Jumpei Baba, Professor Akiko Kumada, and Professor Takafumi Koseki, the committee of my Ph.D. dissertation. Without their kind suggestions and comments, this research definitely cannot be accomplished.

Moreover, I also would like to express my sincere appreciation to Mr. Takaguchi, Dr. Takano, and Dr. Mori who are belong to the Advanced Technology R&D Center in Mitsubishi Electric Corporation for their kind and detailed comments on this research. In addition, I would like to thank Professor Yoshio Izui in Engineering Department of Electrical and Electronic Engineering, Kanazawa Institute of Technology for his tremendous help for constructing the directions of this research.

I deeply thank to Mr. Norihito Shimada and the members in Yokoyama laboratory for their assistance, support, and advice during my doctorate course. Besides, the helpful and kind advice from all staff members of the office of Department of electrical engineering, Faculty of Engineering has been inevitable in finishing this research. I cannot help expressing my gratitude to all their supports as well.

I am highly indebted to all members of The Tokyu Foundation, The Iwatani Naoji Foundation in Japan, and Siebel Scholars Foundation in USA who have kindly supported my whole life during my doctorate course. It is definitely no exaggeration to mention that this accomplishment is composed of the supports from all of them.

Finally, I am sincerely grateful to all my beloved family members: parents, sister, grandparents, and the others for their continuous encouragement during my study in Japan.

Sangwon Kim

Tokyo

November 2019

OUTLINE

LIST OF FIGURES

LIST OF TABLES

1. Introduction

1.1 General Introduction

Currently, the installations of renewable energy sources (RES) such as photovoltaics and wind turbines are being discussed as significant global issues in many power systems. In this context, the power system operators and government in Japan are also aiming to increase the roll of RES sources. As regards the utilizations of large-scale wind power plants, the distances between the wind source areas and large-demand areas are not close, above several hundred kilometers in many scenarios. Hence, the necessity of long-distance transmission has been investigated in such cases. For instance, the scenario of long-distance transmission from the wind power sources in North Sea towards large-demand South areas in Germany is suggested.

The power systems in Japan also confront similar issues. According to 2050, up to 75GW of wind power plant facilities will be installed until 2050 in Japan. However, most of wind energy is concentrated in North-East areas in which the power consumption is relatively low. Therefore, some of the produced wind power cannot be consumed only in the local areas if large-scale wind power plants are installed in power systems in Japan. The necessity of long-distance large-scale wind power transmission from the high wind potential areas towards the large-demand areas has been surveyed in this context.

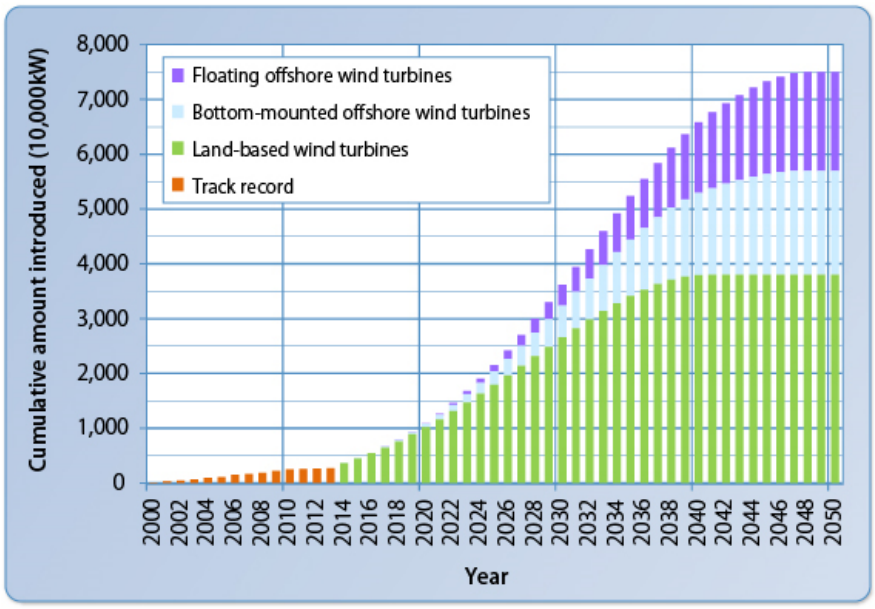

Fig. 1.1. Roadmap of the introduction of wind power in Japan [1]

It should be noted that the following critical problems emerge in case of a large amount of long-distance wind power transmission in Japan. For starters, considering the fluctuation of wind power output and low capacity factors of wind power plants in Japan, the economic benefit of the wind power transmission system is expected not to be high. Moreover, the long-distance large-scale power transmission from the high wind potential areas towards the large-demand areas in Japan is strictly limited due to power system rotor-angle stability issues of the existing AC systems.

From these points of view, high-voltage direct current (HVDC) systems have many advantages over conventional AC transmission systems. It is well-known that in cases of long-distance transmission, HVDC transmission systems are more effective than conventional AC transmission systems considering the following points.

- Low transmission losses (no skin effect)
- No reactive power compensation
- Less stability constraints (no rotor-angle stability, no frequency stability)
- Flexible active power control
- System stabilization effects by HVDC converter control systems

Recently, two types: line-commutated converter (LCC) HVDC and voltage-source converter (VSC) HVDC systems are utilized in general. The comparison between LCC HVDC and VSC HVDC systems are summarized in Table 1.1 [2].

Mostly, thyristors are used as the switching devices of LCC HVDC systems for the recent several decades. Compared to VSC type, the switching losses of LCC based HVDC systems are negligible. Significant harmonics components are produced by switching process. In order to remove these components, AC filters are required for LCC HVDC systems. As a consequence, converter station sizes of LCC HVDC systems are larger than those of VSC HVDC systems in general. Active power reversal is possible by changing the polarity of DC voltage in LCC HVDC systems. Without any external power supply from AC grid sides, it is difficult to utilize black start capability with LCC HVDC systems. The LCC type is superior for DC overhead transmission systems since in cases of a temporary DC fault occurrence, DC voltage can be controlled in a low value to restrain DC fault current. LCC HVDC systems have possibilities of commutation failures if severe AC grid voltage fluctuations are observed. For this reason, LCC HVDC systems have difficulties to be used for weak AC systems. Multi-terminal configurations using the LCC technology are possible, but the flexibility of power flow control is limited compared to multi-terminal VSC HVDC (MTDC) systems.

The utilization of VSC technology for HVDC transmission systems has been proposed since the late 1990s. As the first stage, two-level VSC HVDC systems are discussed and nowadays, modular-multilevel converter (MMC) HVDC systems using many sub-modules are also attracting considerable attention due to outstanding characteristics. IGBT-based switching devices are adopted for VSC HVDC systems. The switching losses of the VSC type are higher than those of LCC type but still less than 1% of losses can be obtained with MMC technology. Less harmonics components emerge by VSC HVDC, using MMC technology in particular. Therefore, the size of AC filter can be reduced or omitted, thus the converter station size can also be decreased. The

direction of active power can be controlled by changing DC current direction. One of the most important advantages of the VSC type over the LCC type is the independent active and reactive power output controllability. Thanks to this characteristic, VSC HVDC systems can also be adopted in weak AC systems exposed to severe AC voltage fluctuations. Compared to LCC HVDC systems, more flexible power flow controls are allowed using multi-terminal VSC HVDC systems.

Table 1.1. Comparison between HVDC systems with LCC and VSC types [2]

	LCC type	***VSC type***
Switching device	Thyristor	(enhanced) IGBT
Switching losses	Negligible	Low (less than 1%)
Station size	Large (with filter station)	Small (around 50% of LCC type)
AC filters	Large	Small or No
Active power reversal	DC voltage polarity reversal, within 0.5 – 1 s	DC current direction reversal, within 0.1 s
Independent active and reactive power control	No	Yes
Black start	Difficult	Yes
Control response time	0.1 – 0.2 s	0.03 – 0.05 s
Overhead transmission	Yes	Yes (DC circuit breakers may be required)
Commutation failure	Yes	No
Capability to supply weak AC system	Limited (additional reactive power control system is required)	Yes
Multi-terminal operation	Limited	Flexible

Multi-terminal VSC HVDC topologies

Several representative multi-terminal topologies are explained [3]. Novel topologies other than these configurations for offshore wind power plant integrations have been discussed in [4].

One of the radial topologies in Fig. 1.2 can be easily extended from point-to-point VSC HVDC systems by adding interconnection transmission lines. In case of a DC fault occurrence, the faulted parts can be separated from the whole DC grid using DC circuit breakers. In general, DC circuit breakers are installed at the both ends of each DC transmission line.

In the star topology described in Fig. 1.3, all VSC converters are interconnected through the DC switching station. The DC switching station refers to the node at which DC transmission lines, DC circuit breakers, isolators, and no VSC converters are installed. Similar to the radial topology, DC circuit breakers are required at the both ends of each DC transmission line. One of the drawbacks of this star topology is that the impact of a DC fault at the DC switching station is critical since all DC transmission lines are affected by the fault.

A simple meshed topology is illustrated in Fig. 1.4. Other meshed topologies with more DC transmission lines than the system in Fig. 1.4 can also be configured. Meshed multi-terminal topologies can enhance the reliability and economic operations of HVDC systems. Instead, additional costs for the increased numbers of DC transmission lines and DC circuit breakers are required.

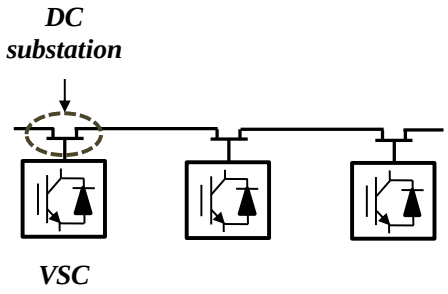

Fig. 1.2. Radial topology [3]

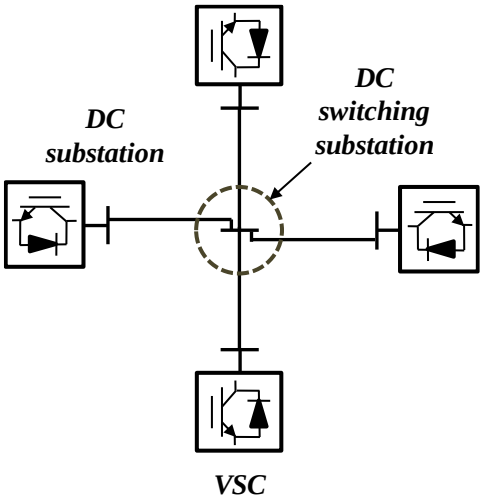

Fig. 1.3. Star topology [3]

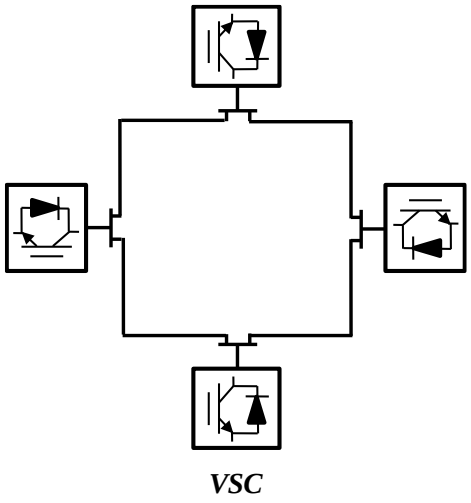

Fig. 1.4. Meshed topology [3]

Configurations of VSC stations

The basic configurations of VSC stations; asymmetrical monopole, symmetrical monopole, and bi-pole configurations are explained [3], [5]. Even though the configurations for point-to-point VSC HVDC systems are illustrated from Fig. 1.5 to Fig. 1.7 for the simplicity, these configurations can also be applied to multi-terminal VSC HVDC systems as plotted from Fig. 1.8 to Fig. 1.10. The symbol 'G' indicates the possible grounding locations of VSC HVDC systems [3].

One DC transmission line and one neutral conductors are required for the asymmetrical monopole configuration in Fig. 1.5. Regarding the neutral conductor, fully-rated load current capacity is necessary to form a complete current path. However, the insulation level of it does not have to be as strong as that of the DC transmission line [3]. The nominal voltage of the positive pole V_n is equal to that of VSC converter. When a pole-to-ground fault occurs, the steady-state post-fault DC voltage does not swell above the nominal voltage [5]. This configuration can be extended to the bi-pole configuration by adding the same monopole VSC HVDC system with the opposite polarity.

The symmetrical monopole VSC HVDC system in Fig. 1.6 consists of positive and negative poles. The nominal voltage of each pole is half of the nominal converter voltage, which is $\pm V_n / 2$. When a pole-to-ground fault occurs, the voltage in the faulted pole drops while the healthy pole voltage swells up to V_n.

The bi-pole configuration in Fig. 1.7 can be interpreted as the integration of two independent asymmetrical monopole systems with different polarities. The nominal voltage of each pole is equal to the converter nominal voltage V_n. In normal balanced operations, DC current flows via positive and negative conductors. When one pole is not available, the other pole can still operate independently if the metallic return path is installed.

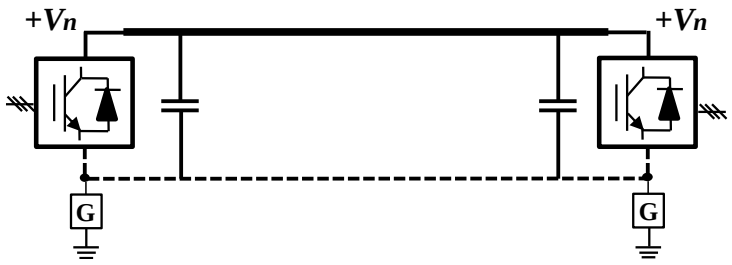

Fig. 1.5. Asymmetric monopole configuration [5]

Fig. 1.6. Symmetric monopole configuration [5]

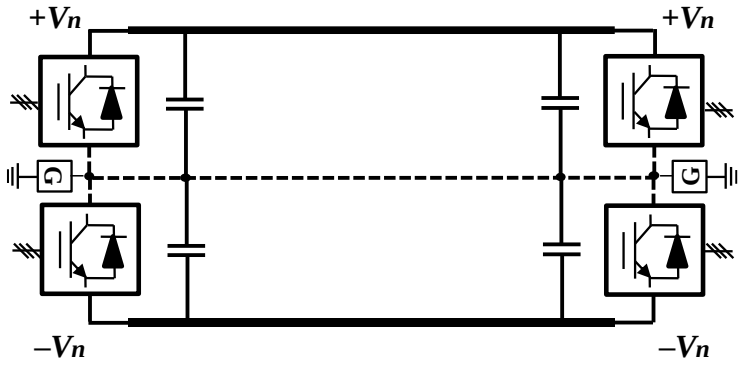

Fig. 1.7. Bi-pole configuration [5]

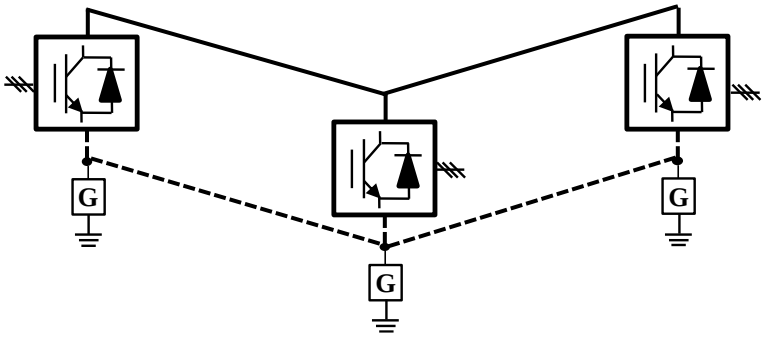

Fig. 1.8. Asymmetric monopole multi-terminal VSC HVDC with earth return [5]

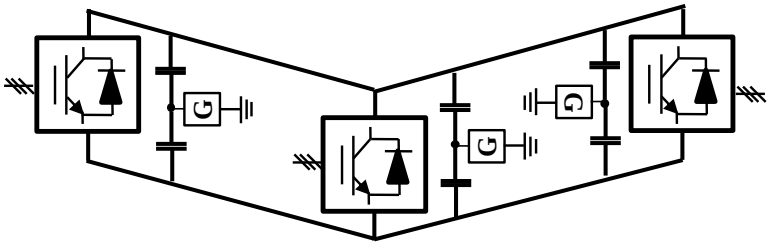

Fig. 1.9. Symmetric monopole multi-terminal VSC HVDC [5]

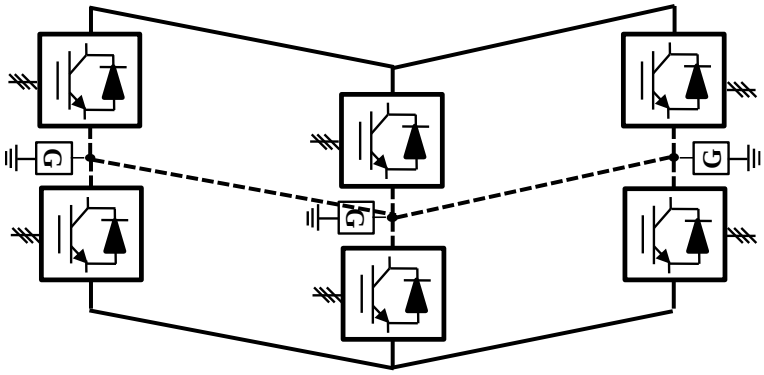

Fig. 1.10. Bi-pole multi-terminal VSC HVDC with metallic return [5]

1.2 Related Previous Works

Transmission expansion planning (TEP) with VSC HVDC systems has been investigated in several previous works [6]-[10]. In particular, TEP using VSC HVDC systems to install RES has been discussed in [8]-[10]. A probabilistic TEP approach has been adopted in [11] for the long-distance RES power transmission with MTDC systems. TEP formulations with HVDC systems have been investigated in [12], [13] based on the optimization process. However, the dynamic behaviors of the HVDC systems have not been considered in [12], [13]. In addition, power system stability issues have been considered in the TEP problems of [6]-[13]. TEP of HVDC systems and offshore wind farms has been studied considering the improvement of DC grid stability in [14]. Transient stability of the system models has been covered in TEP with HVDC systems in [15], [16].

Regarding power system operations, OPF is one of the widely adopted approaches where system constraints are considered. The economic and reliable MTDC operations with offshore wind power plants have been discussed in [17]. The N-1 criterion has been integrated in OPF analysis of power systems with VSC HVDC systems in [18]-[21]. In [22], the voltage stability of the power system model with VSC HVDC systems has been surveyed. The economic benefits produced by several different multi-terminal VSC HVDC systems have been calculated and compared by OPF approach in [23]. It has been revealed by the robust OPF analysis that the maximum admissibility boundaries of offshore wind farm outputs can be increased in [24].

In summary, a lot of research works have focused on power system reinforcements and operations using VSC HVDC systems for RES transmission. These works are classified in Fig. 1.11.

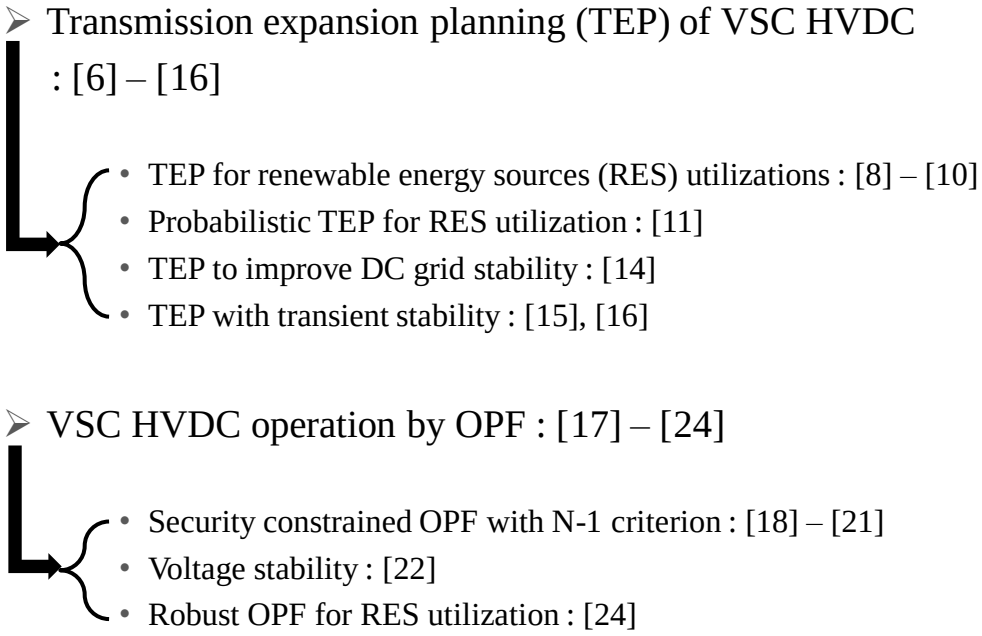

Fig. 1.11. Classification of previous works

The first novelty of this dissertation is the flexible multi-terminal reinforcement and operation proposals of MTDC systems based on the hierarchical OPF analysis. This hierarchical OPF analysis aims at increasing the economic benefits obtained by a MTDC system. In the first step, a MTDC system reinforcement in a power system model is designed for large-scale wind power transmission. In the second step, the optimal operations of the reinforced system model in different conditions are determined. In case of high RES outputs, the MTDC transmission system mainly transmits the RES power output. If the RES output is not high enough, the MTDC system can also be utilized for the power transmission among AC grids.

The second contribution of this dissertation is the consideration of power system stability constraints in the analysis. Among many kinds of power system stability issues, rotor-angle stability; small-signal stability and transient rotor-angle stability which are the critical aspects of large-scale wind power transmission in Japan are needed to be included. On top of that, transient AC and DC voltage stabilities of mixed AC / multi-terminal VSC HVDC systems are also constrained considering AC and DC grid faults. As a consequence, unlike large-scale RES transmission using conventional AC transmission systems, the calculated OPF solutions in mixed AC / multi-terminal VSC HVDC systems are stable from these power system stability viewpoints.

1.3 Objectives and Structure of Dissertation

The objectives of this dissertation are summarized as follows. The author hopes that this dissertation can be utilized as the guideline of VSC HVDC system implementations for the integration of large-scale renewable energy sources.

1. Propose the reinforcement and operation methods to increase the economic benefits of wind power transmission systems using a multi-terminal VSC HVDC system.
2. Develop optimal power flow formulation with power system stability constraints.
3. Discuss fault analysis and a protection strategy in mixed AC / multi-terminal VSC HVDC systems.
4. Suggest the integrated analysis for VSC HVDC systems considering both transmission expansion planning and operation stages.
5. Calculate wind power hosting capacities of power system models for large-scale wind energy utilizations.
6. Evaluate multi-terminal VSC HVDC systems from power system stability viewpoints.

Considering the characteristics of the VSC technology, VSC HVDC systems with multi-terminal configurations are adopted to overcome the low transmission system profits and power system stability issues in this dissertation. When the wind power production is not high, a multi-terminal VSC HVDC system can still be used for the active power transmission among AC grids to relieve the first problem. As a consequence, additional economic benefits compared to the conventional transmission system operation can be produced. Regarding the second problem, the active power transmission in a HVDC system is free from the rotor-angle stability issues of AC systems. On top of that, the control systems of a VSC HVDC system can also contribute to the power system stabilization, which enables to increase the amount of wind power plants installation.

To this end, power system reinforcement and operation methods using multi-terminal VSC HVDC systems are developed in this dissertation. Optimal power flow (OPF) analysis based on hierarchical approaches is suggested to evaluate MTDC systems considering both reinforcements and operations. In order not to violate power system stability issues, those are also taken into account as additional constraints in the OPF analysis.

The summarized organization of this dissertation is shown in Fig. 1.12. It can be seen that based on the proposed hierarchical optimal power flow analysis, multi-terminal VSC HVDC systems are evaluated from the small-signal and transient stability viewpoints. In the transient stability analysis, the small-signal stability constraint to prevent eigenvalues with positive real parts is also included.

The models of mixed AC / multi-terminal VSC HVDC systems with wind power plants are explained in Chapter 2. The detailed behaviors of AC grid, VSC HVDC system, and wind power plant model are covered. The hierarchical optimal power flow analysis determining both transmission expansion planning and system operation is suggested in Chapter 3. In Chapter 4, the analysis considering small-signal stability constraints is carried out. First of all, the wind power hosting capacities of power system models reinforced with either new AC systems or a multi-

terminal VSC HVDC system are compared to see the limitation of AC transmission systems. Several different multi-terminal configurations are considered and the system with the largest hosting capacity is found among them. Sensitivity analyses of wind power capacity and small-signal stability constraints are discussed. In Chapter 5, the transient stability constraints of AC and DC grids are taken into account. The analysis of Chapter 5 focuses on the influences of the transient stability constraints. Wind power hosting capacity of the multi-terminal VSC HVDC system with the transient stability constraints is calculated. The results of the hierarchical transient stability constrained optimal power flow analysis, the investment costs and fuel costs of the system reinforced by a multi-terminal VSC HVDC system are compared to the results without the transient stability constraints. Time-domain simulation results are checked to understand the transient behaviors of mixed AC / multi-terminal VSC HVDC systems. Finally, this dissertation is concluded in Chapter 6 with some future work proposals.

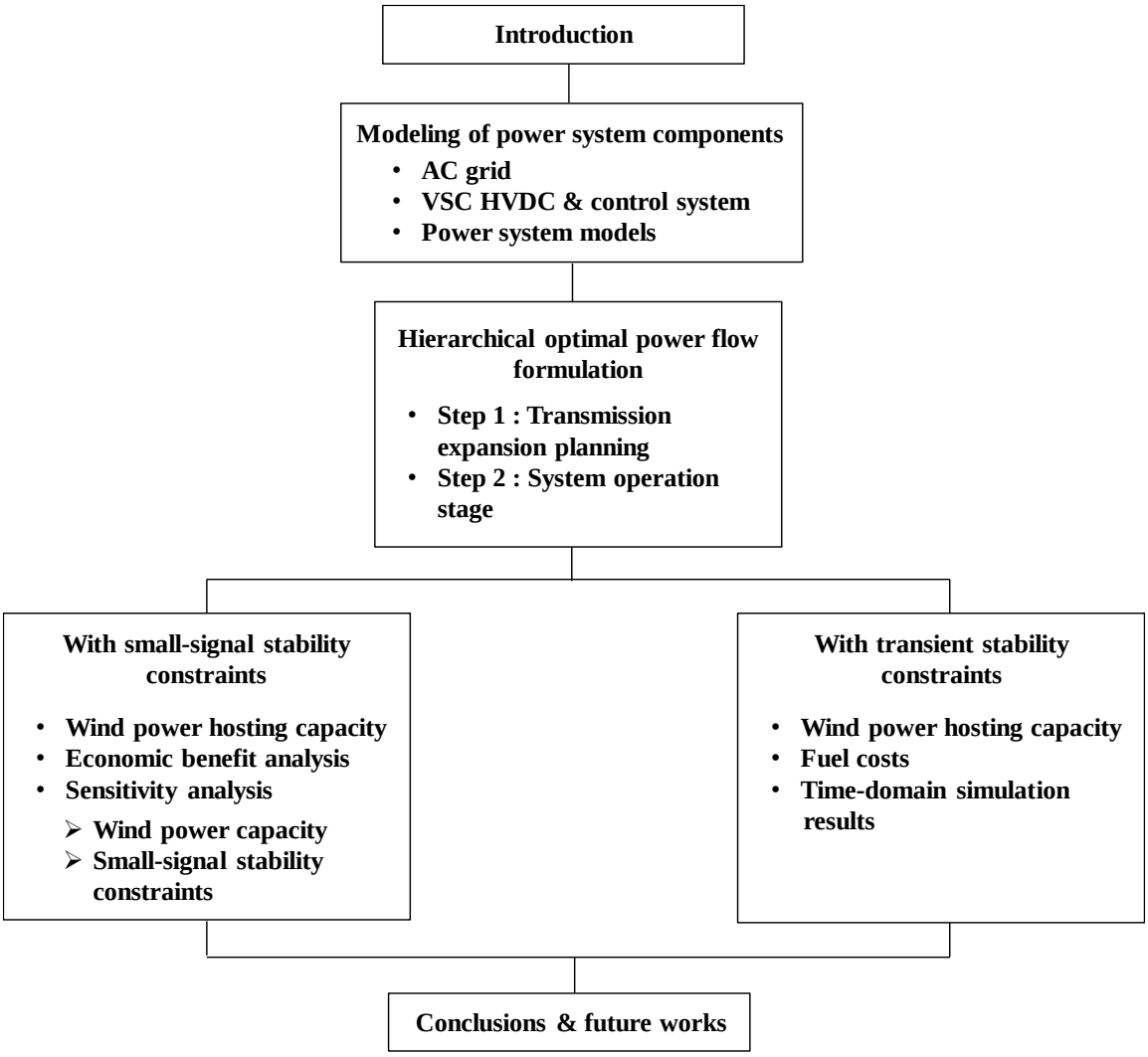

Fig. 1.12. Organization of this dissertation

2. Models of Mixed AC / Multi-Terminal VSC HVDC System with Wind Power Plants

2.1 AC Grid Models

Synchronous generator model

As the synchronous generator model, Park's equivalent model with one damping circuit (*kd* circuit) in *d*-axis and two damping circuits (*fq* and *kq* circuits) in *q*-axis in Fig. 2.1 is adopted. Rotor field winding circuit is represented as the *fd* circuit in *d*-axis in Fig. 2.1. *d*-axis is aligned with the rotor whereas *q*-axis leads by π / 2 rad compared to *d*-axis. The mutual inductance components between *d* and *q* axes circuits are able to disappear by this Park's transformation. The flux linkage equations are based on the assumption that the mutual inductances between the stator side and rotor side circuits in *d* and *q* axes have the same values. In three-phase symmetrical states, the output and torque of a synchronous generator can be represented as below.

Equations of stator voltage and current

$$v_d = p\phi_d - \phi_q p\delta - Ri_d \tag{2.1.1}$$
$$v_q = p\phi_q + \phi_d p\delta - Ri_q \tag{2.1.2}$$

Equations of rotor voltage and current

$$v_f = p\phi_{fd} + R_{fd}i_{fd} \tag{2.1.3}$$
$$0 = p\phi_{kd} + R_{kd}i_{kd} \tag{2.1.4}$$
$$0 = p\phi_{fd} + R_{fd}i_{fd} \tag{2.1.5}$$
$$0 = p\phi_{kq} + R_{kq}i_{kq} \tag{2.1.6}$$

Equations of flux linkage

$$\phi_d = -x_d i_d + x_{md}i_{fd} + x_{md}i_{kd} \tag{2.1.7}$$
$$\phi_{fd} = -x_{md}i_d + x_{fd}i_{fd} + x_{md}i_{kd} \tag{2.1.8}$$
$$\phi_{kd} = -x_{md}i_d + x_{md}i_{fd} + x_{kd}i_{kd} \tag{2.1.9}$$
$$\phi_q = -x_q i_q + x_{mq}i_{fq} + x_{mq}i_{kq} \tag{2.1.10}$$
$$\phi_{fq} = -x_{mq}i_q + x_{fq}i_{fq} + x_{mq}i_{kq} \tag{2.1.11}$$
$$\phi_{kq} = -x_{mq}i_q + x_{mq}i_{fq} + x_{kq}i_{kq} \tag{2.1.12}$$

Equations of power and torque

$$P_e = v_d i_d + v_q i_q \tag{2.1.13}$$

$$T_e = \phi_d i_q - \phi_q i_d \tag{2.1.14}$$

Swing equations

$$2H \frac{d\omega}{dt} = T_m - T_e - D(\omega - \omega_0) \tag{2.1.15}$$

$$\omega_0 = 1 p.u. \tag{2.1.16}$$

$$\frac{d\delta}{dt} = \omega - \omega_0 \tag{2.1.17}$$

p	Differentiation operator with respect to time domain
ϕ_d, v_d, i_d	Linkage flux, voltage, current in *d*-axis circuit
ϕ_q, v_q, i_q	Linkage flux, voltage, current in *q*-axis circuit
$\phi_{fd}, v_{fd}, i_{fd}$	Linkage flux, voltage, current in *fd* winding circuit
$\phi_{kd}, v_{kd}, i_{kd}$	Linkage flux, voltage, current in *kd* winding circuit
$\phi_{fq}, v_{fq}, i_{fq}$	Linkage flux, voltage, current in *fq* winding circuit
$\phi_{kq}, v_{kq}, i_{kq}$	Linkage flux, voltage, current in *kq* winding circuit
x_{fd}, x_{kd}	Self-inductances in *d*-axis circuit
x_{md}	Mutual inductance between windings in *d*-axis circuit
x_{fq}, x_{kq}	Self-inductances in *q*-axis circuit
x_{mq}	Mutual inductance between windings in *q*-axis circuit
$R, R_{fd}, R_{kd}, R_{fq}, R_{kq}$	Resistances in each circuit
T_m, T_e	Mechanical input torque, electrical output torque
P_e	Electrical output power
δ, ω	Generator rotor phase angle, rotational speed
ω_0	Synchronous rotational speed of grid
H, D	Normalized inertia constant, damping coefficient

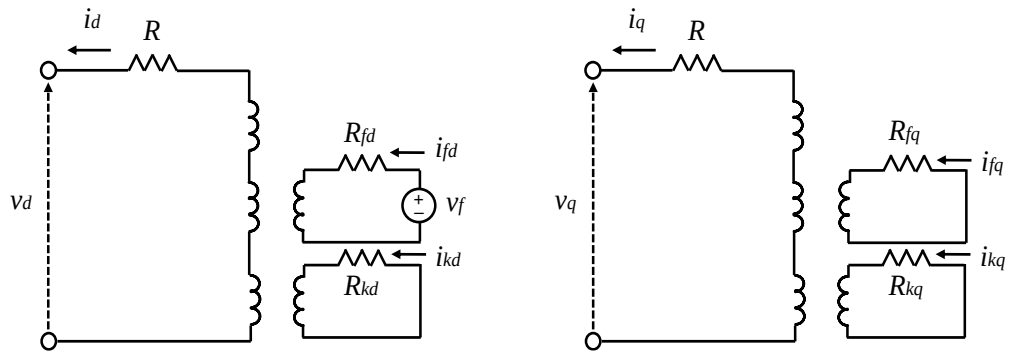

Fig. 2.1. Equivalent circuit of synchronous generator (left : *d*-axis, right : *q*-axis)

Instead of the parameters of a generator above, the measurable parameters of a synchronous generator are synchronous reactance, transient reactance, sub-transient reactance, open-circuit transient time constant, and open-circuit sub-transient time constant as below. The generator parameters can be calculated using these measureable values based on (2.1.18) – (2.1.23) relationships. The parameters in *q*-axis can also be obtained with the same principle.

x_d	Synchronous reactance in *d*-axis
$x_d^{'}$	Transient reactance in *d*-axis
$x_d^{''}$	Sub-transient reactance in *d*-axis
$T_{d0}^{'}$	Open circuit transient time constant in *d*-axis
$T_{d0}^{''}$	Open circuit sub-transient time constant in *d*-axis

$$x_{md} = x_d - x_l \tag{2.1.18}$$

$$x_{lfd} = \frac{(x_d^{'} - x_l)(x_d - x_l)}{x_d - x_d^{'}} \tag{2.1.19}$$

$$x_{fd} = x_{md} + x_{lfd} \tag{2.1.20}$$

$$x_{lkd} = \frac{(x_d^{'} - x_l)(x_d^{''} - x_l)}{x_d^{'} - x_d^{''}} \tag{2.1.21}$$

$$R_{fd} = \frac{x_{fd}}{T_{d0}^{'}} \tag{2.1.22}$$

$$R_{kd} = \frac{(x_d^{'} - x_d^{''})x_{kd}}{(x_d - x_d^{''})T_{d0}^{''}} \tag{2.1.23}$$

For the time-domain simulation analysis, this generator model is modified to be sixth-order synchronous generator model based on the following assumption. Among all leakage flux components aligned with *d* axis circuit, the fluxes linked with two circuits (*d* & *fd*, *fd* & *kd* and kd & *d*) are negligible [25] as described in Fig. 2.2. Only the leakage flux components linked with one circuit are considered. The same assumption can also be applied to the leakage flux components

aligned with q axis. This leads to the following generator model in the form of differential equations.

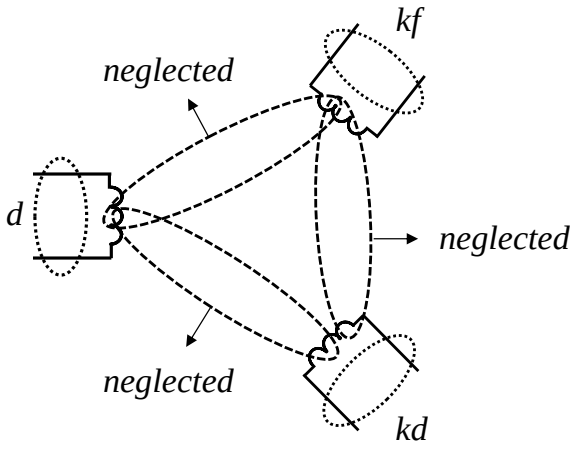

Fig. 2.2. Leakage flux components of circuits aligned with *d* axis [25]

$$\frac{d\delta(t)}{dt} = \omega(t) - \omega_0 \tag{2.1.24}$$

$$\frac{d\omega(t)}{dt} = \frac{\omega_0}{2H}\left[\frac{\omega_0}{\omega(t)}P_m(t) - \frac{\omega_0}{\omega(t)}P_e(t) - D\left(\frac{\omega(t)}{\omega_0} - 1\right)\right] \tag{2.1.25}$$

$$\begin{aligned}\frac{de'_q(t)}{dt} = \frac{1}{T'_{d0}}\Bigg[&e_f(t) + \frac{(L_d - L'_d)(L'_d - L''_d)}{(L'_d - L_l)^2}K_d e''_q(t) \\ &- \left\{1 + \frac{(L_d - L'_d)(L'_d - L''_d)}{(L'_d - L_l)^2}\right\}e'_q(t) \\ &- \frac{\omega(t)}{\omega_0}\frac{(L_d - L'_d)(L''_d - L_l)}{L'_d - L_l}i_d(t)\Bigg]\end{aligned} \tag{2.1.26}$$

$$\frac{de''_q(t)}{dt} = -\frac{1}{T''_{d0}K_d}\left\{K_d e''_q(t) - e'_q(t) + \omega(t)(L'_d - L_l)i_d(t)\right\} \tag{2.1.27}$$

$$\begin{aligned}\frac{de'_d(t)}{dt} = -\frac{1}{T'_{q0}}\Bigg[&-\frac{(L_q - L'_q)(L'_q - L''_q)}{(L'_q - L_l)^2}K_q e''_d(t) \\ &+ \left\{1 + \frac{(L_q - L'_q)(L'_q - L''_q)}{(L'_q - L_l)^2}\right\}e'_d(t) \\ &- \frac{\omega(t)}{\omega_0}\frac{(L_q - L'_q)(L''_q - L_l)}{L'_q - L_l}i_q(t)\Bigg]\end{aligned} \tag{2.1.28}$$

$$\frac{de''_d(t)}{dt} = -\frac{1}{T''_{q0}K_q}\left\{K_q e''_d(t) - e'_d(t) - \omega(t)(L'_q - L_l)i_q(t)\right\} \tag{2.1.29}$$

where

$$K_d = 1 + \frac{(L'_d - L_l)(L''_d - L_l)}{(L'_d - L''_d)(L_d - L_l)} \tag{2.1.30}$$

$$K_q = 1 + \frac{(L'_q - L_l)(L''_q - L_l)}{(L'_q - L''_q)(L_q - L_l)} \tag{2.1.31}$$

Each synchronous generator is equipped with automatic voltage regulator (AVR) and turbine governor (GOV) systems. These control systems are modeled as first-order lag transfer functions for the simplicity. Generator terminal voltage v_t is controlled by AVR system by adjusting excitation voltage v_f. Generator rotational speed ω is maintained by GOV system by controlling mechanical input power P_m.

Equations of AVR and GOV systems

$$\frac{dP_m}{dt} = -\frac{1}{\mathrm{T_G}}\{(P_m - P_{m0}) + K_G(\omega - \omega_0)\} \tag{2.1.32}$$

$$\frac{dv_f}{dt} = -\frac{1}{\mathrm{T_A}}\left\{(v_f - v_{f0}) + \frac{R_{fd}}{\omega_0 x_{md}} K_G(v_t - v_{t0})\right\} \tag{2.1.33}$$

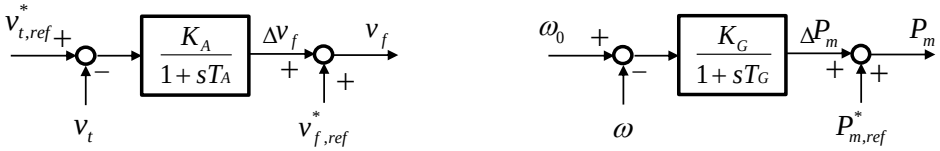

$$\Delta v_f = v_f - v^*_{f,ref} \qquad \Delta P_m = P_m - P^*_{m,ref}$$

Fig. 2.3. AVR and GOV models of generator

$v^*_{t,ref}, v_t$	Generator terminal voltage reference, generator terminal voltage
K_A, T_A	Gain, time constant of AVR system
$v^*_{f,ref}, v_f$	Excitation voltage reference, excitation voltage
$P^*_{m,ref}, P_m$	Mechanical input power reference, mechanical input power
K_G, T_G	Gain, time constant of GOV system

Load model

Loads in power systems consist of thousands of different and complicated components. It is practically impossible to perfectly reflect the behaviors of all load components. Hence, load models are expressed as aggregated simple models in general power system analysis. In static models, the active and reactive power consumptions P and Q of a load model are dependent on its AC bus voltage and frequency, which can be represented as (2.1.34) and (2.1.35). The subscript 0 indicates the initial operating condition values. Δf represents the frequency deviation from the nominal AC bus frequency. The constant impedance (constant Z) model, the constant current (constant I) model, and the constant power (constant P) model are represented in the first, second, and third terms with the coefficients p_1, p_2, and p_3 respectively [26]. In dynamic load models, it is important to consider the characteristics of induction motors since they take the largest portion in many power system loads.

$$P = P_0\left\{ p_1(\frac{V}{V_0})^2 + p_2(\frac{V}{V_0}) + p_3 \right\}(1 + K_{pf}\Delta f) \tag{2.1.34}$$

$$Q = Q_0\left\{ q_1(\frac{V}{V_0})^2 + q_2(\frac{V}{V_0}) + q_3 \right\}(1 + K_{qf}\Delta f) \tag{2.1.35}$$

Wind power plant model

The installation of large-scale wind power plants is one of the main objectives of this dissertation. In such scenarios, several nearby hundreds or thousands of wind turbines are aggregated to be handled. Therefore, aggregated large-scale wind farm models are introduced in power system models in this dissertation.

In order to simplify the implementation of wind farm models, the static model in Fig. 2.5 is adopted. $v_{s,WF}$ indicates the wind-farm-connected point of common coupling (PCC) bus. In normal operations of $v_{s,WF} \geq 0.9$ *p.u.*, the wind farms are considered as the static load models with constant power characteristics. If $v_{s,WF}$ drops below 0.9 *p.u.*, they are handled as static constant current loads considering the current limiters of wind power plant converters.

Inverter-driven RES facilities including photovoltaic generations (PV) and wind turbines (WT) are needed to be blocked or disconnected during the voltage drop of the connection point to protect the facilities. On the other hand, the attention should be carefully paid to the massive disconnections of these units considering the power supply and demand imbalance. In this context, such inverter-driven RES facilities are required to equip with fault ride through (FRT) capabilities. They imply that the facilities should be able to endure a voltage drop and be connected to the grid side. Different voltage profile criteria have been determined by many power system operators. In this dissertation, the FRT requirement for wind power generation facilities in Japan by [27] in Fig. 2.5 is implemented. According to [27], a wind farm model is allowed to be disconnected if the wind-farm-connected AC bus voltage does not satisfy the voltage profile in Fig. 2.5.

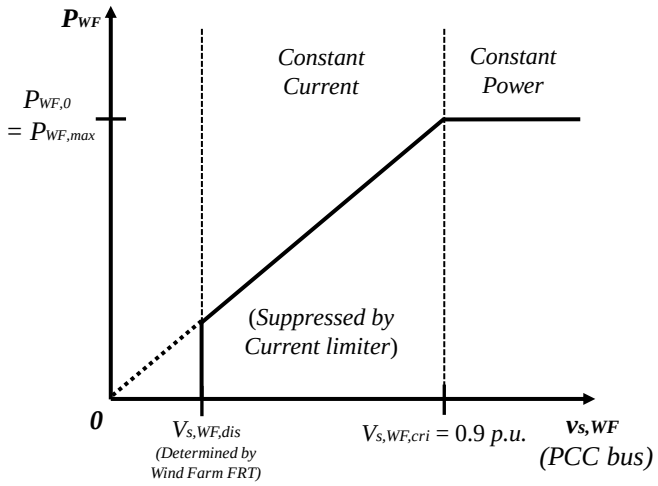

Fig. 2.4. Static wind power plant model

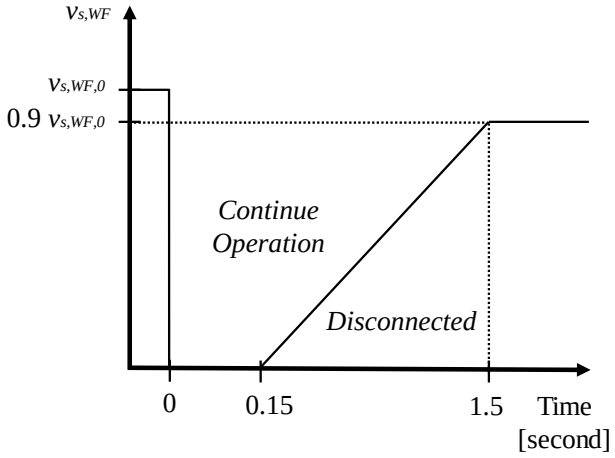

Fig. 2.5. Fault ride through requirement of wind power plant model [27]

2.2 VSC HVDC System Model

Several types of VSC HVDC models have been proposed for the power system analysis, which is summarized in [28]. Full physics-based models can simulate the behaviors of VSC HVDC systems most accurately, but it requires extensive computational burdens. The detailed and simplified characteristics of IGBT switching characteristics are modeled in the IGBT-based models. The Thevenin equivalent circuit is derived based on a simple circuit reduction in equivalent-circuit-based model. In the average value model, the detailed behaviors of switching devices are not considered. A VSC converter is represented as the controlled voltage and current sources in the average value model. In this dissertation, the average value model approach is adopted in which only the fundamental frequency component of the AC controlled voltage source is taken into account.

The average value model of VSC HVDC system with the control system is described in Fig. 2.6. Not only monopole HVDC systems, but bi-pole HVDC systems with symmetrical operations can also be simulated with this model. The representations of '*dq*' frame for this VSC HVDC system model indicates the synchronously rotating frame with synchronous rotational speed ω_0. Therefore, it should be noted that the meaning of '*dq*' frame for this VSC HVDC system model is different from '*dq*' axes explained in the synchronous generator model. Phase reactor, transformer, and AC filter components are represented as R_c and L_c. v_c and v_s refer to the AC voltages at the AC / DC interface bus and the voltage at a point of common coupling (PCC) bus respectively. The resistive, inductive, and capacitive components of DC transmission lines are modeled as R_{DC}, L_{DC}, and C_{DC} respectively. The subscript *'i'* indicates the VSC converter number '*i*'. The grid parameters of VSC HVDC system model per GVA in Table 2.1 are used. With the installations of DC circuit breakers, two 0.1 *p.u.* reactances are added at both ends of each DC transmission line.

The behaviors of the VSC HVDC model are represented as the following mathematical equations (1) – (4) where the active and reactive power outputs of the VSC *i* are defined as (2.2.5) and (2.2.6) respectively. Kirchhoff's current low (KCL) at DC bus of VSC *i* corresponds to (2.2.3). A very low value of R_{DC_f} in (2.2.3) is considered to simulate a fault in the DC grid side. The DC transmission line current flow from DC bus *i* to DC bus *j* is represented in (2.2.4).

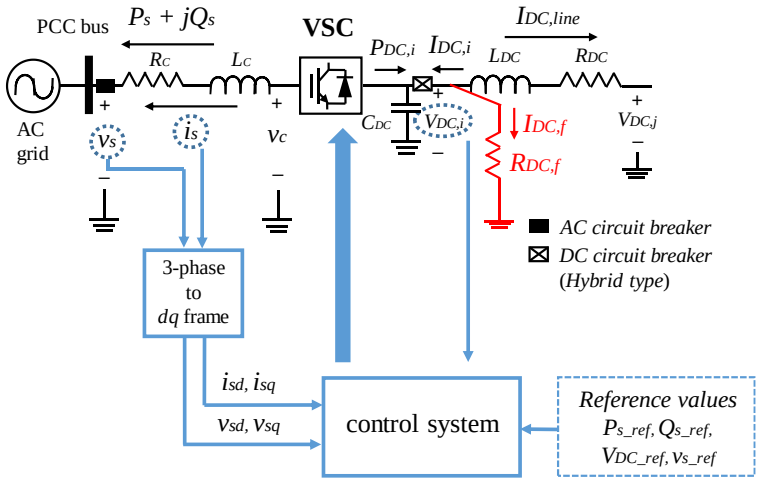

Fig. 2.6. Average value model of VSC HVDC system

$$L_c \frac{di_{sdi}}{dt} = -R_c i_{sdi} + \omega L_c i_{sqi} + v_{cdi} - v_{sdi} \quad (2.2.1)$$

$$L_c \frac{di_{sqi}}{dt} = -R_c i_{sqi} - \omega L_c i_{sdi} + v_{cqi} - v_{sqi} \quad (2.2.2)$$

$$C_{DC} \frac{dV_{DC,i}}{dt} = \frac{P_{DC,i}}{V_{DC,i}} + I_{DC,i} - \frac{V_{DC,i}}{R_{DC,f}} \quad (2.2.3)$$

$$L_{DC} \frac{dI_{DC,line}}{dt} = -R_{DC} I_{DC,line} + V_{DC,i} - V_{DC,j} \quad (2.2.4)$$

$$P_{s,i} = v_{sdi} i_{sdi} + v_{sqi} i_{sqi} \quad (2.2.5)$$

$$Q_{s,i} = v_{sqi} i_{sdi} - v_{sdi} i_{sqi} \quad (2.2.6)$$

Table 2.1. Grid parameters of VSC HVDC system model per GVA

R_c	2×10^{-4} *p.u.*
L_c	0.03 *p.u.*
R_{DC}	1.424×10^{-4} *p.u./* km
L_{DC}	2×10^{-5} *p.u./* km
C_{DC}	5*ms*

A DC grid with overhead transmission lines is exposed to many DC fault types. The DC fault types in a bi-pole VSC HVDC system are described in Fig. 2.7 [3]. Type (a), a pole-to-ground fault is the most frequent type in DC overhead transmission systems. The influences of types (c) and (d) on a power system operation are evaluated to be the most critical since both poles are exposed to a large disturbance and disabled. Therefore, the fault type (d) is taken into consideration in the analysis. As a result, it implies that the OPF solutions in this dissertation are robust from the DC fault viewpoints so that they are able to endure the most severe DC fault type.

(a) Pole-to-ground fault
(b) Pole-to-neutral fault
(c) pole-to-pole fault
(d) bipole-to-ground fault
(e) DC bus fault
(f) neutral-to-ground fault

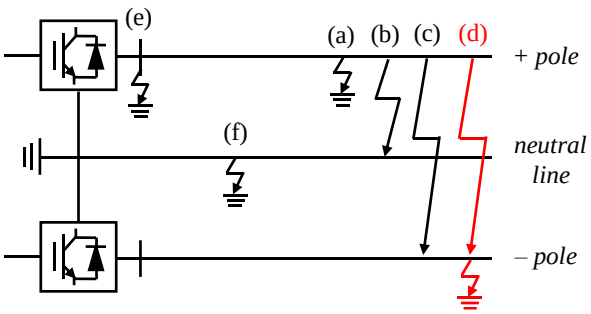

Fig. 2.7. Types of DC faults in a bi-pole VSC HVDC system [3]

Vector current control systems plotted in from Fig. 2.8 to Fig. 2.10 are adopted for the control systems of VSC HVDC systems. The reference value of a variable is notated using the superscript *. The active and reactive currents, i_{sd} and i_{sq} are decoupled by removing the feedforward terms $-\omega L_c i_{sd}$ and $-\omega L_c i_{sq}$ in the inner current controller. Consequently, the active and reactive power outputs can be controlled independently. The values of the pre-disturbance state obtained by an OPF solution are utilized for the reference values. The control systems in Fig. 2.8 and Fig. 2.10 are used for this VSC operation.

Among VSC converters in a multi-terminal VSC HVDC system, a VSC is assigned to maintain DC bus voltage V_{DC} instead of its active power output P_s. This VSC is called the VSC slack in a multi-terminal VSC HVDC system. The control systems in Fig. 2.9 and Fig. 2.10 are equipped for the VSC slack.

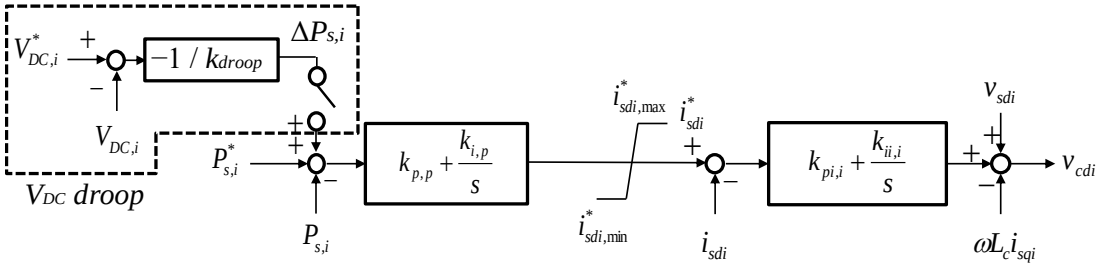

Fig. 2.8. Active current i_{sd} control system except VSC slack

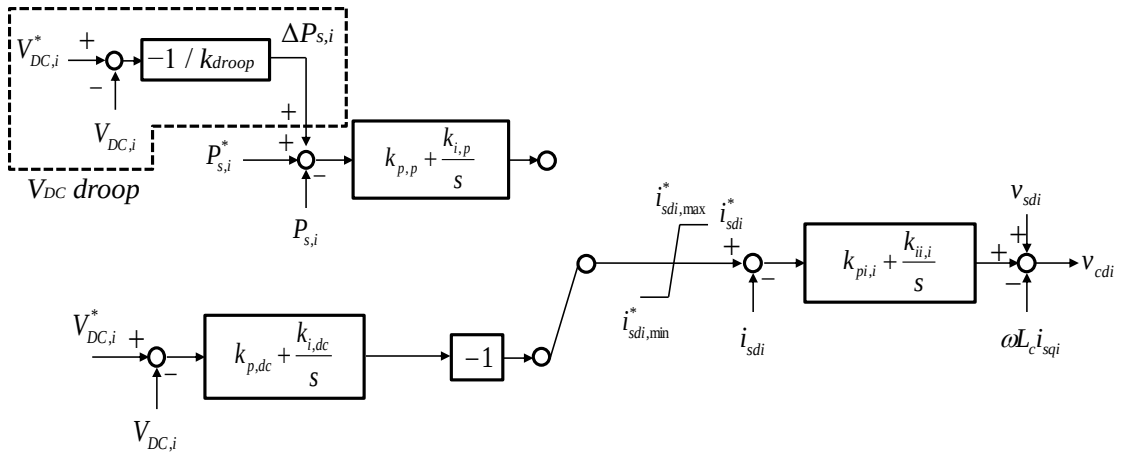

Fig. 2.9. Active current i_{sd} control system for VSC slack

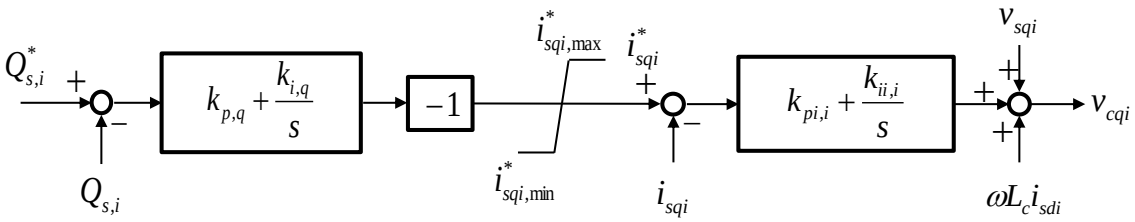

Fig. 2.10. Reactive current i_{sq} control system

The active and reactive current references; i_{sd} and i_{sq} of a VSC converter are produced by the outer controller. These current reference values are limited by its VSC current limiter considering the VSC capacity. Since both active and reactive currents can be controlled independently, several methods for a VSC current limiter can be considered depending on priorities of i_{sd} and i_{sq}.

The method adopted in this dissertation is the constant power factor method in Fig. 2.11. When $\sqrt{i_{sd}^{*} + i_{sq}^{*}}$ exceeds the VSC current capacity, both i_{sd}^{*} and i_{sq}^{*} are limited while the power factor is fixed as described in Fig. 2.11. Here, this method is applied to utilize the controllability of both the active and reactive currents.

On the other hand, the active current reference i_{sd}^{*} has higher priority to the reactive current reference i_{sq}^{*} in Fig. 2.12. This method aims at maximizing the controllability of i_{sd}^{*} as much as possible. The VSC capacity is allocated preferentially for i_{sd}^{*}control. The rest of the VSC capacity is assigned for i_{sq}^{*}control.

The reactive current reference i_{sq}^{*} can also have higher priority to the active current reference i_{sd}^{*}. This method can be adopted in cases of controlling AC grid side voltage, STATCOM-mode operation, dynamic voltage support and so on. The VSC capacity is assigned preferentially for i_{sq}^{*}control and the rest is allocated for i_{sd}^{*}control as illustrated in Fig. 2.12.

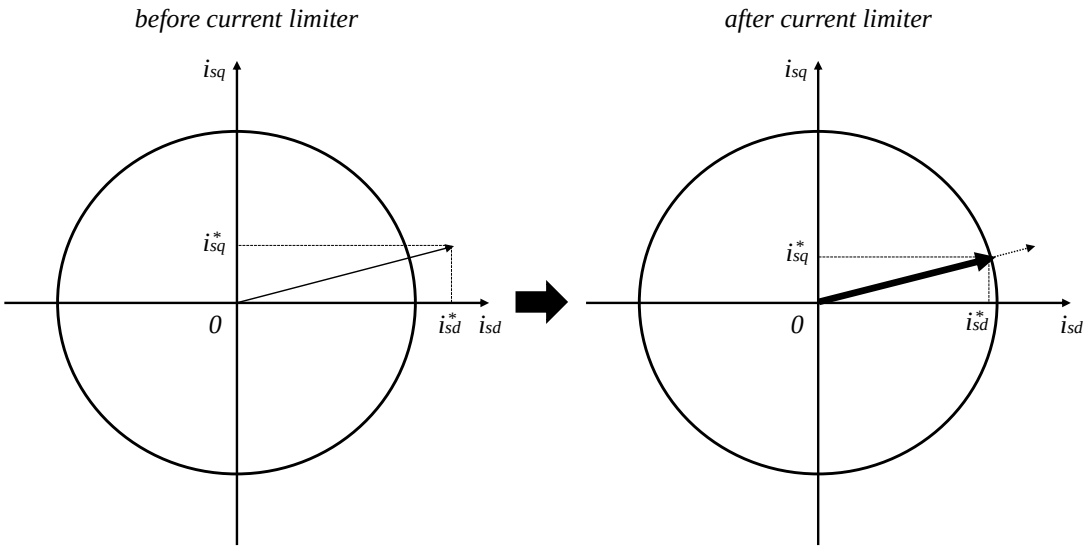

Fig. 2.11. Constant power factor method of VSC current limiter

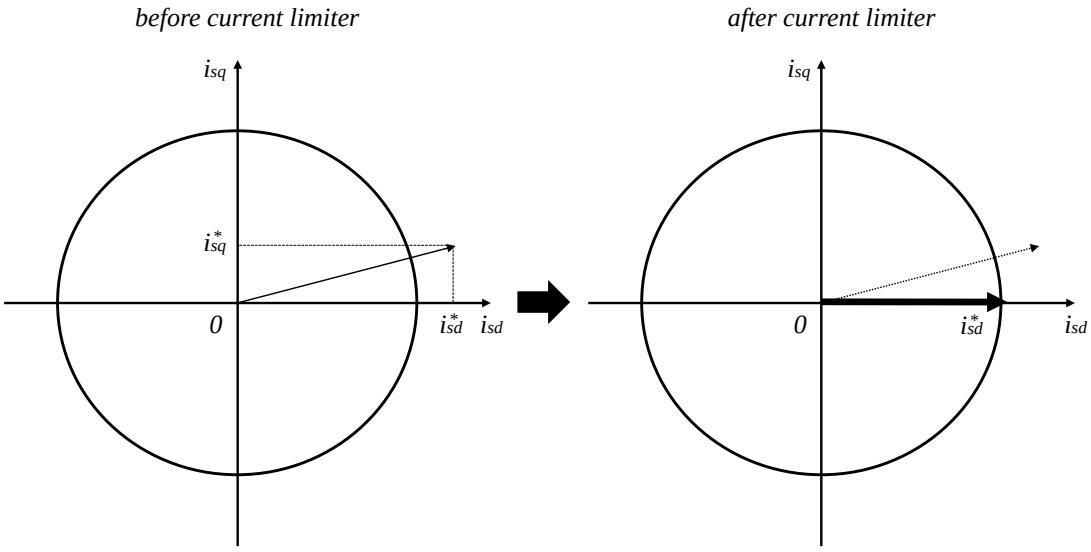

Fig. 2.12. Active current i_{sd} priority method of VSC current limiter

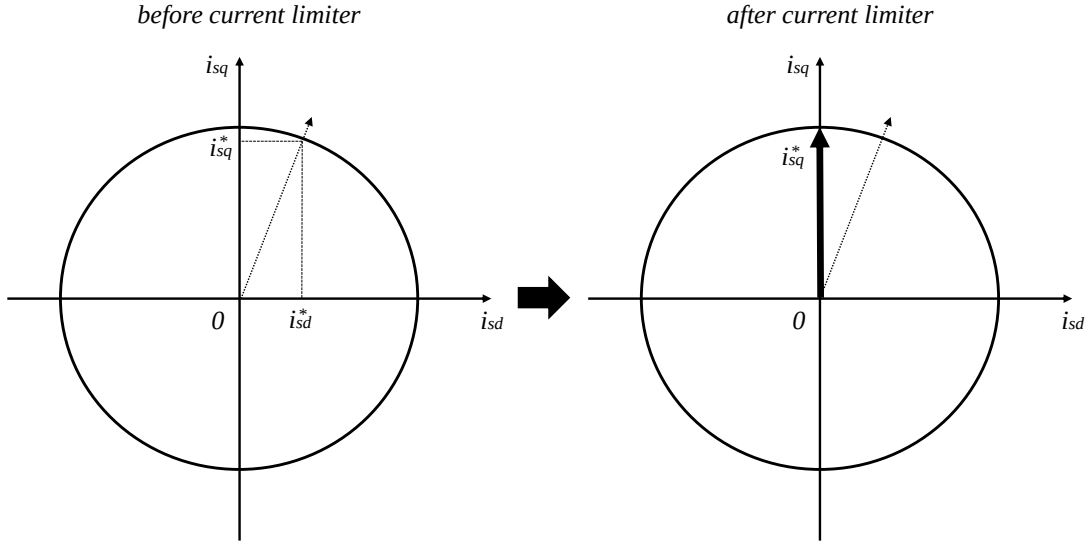

Fig. 2.13. Reactive current i_{sq} priority method of VSC current limiter

As for the DC voltage control cooperation of multi-terminal VSC HVDC systems, the VSC slack is in charge of controlling DC bus voltage as explained above. However, this method has a critical disadvantage that DC voltage cannot be maintained properly in case of the VSC slack outage or a fault occurrence near the VSC slack. In order to overcome this problem, other VSCs are also needed to participate in the DC voltage control. Two popular approaches for the cooperation of the DC voltage control are developed. The modified hybrid version of these approaches is adopted in this dissertation.

Alternative VSC slacks are prepared considering the outage of the original VSC slack in the voltage margin method [29]. For example, VSC A in Fig. 2.14 is the VSC slack controlling the DC voltage in the normal state. Other two VSCs operate by controlling their active power outputs respectively. If VSC A is not available due to a contingency, either VSC B or VSC C takes the part of the VSC slack. In Fig. 2.14, VSC B with narrower DC voltage margin replaces the charge of the original VSC slack. In case of the outages of both VSCs A and B, VSC C is in charge of the VSC slack. One of the advantages of this method is that the active power outputs except the VSC slack are maintained as constants. Nevertheless, it is difficult task to determine the proper DC voltage margin for each VSC. On top of that, the disadvantage of the high responsibility of the original VSC for the DC voltage control cannot perfectly be relieved.

The other cooperation method is the DC voltage droop control using the concept of Fig. 2.15, (2.2.7), and (2.2.8) [29]. The droop control of a VSC adjusts its active power reference value depending on its DC voltage deviation. In contrast to the voltage margin method, multiple VSCs can participate in the DC voltage control simultaneously. As a consequence, the large responsibility of only a single VSC slack can be relieved by this droop approach. Various types of DC voltage droop control systems have been investigated; voltage-active power droop in [30], voltage-current droop in [31], and DC voltage droop with dead-bands in [32]. An example of the DC voltage droop control with the voltage-active power droop is plotted in Fig. 2.16. Different droop gains can be used as described in Fig. 2.16. In Fig. 2.16, VSC A with the lowest absolute value of the slope takes the most part of the DC voltage control. Although the DC voltage droop control has these aspects, the adjustments of the original reference values can trigger additional disturbances to the original system operation due to the deviations of reference values.

Considering these characteristics, the control systems in Fig. 2.8 and Fig. 2.9 are designed for the DC voltage control cooperation in this dissertation. In the normal state or with negligible disturbance cases, a VSC except the slack controls its active and reactive power outputs. Only the VSC slack is in charge of controlling DC voltage to be constant. This is similar to the characteristics of the conventional voltage margin method. On the contrary, if a VSC is equipped with the DC voltage droop control, the DC voltage droop control is activated by using the concepts of Fig. 2.15, (2.2.7) and (2.2.8). Here, a V_{DC} deviation $|V_{DC}^{*} - V_{DC}|$ larger than 0.05 *p.u.* is considered to be a significant V_{DC} deviation. Therefore, the DC voltage droop control is activated if $|V_{DC}^{*} - V_{DC}| >$ 0.05 *p.u.*.

$$\Delta P_s = P_{s,ref} - P_s = -\frac{1}{k_{droop}}(V_{DC,ref} - V_{DC}) \tag{2.2.7}$$

$$P_{s,droop} = P_s + \Delta P_s \tag{2.2.8}$$

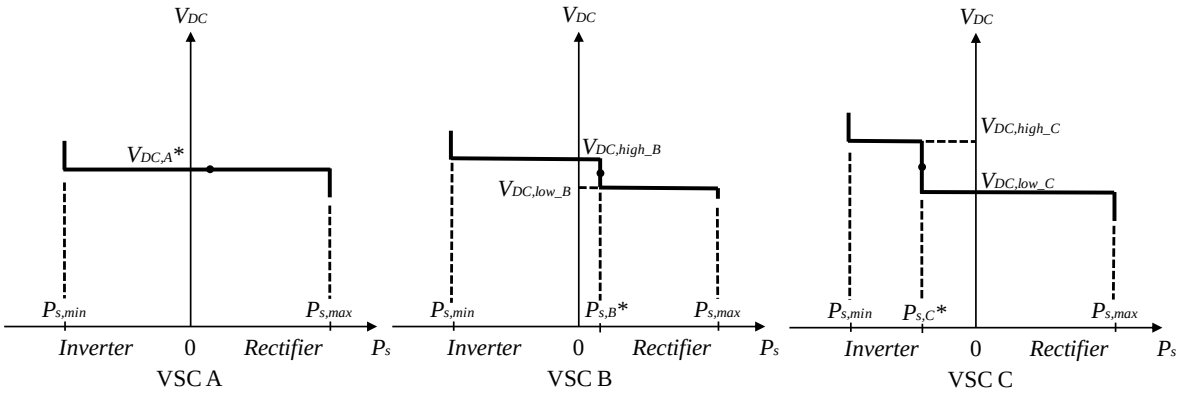

Fig. 2.14. Example of DC voltage margin control of a multi-terminal VSC HVDC system

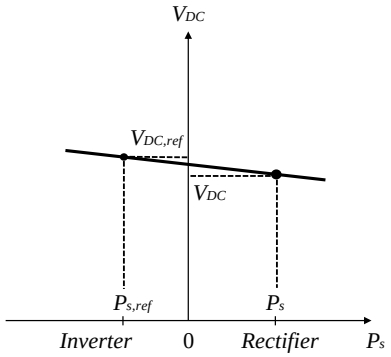

Fig. 2.15. DC voltage droop control of a VSC

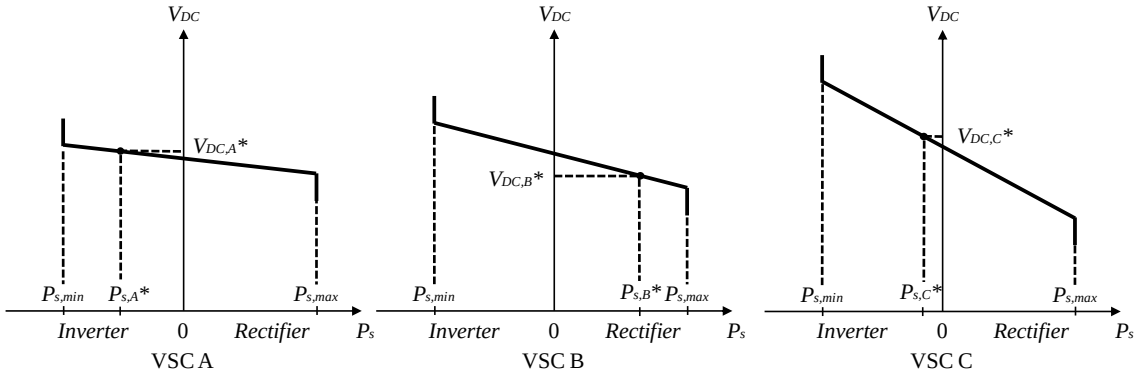

Fig. 2.16. Example of DC voltage droop control of a multi-terminal VSC HVDC system

Considering the power supply and demand imbalance, VSC HVDC systems are also required to equip with the FRT capability [33]. When a PCC bus voltage drop below V_{block} is measured, the corresponding VSC is blocked. A VSC converter is allowed to be disconnected when the PCC bus voltage drop fails to satisfy the FRT requirement in Fig. 2.17.

The FRT grid code for VSC HVDC systems in [33] where the ranges of voltage and time parameters are defined is quoted. The adopted voltage and time parameters for the FRT grid code of VSC HVDC systems are listed in Table 2.3. Except V_{block} and T_{rec2}, the parameters are selected

to be able to endure the most severe condition. V_{rec2} is determined considering the lower limit of AC bus voltage constraint of the OPF analysis in the normal state. In this analysis, V_{rec2} = 0.9 *p.u.*. Regarding V_{block}, it is set as 0.2 *p.u.*, but different V_{block} criteria can also be applied depending on system operators.

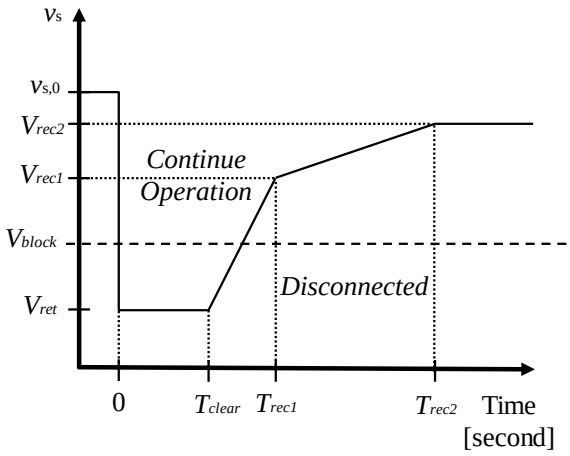

Fig. 2.17. FRT requirement of VSC HVDC system [33]

Table 2.2. Voltage and time parameter ranges of FRT requirements in Fig. 2.17 [33]

***Voltage parameters* [*p.u.*]**		***Time parameters* [*seconds*]**	
V_{ret}	0.00 – 0.30	T_{clear}	0.14 – 0.25
V_{rec1}	0.25 – 0.85	T_{rec1}	1.5 – 2.5
V_{rec2}	0.85 – 0.90	T_{rec2}	T_{rec1} – 10
V_{block}	*adjustable by each TSO*		

Table 2.3. Voltage and time parameters of FRT requirement

***Voltage parameters* [*p.u.*]**		***Time parameters* [*seconds*]**	
V_{ret}	0	T_{clear}	0.25
V_{rec1}	0.85	T_{rec1}	1.5
V_{rec2}	0.90	T_{rec2}	5
V_{block}	0.20		

2.3 Protection Strategy of Mixed AC / VSC HVDC System

Currently, several HVDC system protection methodologies against a DC fault have been developed [3], which is briefly summarized in this dissertation.

For starters, AC grid side breakers at converter stations can be used for the DC fault clearance. Since mechanical AC breakers are used, this takes several cycles of the fundamental AC frequency, which is relatively slow compared to other methods. Moreover, this method leads to the loss of the entire HVDC system during several fundamental AC frequency cycles. Hence, this protection is proper for HVDC systems with small-scale point-to-point or simple configurations. DC grid is needed to be re-energized before it is brought back to pre-fault operation. In this context, MMC HVDC systems without any aggregated DC capacitor of VSC converter are advantageous.

The second method is utilizing converters with the fault-blocking capability. The DC fault blocking behavior of this method is fast and it does not require any DC circuit breakers. Nevertheless, the whole HVDC grid is also lost by this method. All converters should have the fault-blocking capability to apply this method.

The last method is adopting DC circuit breakers (CB). Current waveforms in AC systems have natural zero current moments. AC fault current extinction can be carried out using these natural zero current moments. On the other hand, due to the absence of natural zero DC current moments, the capability of making artificial zero DC current is required for DC CB technologies. A HVDC grid is classified into different protection zones using DC CB. Unlike the previous methods, selective DC fault clearance is possible by this approach. Normally, each DC transmission line is classified as an individual protection zone.

Normally, three types of DC CB are discussed to be utilized in HVDC systems. The mechanical-type-based DC CB is the most economical. However, the operation speed of this DC CB type is the slowest. The solid-state-type DC CB is the fastest DC fault clearance approach. Nevertheless, the expensive cost and large on-state loss are the limitations.

In order to overcome these drawbacks of two previous DC CB types, hybrid-type DC CB is proposed. This DC CB type is more economical and has acceptable on-state loss compared to the solid-state-type DC CB. In addition, this hybrid-type DC CB is still able to clear a DC fault selectively with acceptable speed [4], [34]. In this context, this hybrid-type DC CB is evaluated as the most practical method for multi-terminal VSC HVDC systems. Therefore, this hybrid-type DC CB is adopted for DC fault clearance in this dissertation.

The DC fault clearing time consist of breaking time and fault clearance time [34]. The breaking time and the fault clearance time indicate the rising current and the decreasing current periods respectively. Short breaking time is desirable to obtain low maximum current breaking capability and as a result, low DC CB costs [34]. Here, the DC fault current clearance with 2ms breaking time and 3ms fault clearance of hybrid-type DC CBs described in Fig. 2.18 [34] are considered.

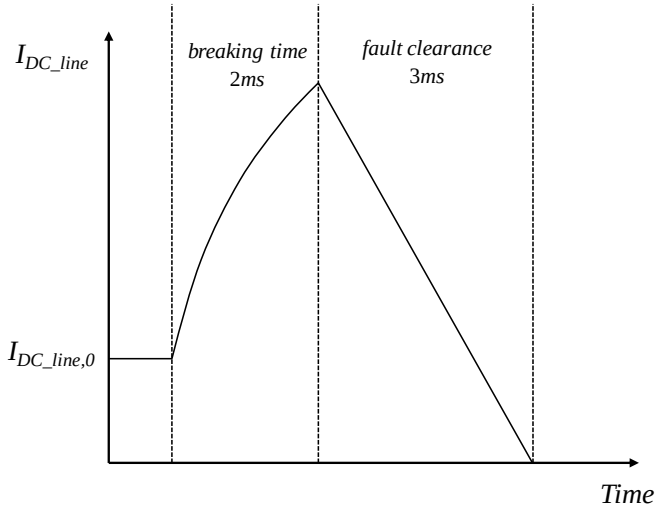

Fig. 2.18. DC fault current extinction model by hybrid-type DC circuit breaker [4], [34]

When a bipole-to-ground DC fault occurs in a VSC HVDC system, the nearby VSC is blocked. The DC voltage at the fault location drops to zero [35] unlike a single pole-to-ground fault. DC CBs are activated to remove the fault selectively and make artificial zero DC current. The DC transmission line on the fault location are opened after the fault clearance time, 5ms. This line is opened until the de-ionization of the DC faulted line is completed, which typically requires 150ms [36]. After that, the faulted line can be reclosed and VSC can be de-blocked at 155ms.

It should be reminded that the DC voltage at the fault location is zero. This DC voltage is needed to be recovered, which is named as 'V_{DC} recovery process'. If the faulted DC line is re-operated without this voltage recovery process, large DC voltage differences between the fault location and other DC buses lead to huge DC current flows. This can damage HVDC grid facilities and even re-trigger DC fault protection process.

The concept of V_{DC} recovery process is described in Fig. 2.19 in which a point-to-point VSC HVDC system is considered for a simple explanation. A DC fault occurs and is cleared by the hybrid DC CBs on the faulted DC transmission line. The DC CBs on the faulted DC line are opened until 155ms for the complete de-ionization. The DC voltage at the fault location $V_{DC,1}$ is zero.

After t = 155ms, the blocked VSC can be de-blocked and V_{DC} recovery process is activated. The DC CBs are still opened during V_{DC} recovery process. The de-blocked VSC supplies active power towards the DC grid to charge the DC capacitor $C_{DC,1}$ of the fault location. In other words, active power is supplied from AC grid towards DC grid by the de-blocked VSC.

From another point of view, this V_{DC} recovery process gives substantial influence on AC grids. This concern grows as the capacity of a VSC HVDC system increases. Especially, the PCC bus voltages at wind-farm-connected buses are needed to be controlled carefully for proper operations of wind farms. From this aspect, the following procedure is proposed to relieve the burden of AC grid side. After a VSC is de-blocked, the VSC is also assigned to produce its pre-fault reactive power output for effective AC bus voltage control. This can be achieved by returning its reactive power output reference Q_s^* as the pre-fault value $Q_{s,0}$. The rest of the VSC capacity $-\sqrt{S_{vsc,\max}^2 - Q_s^{*2}}$ is allocated to recharge C_{DC} by supplying active power.

This recovery process continues until the DC voltage at the fault location $V_{DC,1}$ recovers above a certain threshold, $V_{DC,r}$. Here, $V_{DC,r}$ is set to be 0.8 *p.u.* After that, the DC circuit breakers are re-closed. The de-blocked VSC operation mode is switched to the pre-fault control mode.

This whole protection strategy process is summarized in Fig. 2.20.

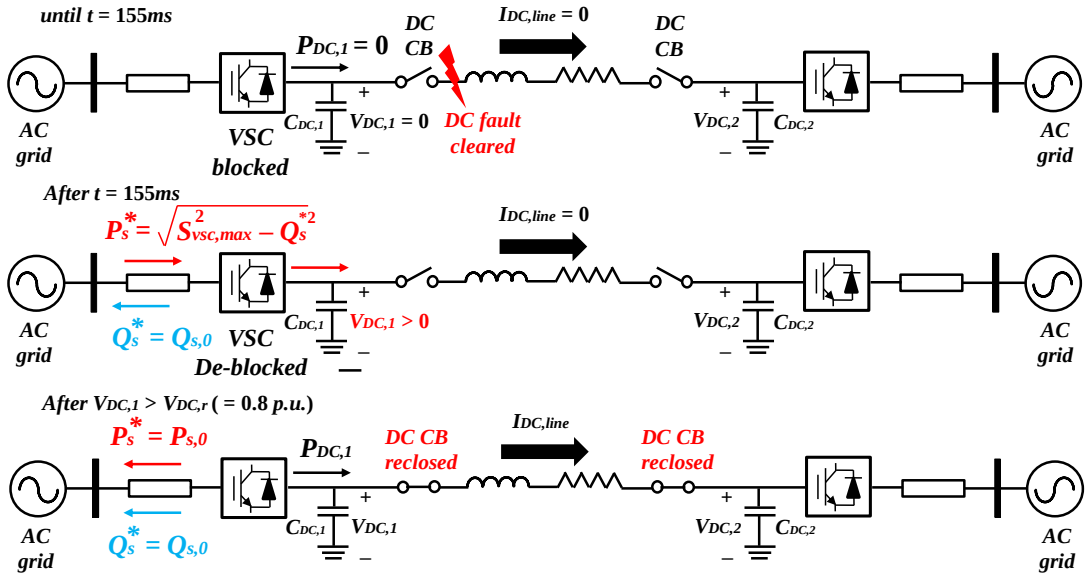

Fig. 2.19. Concept of V_{DC} recovery process

	DC grid	*AC grid*
	VSC blocked	
Stage 1	$P_{DC} = 0$, $I_{DC\_line,f} \uparrow$, $V_{DC,f} \downarrow$	
Stage 2 ($V_{DC,f} = 0$)	$I_{DC\_line,f} \uparrow$ (but after hybrid DC CB breaking time, $I_{DC\_line,f} \downarrow$)	$i_s = 0$, $P_s = 0$, $Q_s = 0$
	$I_{DC\_line,f} = 0$, DC lines near fault : opened at 5ms	
	De-ionization during 150ms	
Stage 3	*at 155ms, VSC de-blocked,*	
	opened DC lines : reconnected,	
	$V_{DC,f}$ *recovery starts*	

Fig. 2.20. Protection strategy of mixed AC / bipole VSC HVDC system against a DC bipole-to-ground fault

2.4 Power System Models

The IEEJ EAST 10-machine System Model [37] is adopted to simulate the installation of wind power plants in Japan. Base Case system model in Fig. 2.21 is composed of two areas. The upper area has low-demand and high wind potential. Considering this wind potential, two wind farm units are installed in the upper area. Both wind farms produce active power with unity power factor. In contrast, the amount of load demand in the lower area is larger than that in the upper area. These two areas are interconnected via the tie-line; the line between AC buses (36) and (17).

Six thermal power plant models; G1, G4, G6, G8, G9, and G10 are included in the system model. G6 is assigned as the slack generator. G2 and G7 represent the nuclear power plant models. G3 and G5 correspond to the pump-storage hydro power plant models. The detailed system data can be seen in [37]. In order to reflect the reduced role of the thermal power plant units, the minimum active power production limits of these units are adjusted to the minimum productions of their respective single generator units as can be seen in Table C.3 in Appendix.

Considering the N-1 criterion, each single-circuit AC transmission line can operate up to 140% overload power flow of its rated capacity for 10 minutes. The loads in the upper area have leading 0.95 power factor. The loads in the lower area have lagging 0.95 power factor. All loads are calculated as static constant impedance load models. It is assumed that sufficient amounts of shunt reactors and capacitors are already prepared by the system operator at the load buses for AC bus voltage adjustments. As regards the tap transformer settings, discretized tap ratio settings with 0.005 *p.u.* unit tap step between the lower and upper ratio boundaries are allowed for all tap transformers.

The system reinforcement by either three or four-terminal 500kV bi-pole VSC HVDC system is considered as plotted in Fig. 2.22 if required for the large-scale wind farm installations. The transmission line lengths of DC overhead lines 1 and 2 are 600km. The length of DC overhead line 3 of a four-terminal VSC HVDC system is 100km.

The VSC converters 1 and 2 near the wind farms control their active and reactive power outputs with the control systems in Fig. 2.8 and Fig. 2.10. In order to focus only on the AC grid stabilization effect, these two VSCs near the wind farms are not equipped with the DC voltage droop control. Among the rest of VSCs, either VSC 3 or VSC 4 can be selected as the VSC slack. In the three-terminal VSC HVDC system, VSC 3 is assigned as the VSC slack. In the four-terminal VSC HVDC system, VSC 4 is the slack converter. In fact, it has been revealed in the preliminary investigations that the OPF results are hardly influenced by the location of the VSC slack when transient stability analysis investigations are not considered. In the transient stability analysis, due to the absence of the active power output controller of the VSC slack, the system stabilization effect of the VSC slack on AC grid side is less than other VSC converters. In addition, the DC voltage control of the VSC slack is carried out by adjusting the active power output of the VSC slack. This active power output adjustment can lead to the destabilization effect on the nearby AC grid. Thus, it is desired for the VSC slack to be installed near a strong AC network side [29]. Hence, the VSC near G2, G3, G4, and G5 with relatively large rated capacities is selected as the VSC slack when considering the transient stability investigations. Regarding the three-terminal VSC HVDC system, the V_{DC} droop control is not utilized since without VSCs 1 and 2, only VSC 3 is capable of

controlling DC bus voltage. The control system parameters of VSC HVDC systems in Table 2.4 and Table 2.5 are adopted. These parameters are tuned by trial and error process to enable a large-scale wind power production considering small-signal stability and transient stability viewpoints.

In the transient stability analysis, a three-phase line-to-ground fault and a bipole-to-ground fault are simulated as the types of AC and DC faults respectively. Ideally, the OPF solution with transient stability constraints is able to maintain stability against all faults in the whole system. To this end, all AC and DC fault locations should be considered in the transient stability analysis. However, only representative AC and DC fault locations notated in Fig. 2.21 and Fig. 2.22 are taken into account to reduce computational burden. This simplification is still valid by only selecting critical faults in the system model. The AC fault locations are chosen based on the locations explained in [37] and near VSC stations. Similarly, the DC fault locations near VSC stations are selected as well.

The investment costs of system reinforcements follow the values in Table 2.6. The reinforcement of each device of a multi-terminal VSC HVDC system up to the corresponding capacity in Table 2.7 is allowed.

The reinforcements with AC transmission systems in Fig. 2.23 are also considered for the case comparisons. The AC reinforcements using only the existing transmission paths are included in New AC system 1. The reinforcements using the new transmission paths in Fig. 2.23 are taken into account in New AC system 2. The AC reinforcement paths in New AC system 1 are classified into four groups. The reinforcement capacities of the transmission lines belong to the same group are assumed to be same to reduce the number of control variables in the optimization process. This assumption is applied to New AC system 2 as well. As for the reinforcement capacities, up to the capacities in Table 2.8 are allowed considering the large-scale wind farm installations. Less than the single-circuit AC transmission line capacity; 6.7GW is not allowed for the new transmission line paths of AC groups *1b* and *2b* in New AC system 2.

Regarding the maximum reinforcement capacities of AC transmission systems, the installations up to double-circuit AC transmission line; 2×6.7GVA for each reinforcement group are considered in New AC system 2. New AC system 1 also has the same maximum reinforcement capacity except AC group *1a*. Since up to two double-circuit AC transmission lines can be installed between the upper and the lower areas in New AC system 2, the reinforcement with up to quadruple-circuit transmission line is taken into account for AC group *1a* in New AC system 1 for the balanced simulation condition with New AC system 2. The maximum MTDC reinforcement capacities in Table 2.7 are also close to these maximum AC transmission reinforcement capacities.

The investment costs of VSC HVDC system devices and AC transmission systems are listed in Table 2.6 and Table 2.8. According to these investment costs in Table 2.6, the same investment cost is obtained for both point-to-point AC and VSC HVDC 600km overhead transmission systems when neglecting the DC circuit breaker costs.

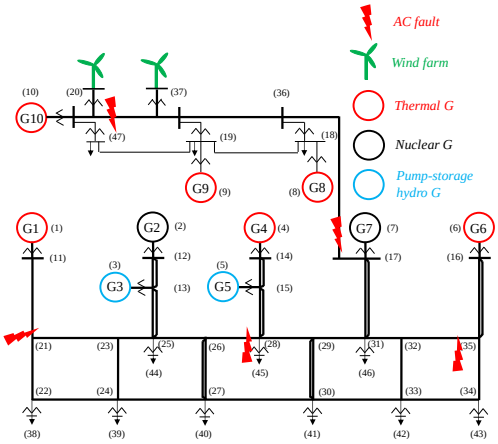

Fig. 2.21. Base Case system model with wind farms

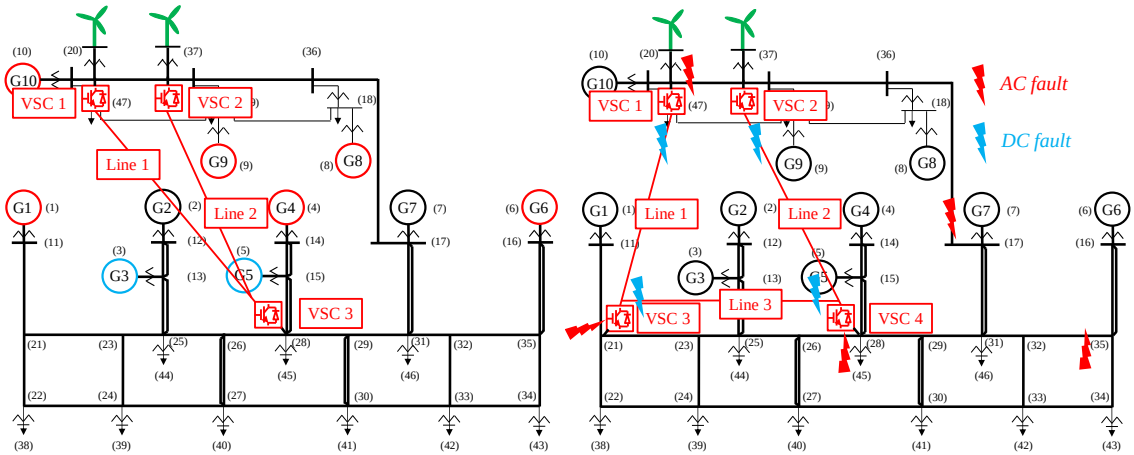

Fig. 2.22. Mixed AC / multi-terminal VSC HVDC system models (left : three-terminal, right : four-terminal)

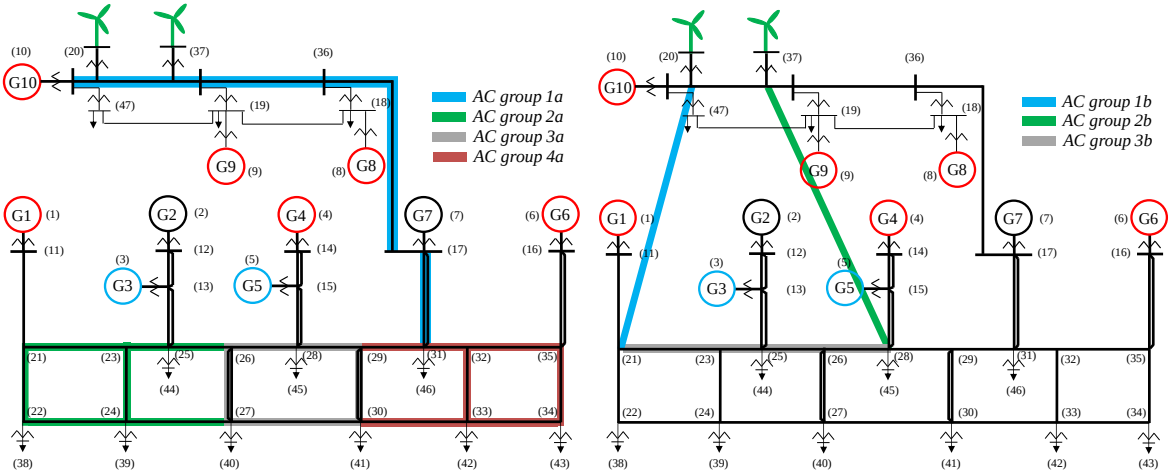

Fig. 2.23. System models with AC transmission reinforcements (left : New AC system 1, right : New AC system 2)

Table 2.4. Parameters of three-terminal VSC HVDC control system

Unit : [*p.u.*]

	k_{droop}	k_{pi}	k_{ii}	$k_{p,P}$	$k_{i,P}$	$k_{p,DC}$	$k_{i,DC}$	$k_{p,Q}$	$k_{i,Q}$
VSC 1		1	20	1	2			1	2
VSC 2									
VSC 3						10	30		

Table 2.5. Parameters of four-terminal VSC HVDC control system

Unit : [*p.u.*]

	k_{droop}	k_{pi}	k_{ii}	$k_{p,P}$	$k_{i,P}$	$k_{p,DC}$	$k_{i,DC}$	$k_{p,Q}$	$k_{i,Q}$
VSC 1		1	20	1	2			1	2
VSC 2									
VSC 3	0.1								
VSC 4	0.1					10	30		

Table 2.6. Investment costs of reinforcement devices [2]

Device	**Cost**	**Unit**
500kV VSC	14,000,000	JPY / MVA
500kV bidirectional hybrid type DC circuit breaker	7,000,000	JPY / MVA
500kV DC overhead line	16,700	JPY / (km × MW)
500kV AC substation	4,000,000	JPY / MVA
500kV AC overhead line	50,000	JPY / (km × MVA)
AC group 1a	38,000,000	JPY / MVA
AC group 2a	32,000,000	JPY / MVA
AC group 3a	23,000,000	JPY / MVA
AC group 4a	32,000,000	JPY / MVA
AC group 1b	38,000,000	JPY / MVA
AC group 2b	38,000,000	JPY / MVA

Table 2.7. Maximum reinforcement capacities of multi-terminal VSC HVDC systems

System	Device	Maximum reinforcement capacity
Three-terminal VSC HVDC	VSC 1	12 GVA
	VSC 2	
	VSC 3	2 × 12 GVA
	DC line 1	12 GW
	DC line 2	
Four-terminal VSC HVDC	VSC 1	12 GVA
	VSC 2	
	VSC 3	
	VSC 4	
	DC line 1	12 GW
	DC line 2	
	DC line 3	

Table 2.8. Components of New AC system reinforcements

System	Number of substations	AC overhead line length	Maximum reinforcement capacity
AC group *1a*	2 (at loads 20 and 31)	600km	4 × 6.7 GVA
AC group *2a*	3 (at loads 38, 39, and 44)	400km	2 × 6.7 GVA
AC group *3a*	3 (at loads 40, 41, and 45)	220km	
AC group *4a*	3 (at loads 42, 43, and 46)	400km	
AC group *1b*	2 (at the left wind farm and load 21)	600km	2 × 6.7 GVA
AC group *2b*	2 (at the right wind farm and load 28)	600km	
AC group *3b*	0	100km	

Table 2.9. Fault numbering

AC fault near VSC 1	AC fault 1
AC fault near G7 (AC tie-line side fault)	AC fault 2
AC fault near VSC 3 (close to AC bus 21)	AC fault 3
AC fault near VSC 4 (close to AC bus 28)	AC fault 4
AC fault close to AC bus 35	AC fault 5
DC fault near VSC 1	DC fault 1
DC fault near VSC 2	DC fault 2
DC fault near VSC 3	DC fault 3
DC fault near VSC 4	DC fault 4

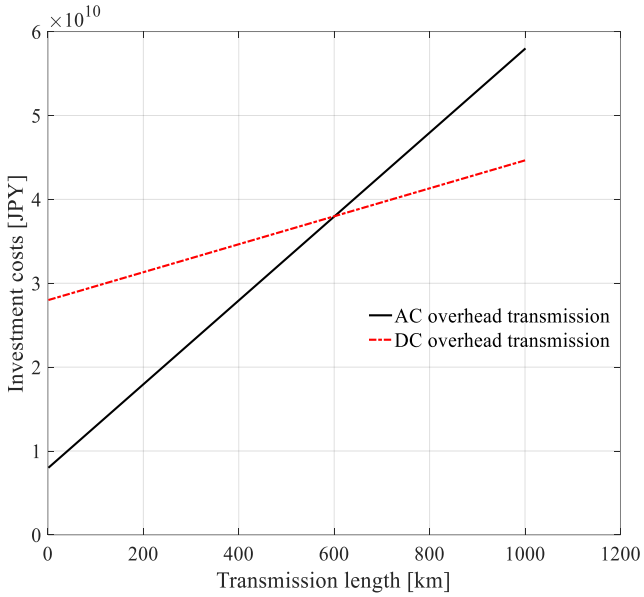

Fig. 2.24. Investment cost comparison between AC and DC overhead transmission (except DC circuit breaker costs)

3. Stability Constrained Optimal Power flow in Mixed AC / Multi-Terminal VSC HVDC System with Wind Power Plants

3.1 Multi-Period Classification

Regarding power system reinforcement planning, the long-term economic benefit analysis during the life-time of the reinforcement facilities is necessary. However, a significant computational burden is required for this economic benefit investigations during several decades. In order to overcome this barrier, a simplified annual economic benefit analysis is applied.

Every year during the entire life-time of the reinforcement facilities has the same amount of load consumptions. As a result, the economic benefit analysis can be carried out only for one year. The annual result is multiplied by a coefficient to obtain the total economic benefits during the entire life-time. one year is classified into several multi-periods considering four seasons and two load patterns of the environments in Japan. In order to reflect wind power output variations, three wind power output patterns; low, average, and peak wind outputs and the corresponding time ratios R_{low}, R_{aver}, and R_{peak} are taken into account. The parameters of the wind outputs and the time ratios are decided considering the environment in Japan. All 18 sections in Table 3.1 are treated to be mutually exclusive.

As a consequence, the annual fuel cost of a mixed AC / multi-terminal VSC HVDC system and the wheeling charge of a VSC HVDC system are obtained by calculating the costs of all 18 sections. As for the annual fuel cost, the fuel costs with the low ($F.C._{low}$), average ($F.C._{aver}$), and peak ($F.C._{peak}$) wind productions in a period are calculated. These costs are multiplied by their respective time ratios. The results are summed up to obtain the fuel cost in a period $F.C._{period}$ in (3.1.1). The annual fuel cost in year 't' $F.C._{annual,t}$ is calculated by summing up all periodical fuel costs which are multiplied by $k_{p\_to\_y}$ in (3.1.2). The annual wheeling charge in year 't' $HVDC_{wh,annual,t}$ is obtained in the same way. Based on the sectional and periodical wheeling charge costs in (3.1.3), $HVDC_{wh,annual,t}$ can be obtained by the sum of all periodical wheeling charge costs multiplied by $k_{p\_to\_y}$ in (3.1.4).

$$F.C._{period} = R_{low} \times F.C._{low} + R_{aver} \times F.C._{aver} + R_{peak} \times F.C._{peak} \quad (3.1.1)$$

$$F.C._{annual,t} = k_{p\_to\_y} \times \Sigma\, F.C._{all\ periods} \quad (3.1.2)$$

$$HVDC_{wh,period} = R_{low} \times HVDC_{wh,low} + R_{aver} \times HVDC_{wh,aver} + R_{peak} \times HVDC_{wh,peak} \quad (3.1.3)$$

$$HVDC_{wh,annual,t} = k_{p\_to\_y} \times \Sigma\, HVDC_{wh,all\ periods} \quad (3.1.4)$$

$k_{p\_to\_y}$ Coefficient converting periodical cost to annual cost
(= (365 days / 4 seasons) × (24 hours / 2 periods))

Table 3.1. Multi-period classification of one year

Season	Load pattern	Total load [GW]	Wind output / capacity	Time ratio	Section number
Spring = Autumn	Peak-load (Period 1)	55.5	2%	R_{low} = 30%	1
			27.5%	R_{aver} = 60%	2
			100%	R_{peak} = 10%	3
	Low-load (Period 2)	28.8	2%	R_{low} = 30%	4
			27.5%	R_{aver} = 60%	5
			100%	R_{peak} = 10%	6
Summer	Peak-load (Period 3)	76.0	2%	R_{low} = 33%	7
			15%	R_{aver} = 62%	8
			100%	R_{peak} = 5%	9
	Low-load (Period 4)	36.0	2%	R_{low} = 33%	10
			15%	R_{aver} = 62%	11
			100%	R_{peak} = 5%	12
Winter	Peak-load (Period 5)	62.5	2%	R_{low} = 25%	13
			40%	R_{aver} = 60%	14
			100%	R_{peak} = 15%	15
	Low-load (Period 6)	32.9	2%	R_{low} = 25%	16
			40%	R_{aver} = 60%	17
			100%	R_{peak} = 15%	18

3.2 Hierarchical Stability Constrained Optimal Power Flow

The proposed hierarchical optimal power flow analysis consists of two separate steps. In the first step, the investment cost of a system reinforcement planning is determined. The maintenance costs of the reinforced systems are neglected for the simplicity. Based on the system reinforcement planning in the first step, the optimal operation in each time section is calculated in the second step to obtain the system fuel cost and the wheeling charge.

Step 1 – Transmission Expansion Planning Stage

The optimization problem (3.2.1) – (3.2.15) is solved to determine the system reinforcement planning in Step 1. Only six sections with peak wind production conditions: Sections 3, 6, 9, 12, 15, and 18 are solved in Step 1 considering that the main purpose of the transmission system reinforcement is the wind power transmission.

$$\textit{min} \quad f_{Total}(x_0,u_0) = f_1 + f_{Inv,hour} + penalty \tag{3.2.1}$$

$$\textit{subject to} \quad g_0(x_0,u_0) = 0 \tag{3.2.2}$$

$$h_0(x_0,u_0) \le 0 \tag{3.2.3}$$

$$g_k(x_k,u_k) = 0 \tag{3.2.4}$$

$$h_k(x_k,u_k) \le 0 \tag{3.2.5}$$

$$|u_k - u_o| \le \Delta u_k \tag{3.2.6}$$

$$All\ real\ (\lambda) < \sigma_{max,0} \tag{3.2.7}$$

$$\xi = \frac{-\sigma}{\sqrt{\sigma^2+\omega^2}} \ge \xi_{\min} \tag{3.2.8}$$

$$|\delta_i(t) - \delta_{COI}(t)| \le \delta_{max} \tag{3.2.9}$$

$$v_{s,min} \le v_s(t) \le v_{s,max} \tag{3.2.10}$$

$$V_{DC,min} \le V_{DC}(t) \le V_{DC,max} \tag{3.2.11}$$

$$|I_{DC,line}(t)| \le k_{Th} \times I_{DC,line,rated} \tag{3.2.12}$$

where

$$f_1 = \sum_{G\in N_g}(C_G + B_G P_G + A_G P_G^2) \tag{3.2.13}$$

$$f_{Inv,hour} = \frac{CRF \times f_{Inv,total}}{365\times 24} \tag{3.2.14}$$

$$CRF = \frac{ir(1+ir)^{LT}}{(1+ir)^{LT}-1} \tag{3.2.15}$$

0	Normal state 0
k	Contingency case k
x	State variable vectors
u	Control variable vectors
Δu_k	Control variable re-dispatch capability
G	Generator G
P_G	Active power productions of generators
A, B, C	Fuel cost coefficients
g	Set of equality constraints
h	Set of inequality constraints
λ	Eigenvalue
σ	Real part of an eigenvalue
ω	Imaginary part of an eigenvalue
ξ	Damping ratio of an eigenvalue
δ	Rotor-angle of generator or Center of Inertia
COI	Center of Inertia
$I_{DC,line}$	DC line current
$I_{DC,line,rated}$	Rated value of DC line current
ir	annual interest rate
LT	Life-time of VSC HVDC system
CRF	Capacity ratio factor

Objective function of Step 1

The objective function f_{Total} (3.1.1) consists of the hourly fuel cost f_1 of a system model and the hourly investment cost of a reinforcement planning $f_{Inv,hour}$ in each period. f_1 is defined by the sum of the quadratic functions of thermal power plant productions P_G using the fuel cost coefficients A_G, B_G, and C_G.

The total investment cost of a reinforcement planning $f_{Inv,total}$ is converted to the hourly investment cost $f_{Inv,hour}$ using the concepts of (3.2.14) and (3.2.15) to be integrated in f_{Total} [38]. For the life-time LT of the system reinforcement facilities, the annual interest rate ir is considered. In this analysis, LT and ir are considered as 30 years and 1% respectively. If one of the constraints is not satisfied, a large *penalty* value is added to the objective function value.

It is worth noting that not only the system reinforcement costs, the hourly operation cost f_1 is also taken into consideration in Step 1. The purpose of this objective function is to obtain the effective solution considering both the system reinforcement and operation aspects. In other words, without f_1 in the objective function in Step 1, the possibility where an impractical system operation cost is obtained exists.

As a consequence, the cost results of f_1 and $f_{Inv,hour}$ are obtained by Step 1. However, only the investment cost result $f_{Inv,hour}$ is utilized since the fuel cost result f_1 of Step 1 is not the final optimal solution from the operation cost viewpoint. Therefore, additional optimization process is required

to find the optimal operation condition, which corresponds to the second step of the hierarchical OPF analysis.

Control variables

The objective of OPF analysis is to find the optimal objective function value by adjusting controllable variables in a power system model. The control vector *u* consists of all controllable variables.

Similar to the conventional OPF analysis, *u* includes the active power productions and the terminal bus voltage magnitudes of thermal power plants in AC grids. It should be noted that if a thermal power plant is assigned as the slack generator of an AC grid, the active power production of the plant is not controllable in the OPF analysis. In addition, the reactive power outputs of shunt reactors, capacitors, and tap transformer ratio settings are also included in the control vector *u* to adjust AC bus voltages. Furthermore, the active and reactive power outputs of VSC converters are also the components of *u* in cases of mixed AC / VSC HVDC systems. As with AC grids, the active power output of the slack VSC is not controllable.

In Step 1, *u* includes the reinforcement capacities of transmission systems as well. For example, the reinforcement capacities of *AC groups 1a*, *2a*, *3a*, and *4a* are calculated as the controllable variables of New AC system 1 in Step 1 analysis. Similarly, the capacities of VSCs 1 ~ 4 and DC lines 1 ~ 3 are handled to be controllable of four-terminal VSC HVDC system in Step 1 analysis. On the contrary, these reinforcement capacities are not classified as the controllable variables in Step 2.

Equality Constraints

Active power balance at all AC grid buses

$$P_{G,AC,j} - P_{AC\_load,j} + P_{VSC,AC,j} = P_{AC,j} \tag{3.2.16}$$

Reactive power balance at all AC grid buses

$$Q_{G,AC,j} - Q_{AC\_load,j} + Q_{VSC,AC,j} = Q_{AC,j} \tag{3.2.17}$$

Active power balance at all DC grid buses

$$P_{G,DC,j} + P_{VSC,DC,j} - P_{DC\_load,j} = P_{DC,j} \tag{3.2.18}$$

j	Bus number
$P_{G,AC}$	Active power injection by generators in AC grid
$Q_{G,AC}$	Reactive power injection by generators in AC grid
P_{AC_load}	Active power consumption by AC loads
Q_{AC_load}	Reactive power consumption by AC loads
$P_{VSC,AC}$	VSC active power injection into AC grid
$Q_{VSC,AC}$	VSC reactive power injection into AC grid
P_{AC}	Net active power injection into AC grid
Q_{AC}	Net reactive power injection into AC grid
$P_{G,DC}$	Active power generation in DC grid
$P_{VSC,DC}$	VSC active power injection into DC grid
P_{DC_load}	Active power consumption by DC loads
P_{DC}	Net active power injection into DC grid

Inequality Constraints

The active, reactive, and apparent power outputs of synchronous generators are constrained by their respective lower and upper production limits from (3.2.19) to (3.2.21). The upper production limit values of the generators in [37] are referred. As for the lower production limits of thermal power plants, the limit of single generator unit is considered. For example, G1 model with 7,000MW rated active power production consists of ten generator units. The minimum active power production limit of single G1 generator unit is 140MW. In this case, the lower and upper active power production limits of G1 are 140MW and 7,000MW respectively.

The active, reactive, and apparent power productions of a VSC are also limited by their respective lower and upper limits from (3.2.22) to (3.2.24). The apparent power production upper limit is determined by the capacity of a VSC converter. For instance, the lower and upper limits of VSC apparent power outputs are zero and 1GVA if the VSC capacity is 1GVA.

The lower and upper production limit magnitudes of a VSC active power output are identical to the VSC capacity. The primary purpose of installing a VSC HVDC system is the active power transmission of wind power plant outputs and AC grids. Hence, the maximum production capability of a VSC is directly applied to the lower and upper production limits of the VSC active power output.

The lower and upper production limit magnitudes of a VSC reactive power output are also decided by the VSC capacity. For example, the lower and upper limits of a VSC reactive power output are –1GVAR and 1GVAR if the VSC capacity is 1GVA.

All bus voltage magnitudes of AC and DC grids are constrained between 0.9 *p.u.* and 1.1 *p.u.* in normal operations by (3.2.25) and (3.2.26). The ratios of all tap transformers R_{tap} are limited between the minimum ratio 0.95 and maximum ratio 1.05 in (3.2.27). The active power flow results via all AC and DC transmission lines are limited within their respective transmission line capacities in (3.2.28) and (3.2.29).

Lower and upper limits of AC generator active power output

$$P_{G,AC,i}^{\min} \le P_{G,AC,i} \le P_{G,AC,i}^{\max} \tag{3.2.19}$$

Lower and upper limits of AC generator reactive power output

$$Q_{G,AC,i}^{\min} \le Q_{G,AC,i} \le Q_{G,AC,i}^{\max} \tag{3.2.20}$$

Lower and upper limits of AC generator apparent power output

$$S_{G,AC,i}^{\min} \le S_{G,AC,i} \le S_{G,AC,i}^{\max} \tag{3.2.21}$$

Lower and upper limits of VSC converter active power output

$$P_{VSC,AC,i}^{\min} \le P_{VSC,AC,i} \le P_{VSC,AC,i}^{\max} \tag{3.2.22}$$

Lower and upper limits of VSC converter reactive power output

$$Q_{VSC,AC,i}^{\min} \le Q_{VSC,AC,i} \le Q_{VSC,AC,i}^{\max} \tag{3.2.23}$$

Lower and upper limits of VSC converter apparent power output

$$S_{VSC,AC,i}^{\min} \le S_{VSC,AC,i} \le S_{VSC,AC,i}^{\max} \tag{3.2.24}$$

Lower and upper limits of AC bus voltage magnitude in the steady-state

$$V_{AC,j}^{\min} \le V_{AC,j} \le V_{AC,j}^{\max} \tag{3.2.25}$$

Lower and upper limits of DC bus voltage in the steady-state

$$V_{DC,j}^{\min} \le V_{DC,j} \le V_{DC,j}^{\max} \tag{3.2.26}$$

Lower and upper limits of tap transformer setting

$$R_{tap}^{\min} \le R_{tap} \le R_{tap}^{\max} \tag{3.2.27}$$

AC transmission line capacity limit

$$P_{AC,ij}^{\min} \le 0 \le P_{AC,ij} \le P_{AC,ij}^{\max} \tag{3.2.28}$$

DC transmission line capacity limit

$$P_{DC,ij}^{\min} \le 0 \le P_{DC,ij} \le P_{DC,ij}^{\max} \tag{3.2.29}$$

$S_{G,AC}$	Apparent power injection by generators in AC grid
$S_{VSC,AC}$	VSC apparent power injection into AC grid
V_{AC}	AC bus voltage
V_{DC}	DC bus voltage
R_{tap}	Tap ratio
$P_{AC,ij}$	Active power flow from AC bus *i* to AC bus *j*
$P_{DC,ij}$	Active power flow from DC bus *i* to DC bus *j*

In order for reliable power system operations, the operations are determined to be able to cope with contingency cases. In general, the N-1 criterion is adopted in power systems to guarantee reliable system operations against the malfunction of one facility. The word 'N-1' implies that a power system can be operated even one facility of the system is disabled. This N-1 criterion is included as the additional constraints (3.2.4) – (3.2.6) in this analysis. This OPF analysis is called security-constrained optimal power flow.

Given the contingency case *k*, the following post-fault analysis is solved to consider the N-1 criterion. The linearized DC OPF is adopted for this post-fault analysis. Thus, the constraints regarding bus voltage magnitudes and reactive power outputs are neglected. The aim of this post-fault analysis is to find the infeasibility of the OPF solution u_0 considering the re-dispatch of the control variables during 30 minutes after the contingency case *k*, $|u_k - u_0|$. If $|u_k - u_0|$ exceeds the upper limit of the control variable re-dispatch Δu_k, positive z_k and y_k values are detected. In such cases, it is classified that u_0 does not satisfy the N-1 criterion. u_0 is accepted as the feasible solution when a positive y_k is not detected for all contingency cases.

$$\begin{aligned}
&\textit{min} && e^T z_k = y_k && (3.2.30)\\
&\textit{subject to} && g_k(x_k, u_k) = 0 && (3.2.31)\\
& && h_k(x_k, u_k) \le 0 && (3.2.32)\\
& && |u_k - u_o| - \Delta u_k \le z_k && (3.2.33)\\
& && z_k \ge 0 && (3.2.34)
\end{aligned}$$

e	Unity vector
z	Positive slack variable
y	Total post-fault infeasibility index

The re-dispatch of control variables is not allowed in preventive security-constrained OPF analysis. Therefore, all elements of Δu_k are zero in such cases. Whereas the re-dispatch of control variables can be considered in corrective security-constrained OPF analysis [20]. Here, the control variables except thermal power plant outputs are able to re-dispatch their planning within their minimum and maximum operation ranges considering their fast ramp rate behaviors during 30 minutes. The outputs of pump-storage hydro power plants can also be adjusted freely within their minimum and maximum output limits. Therefore, Δu_k elements of these variables correspond to their respective minimum and maximum operation limits.

The re-dispatch of thermal power plants is carried out considering their ramp rate characteristics. In general, the ramp rate of a thermal power plant is the several percent of its rated power output per minute. Here, all thermal power plants are assumed to have 2% / minute of ramp rate for the simplicity. Hence, ±60% active power output re-dispatch is allowed for thermal power plants during 30 minutes as Δu_k.

The concept of thermal power plant re-dispatch is depicted in Fig. 3.1. For starters, it should be noted that a generator model represents the aggregated model of many single generator units. For example, the aggregated generator model G1 is composed of ten thermal power plant units. In general, it is desirable for a thermal power plant unit to operate close to its rated power output to obtain good efficiency. Hence, the minimum number of thermal power plant units in operation can be determined provided the total active power production of the aggregated thermal power plant model in the OPF solution. In Fig. 3.1, six thermal power plant units are required to produce $6 \times P_0$ of active power output. In the post-fault analysis, the productions of six thermal power plant units can be adjusted within their re-dispatch capabilities Δu_k as described in Fig. 3.1.

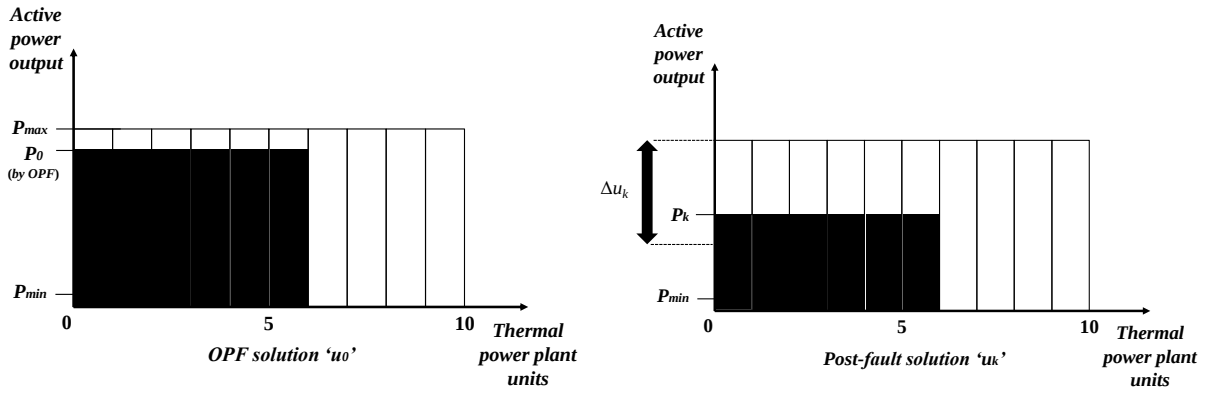

Fig. 3.1. Post-fault re-dispatch of thermal power plant units

The constraint (3.2.7) implies that all eigenvalues of a system model at an operating point should have the real parts less than $\sigma_{max,0}$. Here, $\sigma_{max,0}$ is zero to prevent unstable system operations. On top of that, it is well-known that critical oscillation modes, especially weakly damping electromechanical modes are often observed in AC grid operations. In order to guarantee well-damped behaviors of a system operation, (3.2.8) is also taken into consideration. Here, (3.2.8) is considered for the electromechanical modes with the oscillation frequencies between 0.05 – 3.0 Hz. Consequently, the oscillation modes are forced to have the damping ratios greater than or equal to

ξ_{min} by (3.2.8).

As for the transient stability constraints, the inequality constraints (3.2.9) – (3.2.12) are checked for ten seconds after a fault occurrence. In order to prevent generators from out of synchronism, the rotor-angle deviations of generators from COI $\delta_i - \delta_{COI}$ are constrained within a certain upper limit δ_{max} in (3.2.9). In the system models without any HVDC systems, the constraints (3.2.10) – (3.2.12) are not considered.

Improper behaviors of a VSC HVDC system can be observed in case of a significant PCC bus voltages v_s fluctuation after a fault. In addition, the wind generation units' FRT requirement may not be satisfied as well. Therefore, the fluctuations of v_s are also included as the additional constraints in (3.2.10) to prevent these problems. The constraint (3.2.10) indicates the deviations of v_s below $v_{s,min}$ or above $v_{s,max}$ are not allowed.

The constraints (3.2.11) and (3.2.12) are relevant to the transient DC grid behaviors. The most important DC grid index, DC grid voltage V_{DC} is considered in (3.2.11). The transient deviations of V_{DC} below $V_{DC,min}$ or above $V_{DC,max}$ are prohibited, which has the similar meaning as (3.2.10).

A DC overcurrent after a fault occurrence can give critical influences to VSC converters and DC transmission lines. From this viewpoint, the constraint (3.2.12) regarding DC transmission line current flow is considered. Considering a threshold ratio k_{Th} and the rated line capacity of each DC transmission line $I_{DC,line,rated}$, it indicates a DC current flow above the rated line capacity $I_{DC,line,rated}$ multiplied by the threshold ratio k_{Th} is not allowed. In fact, DC overcurrent threshold method is being adopted for the activations of DC grid protections in most HVDC applications. Of course DC grid protection is required in case of a DC fault occurrence, but the unnecessary DC grid protection activation after an AC fault should be avoided. The constraint (3.2.12) is needed considering this aspect as well.

The parameters for the transient stability constraints are listed in Table 3.2. The determination of these constraint parameters can differ depending on each transmission system operator. δ_{max} is 180° to prevent generators' out of synchronism in (3.2.9). The lower and upper voltage boundaries in (3.2.10) and (3.2.11); $v_{s,min}$, $v_{s,max}$, $V_{DC,min}$, and $V_{DC,max}$ are determined considering the conditions of system operation, AC / DC conversion of VSC converter, and insulation requirements of system facilities. As for k_{Th} in (3.2.12) is 150% considering the DC grid overcurrent protection threshold criterion.

Regarding the voltage constraints (3.2.10) and (3.2.11), it should be noted that a sudden large v_s drop during a VSC-side AC fault is inevitable. Similarly, a significant V_{DC} drop during a DC fault near a VSC always occur. Therefore, it is desirable for the constraints (3.2.10) and (3.2.11) to be considered after the influences of the fault are somehow cleared.

The concept of time delay parameters is adopted in this context. The transient voltage constraints (3.2.10) and (3.2.11) are checked after a certain time delay. These time delay parameters are determined considering AC and DC grid fault clearance and protection behaviors. In case of an AC fault occurrence near a VSC, the AC fault is removed after 1.07 seconds of the fault occurrence. Considering this aspect, the time delay for (3.2.10) is set as 1.5 seconds. When a DC fault occurs, it is desirable for the transient AC and DC bus voltages to be constrained after V_{DC} recovery process is completed. In preliminary investigations, 3 seconds are enough for V_{DC} recovery process of VSC

HVDC systems in this dissertation. Hence, the time delay of 3 seconds is adopted for (3.2.10) and (3.2.11) when a DC fault occurs. The time delay parameters for the transient stability constraints are summarized in Table 3.3. Different time delay parameters can be adopted depending on AC and VSC HVDC system behaviors.

Table 3.2. Parameters of transient stability constraints

δ_{max}	180 °
$v_{s,min}$	0.7 *p.u.*
$v_{s,max}$	1.3 *p.u.*
$V_{DC,min}$	0.7 *p.u.*
$V_{DC,max}$	1.3 *p.u.*
k_{Th}	150%

Table 3.3. Time delay parameters for transient stability constraints

Unit : [sec]

	AC fault	DC fault
(3.2.9)	0	0
(3.2.10)	1.5	3 (after V_{DC} recovery)
(3.2.11)	0	3 (after V_{DC} recovery)
(3.2.12)	0	0

As a result of Step 1 analysis, six different system expansion decisions in six peak wind output periods are determined. Among those results, the solution with the maximum capacity is adopted as the final reinforcement planning. For instance, if the reinforcement planning result of VSC 1 is 2GVA in Section 6 and those in other five sections are zero, 2GVA is adopted as the final VSC 1 reinforcement decision. Similarly, if the reinforcement result of AC group 1*a* transmission lines is 10GW in section number 3 and the results in other section numbers are less than 10GW, 10GW is adopted as the final reinforcement decision of AC group 1*a*.

Step 2 – System Operation Determination Stage

The system reinforcement planning is determined by Step 1. Based on this result, the objective of Step 2 is to find the optimal operations of all 18 sections. Therefore, the objective function of Step 2 is composed of only the operation cost term f_1 with the same constraints. Similarly, a large *penalty* value is also added to the objective function in case of the violation of one of the constraints.

As a consequence, the objective function value f_1 of Step 2 corresponds to the fuel cost *F.C.* of each time section. The wheeling charge of a multi-terminal VSC HVDC system in each time section $HVDC_{wh}$ is obtained based on the total transmitted energy E_{MTDC} multiplied by the unit wheeling charge Wh_{unit} in (3.2.36).

Objective function

$$min \quad f_{Total}(x_0, u_0) = f_1 + penalty \tag{3.2.35}$$

Wheeling Charge Calculation

$$HVDC_{wh} = Wh_{unit} \times E_{MTDC} \tag{3.2.36}$$

Wh_{unit} Unit wheeling charge [JPY / kWh]
E_{MTDC} Total transmitted energy by MTDC system

Optimization Algorithm

Differential evolution is adopted for the optimization process. First of all, the parent control vector set of control variables *u_set* is initialized randomly within their minimum and maximum limits. The power flow analysis is carried out and the constraints (3.2.2) – (3.2.8) are checked for each control vector *u*. If a constraint violation among (3.2.2) – (3.2.8) is observed by the *n*th control vector u_n, the corresponding large penalty value is added to its fitness value.

For the investigation of the transient stability constraints, time-domain simulation is executed for each control vector *u*. However, the analysis confronts the critical problem that it requires a significant calculation time caused by the time-domain simulation. In order to relieve this phenomenon, the infeasible vector filtering out method is proposed. Time-domain simulation is executed only for feasible control vectors as notated inside the dotted line in Fig. 3.2. If one of the constraints (3.2.2) – (3.2.8) is violated, time-domain simulation for the corresponding control vector is not carried out and instead, a huge penalty value is added. This is named as the infeasible vector filtering out process. The penalty value for this filtering out is set to be higher than other penalty values for the effective filtering.

After mutation and crossover stages, the trial vector set *w_set* is produced. In order to calculate the fitness values of the trial vectors, they undergo the same process with the same filtering out. After the *n*th vectors of *u_set* and *w_set* are compared each other, the one with the lower fitness value is chosen in the minimization problem. This procedure is repeated until the iteration number *K* exceeds the maximum iteration number K_{max} = 500. K_{max} is determined considering the convergence of the optimization process. More optimization computation is required as the numbers of control variables and constraints increase. The population size of DE is 100. The entire optimization process using DE is described in Fig. 3.2.

The dynamic behaviors of the OPF solution also depend on the control system parameters. In this dissertation, the objective of the optimization process is to calculate the optimal operation cost, not the optimal control parameters. This indicates that if the solution with the optimal operation cost can be found, any control parameters satisfying the constraints (3.2.2) – (3.2.8) can be utilized. In order to find the effective control parameters, the control parameters can also be included as the control vector elements of evolutionary algorithm. If a system operator already has the knowledge of effective control parameters, they can be simply determined by fixed values as well.

Due to the random characteristics of evolutionary algorithm and metaheuristic methods, different solution may be obtained even with the same optimization algorithm. Here, the validity of the solution is checked by simulating many times with the optimization algorithm.

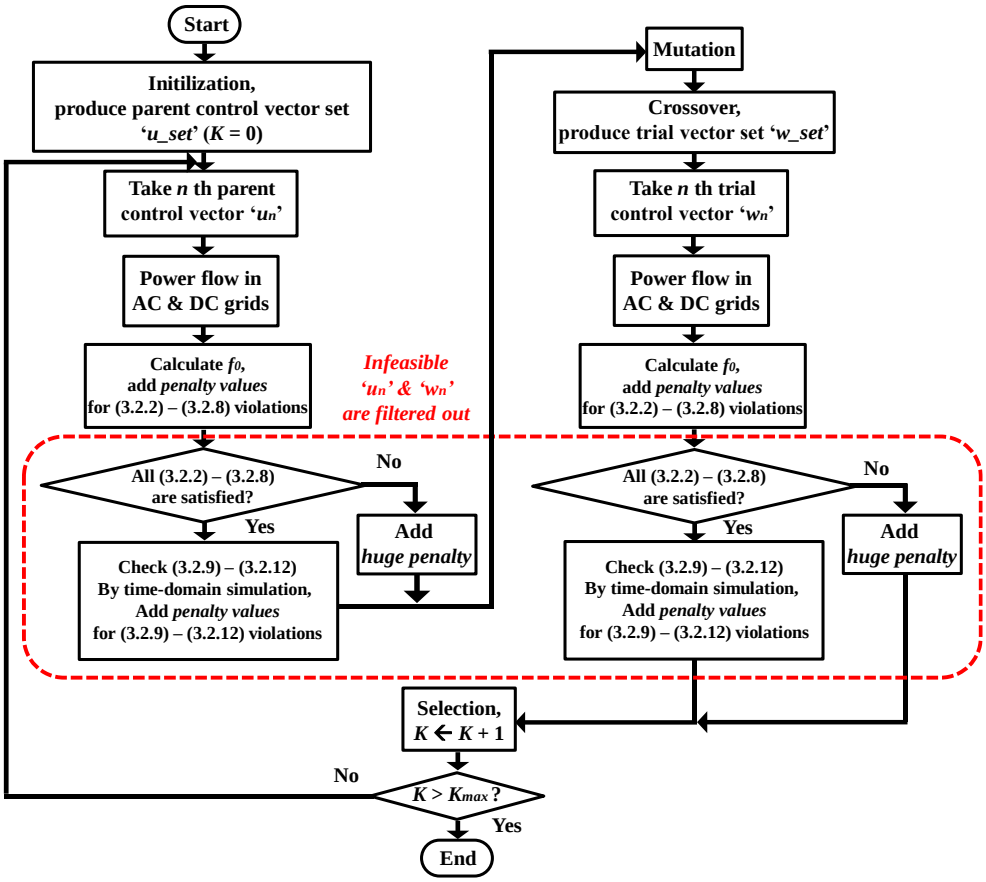

Fig. 3.2. Flowchart of each OPF analysis using differential evolution

4. Economic Benefit Analysis

4.1 Wind Power Hosting Capacities

First of all, multi-terminal topologies with different VSC locations and configurations from MTDC *a*) to MTDC *i*) systems are defined in Table 4.1 to find the system capable of installing the largest wind power plants' capacity. For instance, the notation of MTDC *a*) indicates VSC 3 of a three-terminal VSC HVDC system is installed at AC bus (21). MTDC *h*) represents the system with VSCs 3 and 4 of a four-terminal VSC HVDC system installed at AC buses (21) and (28) respectively.

Table 4.1. Multi-terminal VSC HVDC system notations

MTDC	*a*) 3−terminal, VSC 3 at (21)
	b) 3−terminal, VSC 3 at (25)
	c) 3−terminal, VSC 3 at (28)
	d) 3−terminal, VSC 3 at (31)
	e) 3−terminal, VSC 3 at (35)
	f) 4−terminal, VSC 3, 4 at (21)(25)
	g) 4−terminal, VSC 3, 4 at (25)(28)
	h) 4−terminal, VSC 3, 4 at (21)(28)
	i) 4−terminal, VSC 3, 4 at (31)(35)

The wind power hosting capacities of the system models and the total investment costs for the hosting capacities are calculated in Table 4.2. This aims at investigating the economic benefits of MTDC systems in which the maximum allowable wind power capacity of each system is introduced. In the hosting capacity analysis, power system reinforcements are considered if necessary for the installation of large-scale wind power plants. Hence, Step 1 analysis is applied for the investigation of the hosting capacities.

The notations of 'OPF' and 'SSSC-OPF' correspond to the cases of the normal OPF analysis without any stability constraints and with the consideration of small-signal stability constraint 'small-signal stability constrained-optimal power flow (SSSC-OPF)' respectively. In this chapter, the transient stability constraints are not considered. The investment costs of hybrid type DC circuit breakers at each DC transmission line are not included in the OPF and SSSC-OPF results.

Wind power suppression is not allowed except in the N-1 post-fault contingency analysis. The investigation is started in which 1GW of both wind farms are installed. If all six periods with peak wind power outputs are revealed to have the Step 1 solution, the capacities of both wind farms are increased by 1GW again. This process is repeated until no solution is found in at least one period. For example, 5+5GW of wind power hosting capacity implies that all six periods of the system model with peak wind power outputs are revealed to have the Step 1 solutions. However, the Step 1 solution is not found in at least one of the six periods when 6+6GW of wind farms are installed.

Without any MTDC reinforcements, it is revealed by the OPF analysis that 5+5GW wind farms are allowed to be installed in Base Case. In contrast, only up to 2+2GW wind farms can be installed in Base Case according to the result of the SSSC-OPF analysis. More than 3+3GW wind farm installations are prohibited to prevent unstable modes. For instance, the eigenvalues with positive real parts are observed in Section 6 when 3+3GW wind farms are installed in Base Case as can be seen in Table 4.3. In this case, these unstable eigenvalues are mainly triggered by the generators close to the wind farms. Different unstable eigenvalues can also appear depending on the capacity of wind farms, seasonal, and load conditions. The principle of this unstable phenomenon can be explained by Fig. 4.1. For the simple explanation, the ideal AC transmission system is assumed in Fig. 4.1. Since AC voltages are limited between 0.9 *p.u.* and 1.1 *p.u.* by the AC bus voltage constraints of the OPF analysis in normal operations, the phase angle differences between AC buses δ are needed to be increased to increase the amount of active power transmission. However, the system operation becomes unstable when δ exceeds 90 degrees in the ideal AC transmission system. Although the practical AC transmission systems are different from the ideal system, this principle can still be applied to explain the unstable phenomenon of AC transmission systems in cases of large-scale active power transmission. Without any adjustments of the transmission line reactance component X, the phase angle differences δ between AC buses are increased in cases of large-scale active power transmission. However, the system operation becomes unstable if δ exceeds a certain small-signal stability limit.

On the contrary, the wind power hosting capacities of the systems with one of the MTDC systems in Table 4.1 can be increased. Firstly, HVDC transmission systems do not suffer from such unstable problems explained above. In addition, the MTDC systems with the control systems are also able to contribute to the system stabilization.

The results of Step 1 analysis and the final reinforcement decisions of all MTDC systems are calculated from Table 4.4 to Table 4.12. As explained in Chapter 3, the maximum capacity result of each device is adopted as the final reinforcement decision. In most conditions, the maximum capacity results of devices are calculated in the low-load conditions; Periods 2, 4, and 6. This is due to the fact that large amounts of active power transmissions from the upper area with the wind farms towards the lower area are required mainly in these conditions. On the other hand, since the wind power output can be consumed in the local upper area in the peak-load conditions, the reinforcement capacity results of Step 1 analysis in Periods 1, 3, and 5 are relatively lower than those in Periods 2, 4, and 6.

It is noteworthy that different hosting capacities of MTDC systems in Table 4.2 are obtained. The critical factor of these different MTDC hosting capacities is revealed to be AC transmission line capacities near VSCs 3 and 4. As described in Fig. 4.2, the AC transmission lines near AC bus (25) are heavily loaded in peak-load conditions since a significant amount, approximately 17GW of active power is transmitted from G2 and G3 sides. The AC transmission lines close to AC bus (31) are also heavily loaded in low-load conditions. In these low-load conditions, the upper area local power consumptions are lower than those in the peak-load conditions. Hence, in case of peak wind power output, the amounts of the active power transmission from the upper area towards the lower area in the low-load conditions are relatively higher than those in the peak-load conditions. Therefore, when VSC 3 is installed at AC bus (25) in MTDC *b*) system, more than 7+7GW wind

farm installations are not permitted due to the lack of AC transmission line capacities near AC bus (25). For the same reason, the wind power hosting capacity of MTDC *d*) is the lowest among all MTDC systems. On the contrary, MTDC *h*) system with the four-terminal configuration is relatively free from this AC transmission line capacity issue. The sufficient AC transmission line capacities can be secured by adjusting the active power productions of the thermal power plants. For example, AC bus (28) is close to G4 and G5 whose rated capacities are relatively large in the system model. Nevertheless, the sufficient AC transmission line capacities near AC bus (28) can be secured by adjusting the active power production of G4. As a consequence, MTDC *h*) leads to the highest 9+9GW wind power hosting capacity. The installation of more than 9+9GW wind farms is prohibited by the lower limits of thermal power plant productions. Additional energy storage systems are required to install more than 9+9GW wind power plants. In other words, the VSC installations at AC buses close to the thermal power plants are recommended to reduce the thermal power plant productions and increase the amount of wind power plants installation.

Table 4.2. Wind power hosting capacities and investment costs of multi-terminal VSC HVDC systems

	Wind power hosting capacity [GW]		***Inv.Costs* [billion JPY]**	
	OPF	SSSC-OPF	OPF	SSSC-OPF
Base Case	5+5	2+2	0	0
MTDC *a*)	8+8		469	
MTDC *b*)	6+6		308	
MTDC *c*)	8+8		584	
MTDC *d*)	5+5		262	
MTDC *e*)	6+6		443	
MTDC *f*)	8+8		489	
MTDC *g*)	8+8		503	
MTDC *h*)	9+9		638	
MTDC *i*)	7+7		529	

Table 4.3. Examples of unstable eigenvalues in Base Case (3+3GW wind farms are installed in Section 6)

Eigenvalue	**High participation**
0758/sec ± *j*0.227Hz	G9, G10, G7, G8

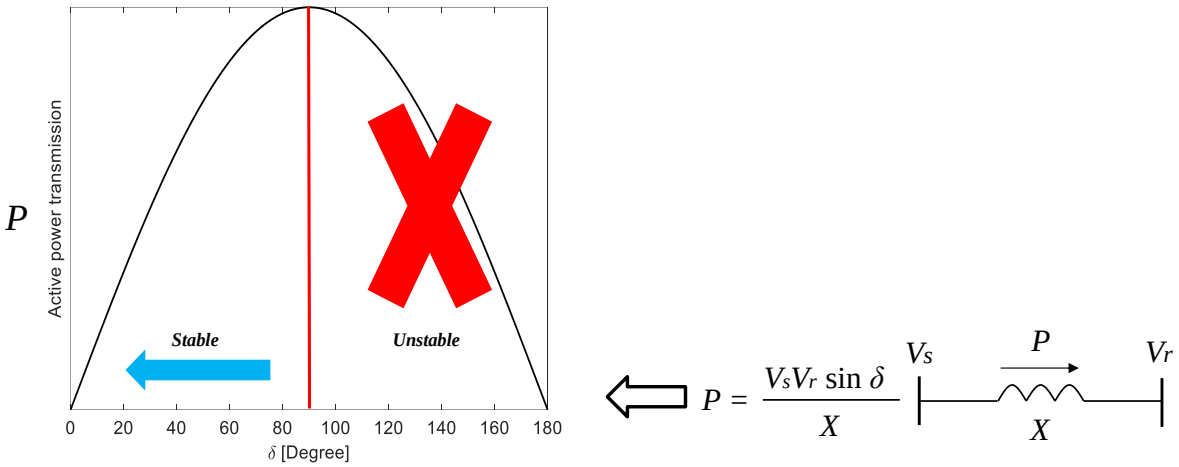

Fig. 4.1. Principle of unstable phenomenon in AC transmission system

Table 4.4. Reinforcement result of MTDC *a*) with 8+8GW wind farms by Step 1

	Reinforcement [GVA]						
	Period 1	**Period 2**	**Period 3**	**Period 4**	**Period 5**	**Period 6**	**Reinforcement decision**
VSC 1	2.8	8.5	3.3	1.6	3.1	2.2	8.5
VSC 2	3.8	1.5	4.7	7.0	3.9	6.1	7.0
VSC 3	6.6	8.1	5.5	8.0	5.9	7.7	8.1
DC line 1	2.6	7.1	2.1	1.5	2.8	2.1	7.1
DC line 2	3.6	1.2	3.8	6.8	3.4	5.9	6.8

Table 4.5. Reinforcement result of MTDC *b*) with 6+6GW wind farms by Step 1

	Reinforcement [GVA]						
	Period 1	**Period 2**	**Period 3**	**Period 4**	**Period 5**	**Period 6**	**Reinforcement decision**
VSC 1	0.80	4.0	4.0	4.3	0	4.0	4.3
VSC 2	4.4	4.7	4.8	3.5	2.1	6.5	6.5
VSC 3	2.5	4.4	3.5	4.2	1.7	5.8	5.8
DC line 1	0.80	0	0	1.6	0	0	1.6
DC line 2	1.8	4.6	2.7	2.9	1.8	6.0	6.0

Table 4.6. Reinforcement result of MTDC *c*) with 8+8GW wind farms by Step 1

	Reinforcement [GVA]						
	Period 1	**Period 2**	**Period 3**	**Period 4**	**Period 5**	**Period 6**	**Reinforcement decision**
VSC 1	7.3	10	4.8	5.2	4.3	5.9	10
VSC 2	1.0	5.1	6.4	9.6	3.3	4.7	9.6
VSC 3	6.0	9.8	7.2	9.8	5.6	8.8	9.8
DC line 1	5.3	8.7	0.50	1.3	3.2	5.2	8.7
DC line 2	1.0	0.70	5.9	8.5	2.7	4.0	8.5

Table 4.7. Reinforcement result of MTDC *d*) with 5+5GW wind farms by Step 1

	Reinforcement [GVA]						
	Period 1	**Period 2**	**Period 3**	**Period 4**	**Period 5**	**Period 6**	**Reinforcement decision**
VSC 1	3.6	5.4	4.2	3.7	2.8	3.0	5.4
VSC 2	0	2.3	3.6	1.9	1.6	2.6	3.6
VSC 3	0.80	5.0	2.8	3.6	0.70	3.2	5.0
DC line 1	0.80	4.8	2.3	1.1	0	1.3	4.8
DC line 2	0	1.5	0.70	1.8	0.80	1.8	1.8

Table 4.8. Reinforcement result of MTDC *e*) with 6+6GW wind farms by Step 1

	Reinforcement [GVA]						
	Period 1	**Period 2**	**Period 3**	**Period 4**	**Period 5**	**Period 6**	**Reinforcement decision**
VSC 1	1.1	8.0	4.2	7.2	0.90	4.2	8.0
VSC 2	1.9	0.50	3.3	1.8	3.2	6.5	6.5
VSC 3	1.7	7.5	3.0	6.4	2.1	7.2	7.5
DC line 1	0.80	7.0	1.6	6.0	0.50	1.0	7.0
DC line 2	1.0	0.50	1.3	0	1.6	6.5	6.5

Table 4.9. Reinforcement result of MTDC *f*) with 8+8GW wind farms by Step 1

	Reinforcement [GVA]						
	Period 1	**Period 2**	**Period 3**	**Period 4**	**Period 5**	**Period 6**	**Reinforcement decision**
VSC 1	6.2	5.5	6.3	3.4	5.0	9.6	9.6
VSC 2	0	4.6	2.7	5.2	2.5	1.0	5.2
VSC 3	5.8	8.3	7.3	7.8	6.0	7.8	8.3
VSC 4	0	1.8	0	0	0	1.2	1.8
DC line 1	6.1	5.0	3.9	3.2	4.4	8.2	8.2
DC line 2	0	3.7	2.2	5.0	1.8	1.0	5.0
DC line 3	0	1.9	2.0	4.8	1.6	0.30	4.8

Table 4.10. Reinforcement result of MTDC *g*) with 8+8GW wind farms by Step 1

	Reinforcement [GVA]						
	Period 1	**Period 2**	**Period 3**	**Period 4**	**Period 5**	**Period 6**	**Reinforcement decision**
VSC 1	6.0	4.3	5.9	9.7	0.70	4.6	9.7
VSC 2	3.1	5.5	3.5	0	5.4	5.4	5.5
VSC 3	2.1	5.2	3.6	6.2	0.70	4.4	6.2
VSC 4	3.7	3.0	2.3	2.1	4.7	4.3	4.7
DC line 1	3.5	3.4	3.2	8.3	0.70	4.6	8.3
DC line 2	2.6	5.1	2.5	0	5.0	4.4	5.1
DC line 3	1.3	2.0	0	1.8	0	0	2.0

Table 4.11. Reinforcement result of MTDC *h*) with 9+9GW wind farms by Step 1

	Reinforcement [GVA]						
	Period 1	**Period 2**	**Period 3**	**Period 4**	**Period 5**	**Period 6**	**Reinforcement decision**
VSC 1	2.9	7.5	4.9	8.4	7.4	3.6	8.4
VSC 2	5.5	5.2	5.0	8.0	2.6	9.2	9.2
VSC 3	5.4	5.6	9.0	5.6	5.8	2.3	9.0
VSC 4	2.4	4.7	0.60	5.2	1.8	7.7	7.7
DC line 1	2.8	5.9	4.3	5.9	6.0	1.0	6.0
DC line 2	4.8	4.6	4.1	5.3	2.0	9.2	9.2
DC line 3	2.3	0	3.3	0	0	1.3	3.3

Table 4.12. Reinforcement result of MTDC *i*) with 7+7GW wind farms by Step 1

	Reinforcement [GVA]						
	Period 1	**Period 2**	**Period 3**	**Period 4**	**Period 5**	**Period 6**	**Reinforcement decision**
VSC 1	5.6	8.8	6.2	8.8	6.1	7.2	8.8
VSC 2	1.0	0	2.5	4.9	1.6	3.6	4.9
VSC 3	2.8	5.2	4.5	5.9	3.6	5.0	5.9
VSC 4	1.6	9.2	0	6.5	0.80	7.9	9.2
DC line 1	3.5	7.6	3.7	8.0	3.5	5.2	8.0
DC line 2	1.0	0	0.90	2.2	1.0	3.1	3.1
DC line 3	0.60	8.7	0.80	2.3	0	4.8	8.7

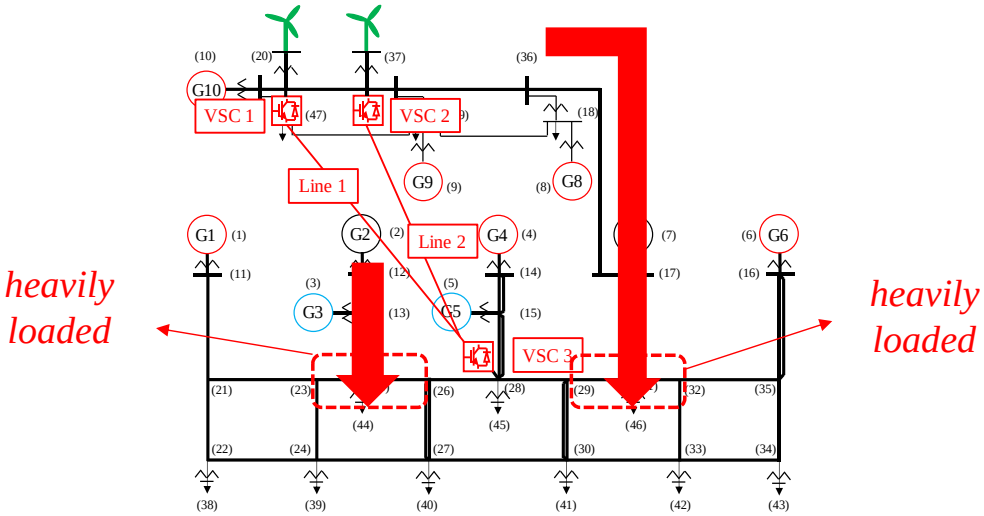

Fig. 4.2. Critical factor of MTDC system wind power hosting capacity : AC transmission line capacities

The hosting capacities and investment costs of New AC systems are calculated to prove the limitations of conventional AC transmission systems. Regarding the results of New AC systems, the post-fault feasibility analysis for the N-1 criterion is neglected to focus only on the influence of the small-signal stability constraint.

The first limitation can be inferred by comparing the wind power hosting capacities and investment costs of the OPF and SSSC-OPF results. Unlike the hosting capacities of the models with a MTDC system, it can be seen that the wind power hosting capacities of New AC systems are reduced when the small-signal stability constraints are considered. This is due to the unstable phenomenon described in Fig. 4.1. In the SSSC-OPF analysis, the phase angle differences between AC buses are also limited by the small-signal stability constraint, which limits the amount of active power transmission in AC grids.

The second limitation is the expensive investment costs of New AC systems compared to the costs of the MTDC systems of the SSSC-OPF analysis. In particular, more AC transmission lines are necessary even for the reduced hosting capacity of 4+4GW wind farms in the SSSC-OPF analysis compared to the results in the OPF analysis. The Step 1 reinforcement results of New AC systems are listed from Table 4.14 to Table 4.17. In general, the final reinforcement results of *AC groups 1a*, *1b*, and *2b* are decided by the results in the low-load conditions; Periods 2, 4, and 6. In these periods, since the total load consumption in the upper area is lower than that in the peak-load conditions, the amounts of active power transmission from the upper area towards the lower area are larger than those in the peak-load conditions. Considering the phase angle differences constraints between AC buses by the small-signal stability constraint, significant amounts of AC transmission line capacities are installed to reduce the reactance components of the lines X, consequently, to achieve the large-scale active power transmission.

Table 4.13. Wind power hosting capacities and investment costs of New AC systems

	Wind power hosting capacity [GW]		***Inv.Costs* [billion JPY]**	
	OPF	SSSC-OPF	OPF	SSSC-OPF
New AC system 1	5+5	4+4	455	744
New AC system 2	5+5	4+4	544	808

Table 4.14. Reinforcement result of New AC system 1 with 5+5GW wind farms by OPF

	Reinforcement [GW]						
	Period 1	**Period 2**	**Period 3**	**Period 4**	**Period 5**	**Period 6**	**Reinforcement decision**
AC group 1a	0.20	11	3.3	0	0	4.8	11
AC group 2a	0	0	0	0	0	0	0
AC group 3a	0	0	0	0	0	0	0
AC group 4a	0	0.8	0	0.4	0	0.6	0.80

Table 4.15. Reinforcement result of New AC system 2 with 5+5GW wind farms by OPF

	Reinforcement [GW]						
	Period 1	**Period 2**	**Period 3**	**Period 4**	**Period 5**	**Period 6**	**Reinforcement decision**
AC group 1b	6.7	6.7	6.7	6.7	6.7	6.7	6.7
AC group 2b	6.7	6.7	6.7	6.7	6.7	6.7	6.7
AC group 3b	0	0	7	0	0	0	7

Table 4.16. Reinforcement result of New AC system 1 with 4+4GW wind farms by SSSC-OPF

	Reinforcement [GW]						
	Period 1	**Period 2**	**Period 3**	**Period 4**	**Period 5**	**Period 6**	**Reinforcement decision**
AC group 1a	1.5	19	0.30	12	0	14	19
AC group 2a	0	0	0	0	0	0	0
AC group 3a	0	0	0	0	0	0	0
AC group 4a	0	0	0	0	0	0.80	0.80

Table 4.17. Reinforcement result of New AC system 2 with 4+4GW wind farms by SSSC-OPF

	Reinforcement [GW]						
	Period 1	**Period 2**	**Period 3**	**Period 4**	**Period 5**	**Period 6**	**Reinforcement decision**
AC group 1b	6.7	7.9	6.7	7.8	6.7	9.9	9.9
AC group 2b	6.7	11	6.7	6.7	6.7	6.7	11
AC group 3b	0	0	0.90	0	1.2	0	1.2

4.2 Definition of Economic Benefit Index

The analysis model of economic benefits in this dissertation is based on the scenario that considering the utilization of large-scale wind power plants, the existing transmission system operator is in charge of reinforcing the transmission system if necessary. The transmission system operator and the wind power plants operator are different. In this context, the method to define the economic benefits of the transmission system reinforcement, operation and the installation of the wind power plants is investigated.

As the results of the Step 1 HVDC reinforcement, the Step 2 operations, and the additional wind farms installation, the fuel cost reduction $F.C_{reduc}$ and the HVDC wheeling charge $HVDC_{wh}$ benefits are produced. These economic benefits are taken into consideration in the cash inflow CF of the HVDC system. The subscript t in the following definitions represents the year 't'.

The annual fuel cost of the system with MTDC $F.C._{MTDC,t}$ can be reduced compared to the annual fuel cost of Base Case $F.C._{Base\ Case,t}$ in (4.2.2). The proposed hierarchical MTDC reinforcement and operation contributes to $F.C._{reduc,t}$. In addition, $F.C._{reduc,t}$ is also affected by the reduced thermal power plant productions $P_{reduc,Th,t}$.

It should be noted that the aim is to evaluate the economic benefits obtained by the proposed hierarchical analysis using a MTDC system. However, not only the benefits of the hierarchical analysis, but the installation of additional wind farms also contributes to $F.C_{reduc,t}$. In order to focus only on the benefits of the hierarchical method, the contribution of additional wind farms is needed to be excluded.

Here, the fuel cost reduction $F.C_{reduc}$ benefit produced by additional wind farms is defined as $\mathrm{Pr}_{Th} \times P_{reduc,Th}$. $P_{reduc,Th}$ and Pr_{Th} correspond to the active power production by additional wind farms installation and the unit fuel cost respectively. $P_{reduc,Th}$ is identical to $P_{WF,MTDC} - P_{WF,BaseCase}$ in (4.2.3). Consequently, the cash inflow produced by the hierarchical MTDC reinforcement and operation is defined as $F.C._{reduc} - (Pr_{Th} \times P_{reduc,Th})$ in (4.2.1) excluding the contribution of additional wind farms installation.

As the definition of Pr_{Th}, the marginal costs $f_{m,G}$ of all thermal power plants in (4.2.5) are utilized. Since the marginal costs represent the relationship between the active power productions of thermal power plants and the corresponding fuel costs, the meaning of the unit fuel costs Pr_{Th} can be evaluated properly. Depending on Step 2 results, all 18 sections can have different Pr_{Th} unit fuel costs. When the active power production of a thermal power plant in Base Case is its minimum production limit $P_{G,min}$, the marginal cost of the generator is defined as zero. This is due to the fact that the active power production of the generator in Base Case cannot be reduced even with additional wind farms installed. Finally, the weighted average of the thermal power plants $f_{m,G}$ weighted by their respective active power productions $P_{G,MTDC}$ is defined as the unit fuel cost of the whole system model Pr_{Th} in (4.2.4).

Not only the fuel cost reduction benefit explained above, the wheeling charge benefit $HVDC_{wh}$ is also produced by the hierarchical MTDC reinforcement and operation. $HVDC_{wh,annual}$ in (3.1.4) is calculated by the total transmitted energy using a MTDC system multiplied by the unit MTDC wheeling charge.

Net present value (NPV) is calculated as (4.2.6). $Inv.Costs_{MTDC}$ is the total investment costs of a MTDC system determined in Step 1. Profitability index (PI) analysis in (4.2.7) is calculated to evaluate the cost-benefit efficiency of an investment decision $Inv.Costs_{MTDC}$.

$$CF_t = F.C._{reduc,t} - (\mathrm{Pr}_{Th} \times P_{reduc,Th,t}) + HVDC_{wh,annual,t} \tag{4.2.1}$$

$$F.C._{reduc,t} = F.C._{Base\ Case,WF,t} - F.C._{MTDC,WF,t} \tag{4.2.2}$$

$$P_{reduc,Th,t} = P_{MTDC,WF,t} - P_{Base\ Case,WF,t} \tag{4.2.3}$$

$$\mathrm{Pr}_{Th} = \frac{\sum_{G \in N_G} P_{G,MTDC} f_{m,G}}{\sum_{G \in N_G} P_{G,MTDC}} \tag{4.2.4}$$

$$f_{m,G} = B_G + 2A_G P_{G,MTDC} \tag{4.2.5}$$

$$NPV = \left[\sum_{t=1}^{LT} \frac{CF_t}{(1+ir)^t} \right] - Inv.Costs_{MTDC} \tag{4.2.6}$$

$$PI = 1 + (NPV / Inv.Costs_{MTDC}) \tag{4.2.7}$$

Before the economic analysis, the unit wheeling charges Wh_{unit} of MTDC systems are needed to be determined to calculate the wheeling charge profits of MTDC systems. Many different scenarios can be applied depending on the environments, regulations, and policies regarding power system operations. Here, the economic benefit analysis is based on the scenario that the power system operator can reinforce the system with a MTDC system for the installation of additional wind farms. In order to for the investment costs of the MTDC system to be paid back within its life-time, the wheeling charge is imposed to customers using the MTDC system. According to this scenario, Wh_{unit} can be determined by (4.2.8), (4.2.10), and (4.2.11). When the annual interest rate of cash flow is considered, Wh_{unit} can be defined based on (4.2.9), (4.2.10), and (4.2.12).

$$\frac{Inv.Cost_{MTDC}}{LT} = HVDC_{wh,annual} \tag{4.2.8}$$

$$Inv.Costs_{MTDC} \times CRF = HVDC_{wh,annual} \tag{4.2.9}$$

$$HVDC_{wh,annual} = Wh_{unit} \times E_{HVDC,annual} \tag{4.2.10}$$

$$Wh_{unit} = \frac{Inv.Cost_{MTDC}}{LT \times E_{HVDC,annual}} \tag{4.2.11}$$

$$Wh_{unit} = \frac{Inv.Cost_{MTDC} \times CRF}{E_{HVDC,annual}} \tag{4.2.12}$$

$E_{HVDC,annual}$ Total annual transmitted energy by a VSC HVDC system [kWh]

In the previous wind power hosting capacity analysis, Base Case system is revealed to be capable of installing 2+2GW wind farms in the SSSC-OPF analysis. A MTDC system reinforcement is required for the installation of additional wind farms.

In order to decide Wh_{unit}, the conventional MTDC reinforcement and operation are considered as the standard case. In Base Case system, 1GVA MTDC system is installed to integrate additional 1+1GW wind farms in the conventional MTDC reinforcement concept. Similarly, *x*GVA MTDC system reinforcement is taken into account to install additional $x + x$ GW wind farms in the conventional approach as plotted in Fig. 4.3. As for the conventional MTDC operation, the wind power output is firstly consumed by the local upper area loads. The rest of wind power production is transmitted towards the other lower area. Accordingly, the MTDC transmission system is hardly used when the wind power production is not high enough. The conventional MTDC operation concept is described in Fig. 4.4.

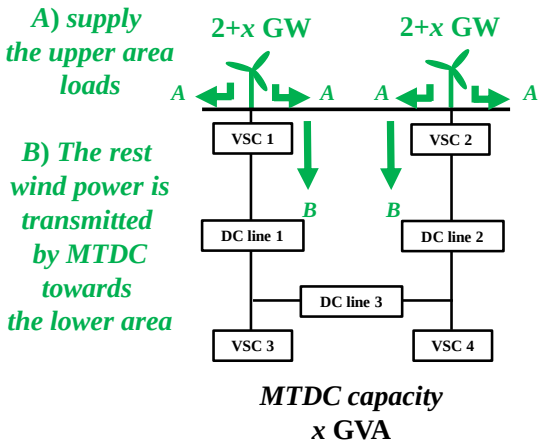

Fig. 4.3. Conventional MTDC reinforcement concept for additional x+xGW wind farms

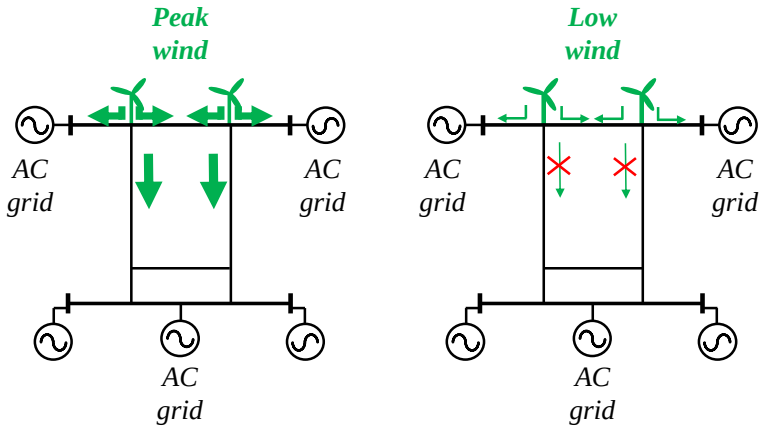

Fig. 4.4. Conventional MTDC operation concept in cases of peak and low wind outputs

The unit wheeling charges Wh_{unit} of MTDC *h*) system with different capacities of wind farms are calculated in Table 4.18. For example, the result with 9+9GW wind farms mean that 2.37 JPY/kWh of Wh_{unit} is required for the investment cost of 7GVA MTDC *h*) system to be paid back by the conventional MTDC operation in Fig. 4.4. When 1GVA MTDC *h*) system is installed for the additional 1+1GW wind farms, the transmitted energy via the MTDC system is very low. Thus, impractically high Wh_{unit} is necessary.

It should be reminded that one of the objectives of this dissertation is the utilization of large-scale wind power plants. Therefore, the result of Wh_{unit} with the largest capacity of wind farms is desirable to be quoted. For the simplicity, Wh_{unit} is determined to be 2 JPY / kWh in this dissertation.

Table 4.18. Wh_{unit} based on conventional MTDC *h*) system operations

Total wind farm capacity [GW]	3+3	5+5	7+7	9+9
MTDC capacity [GVA]	1	3	5	7
Wh_{unit} **[JPY / kWh]**	22.9	4.98	3.18	2.37

For starters, the hourly cash flow results of all 18 sections are plotted in Fig. 4.6. $Pr_{Th} \times P_{reduc,Th}$ is also notated in Fig. 4.6 together, but actually not included in the cash inflow of MTDC systems. $HVDC_{wh,con}$ corresponds to the basic HVDC wheeling charge profit which can be obtained by the conventional MTDC operation in Fig. 4.4. Whereas $HVDC_{wh,pro}$ indicates the additional HVDC wheeling charge benefits produced by the proposed hierarchical OPF analysis. The additional economic benefits produced by the proposed hierarchical OPF method correspond to $F.C._{reduc} - (Pr_{Th} \times P_{reduc,Th})$ and $HVDC_{wh,pro}$ terms.

By applying the proposed hierarchical OPF method, the installed MTDC system can be utilized more effectively as described in Fig. 4.5. When the wind power output is high, the wind power plant outputs can be transmitted using the MTDC system if necessary. The amounts of active power transmissions via AC transmission systems and the MTDC system are determined to minimize the objective function, the total fuel cost of the system models. On top of that, the MTDC system can still be utilized in case of the low wind power outputs. In Fig. 4.5, the MTDC system is also used for the active power transmission among AC grids to minimize the total fuel cost. As a result, higher average capacity factor of the MTDC system can be obtained compared to the conventional operation in Fig. 4.4. As a consequence, additional economic benefits $HVDC_{wh,pro}$ can also be produced.

To be more specific, the operation results in Sections 1 and 9 are selected to be explained as the representative examples. In Section 1 with low wind power outputs in Fig. 4.7, the produced wind power is consumed in the local upper area. As a result, there is no wind power transmission from the upper area towards the lower area and thus, the HVDC transmission system in the left-hand side of Fig. 4.7 is not used at all in case of the conventional operation. On the other hand, the MTDC system in the right-hand side of Fig. 4.7 can still be utilized for the minimization of the total fuel cost as notated by the red arrows in Fig. 4.7. In the system model, the active power is

transmitted from G4 side towards other generator sides due to one of the cheapest fuel cost coefficients of G4. Consequently, two additional benefits; the fuel cost reduction effect by the proposed method and higher capacity factor of the MTDC system can be produced. These benefits are represented as $F.C._{reduc} - (\mathrm{Pr}_{Th} \times P_{reduc,Th})$ and $HVDC_{wh,pro}$ profits in Fig. 4.6.

In Section 9 with peak wind outputs in Fig. 4.8, 18GW of wind power is produced and the total active power consumption in the upper area is 14.25GW. Hence, the produced wind power is consumed by the upper area loads preferentially and the rest of wind power, 3.75GW is transmitted towards the lower area by the conventional operation. In such case, the multi-terminal configuration is not essential and two point-to-point VSC HVDC transmission systems may also be capable of this conventional operation. On the contrary, the wind power outputs can be transmitted more effectively to minimize the total fuel cost by the proposed operation method as described in the right-hand side of Fig. 4.8. The increased capacity factor of the MTDC system can also be checked by the difference of the MTDC active power transmission between the conventional and proposed operations; (7.43 + 1.25) – 3.75GW. As a result, additional economic benefits indicated as $F.C._{reduc} - (\mathrm{Pr}_{Th} \times P_{reduc,Th})$ and $HVDC_{wh,pro}$ terms in Fig. 4.6 are obtained by the proposed method.

The highest $F.C._{reduc} - (\mathrm{Pr}_{Th} \times P_{reduc,Th})$ cash inflow is produced in Section 9. In Sections 7, 8, and 9, the power system models are in the most heavily-loaded conditions. In such conditions, G8 and G9 with the most expensive fuel cost coefficients are also required to produce active power to satisfy the supply and demand balance. When the developed hierarchical OPF method is applied in these conditions, the active power productions with the most expensive fuel cost coefficients can be reduced, which leads to substantial fuel cost reduction effects. Considering both wind power transmission and AC grid power transmission, the highest $F.C._{reduc} - (\mathrm{Pr}_{Th} \times P_{reduc,Th})$ profit can be obtained in the most heavily-loaded patterns with the peak wind production.

It is worth emphasizing the generality of the proposed hierarchical OPF method. The same principle can be applied to the analysis of other power systems for the transmission of RES using a MTDC system. By adopting different objective functions in the hierarchical OPF analysis, a MTDC system can be utilized effectively for various purposes.

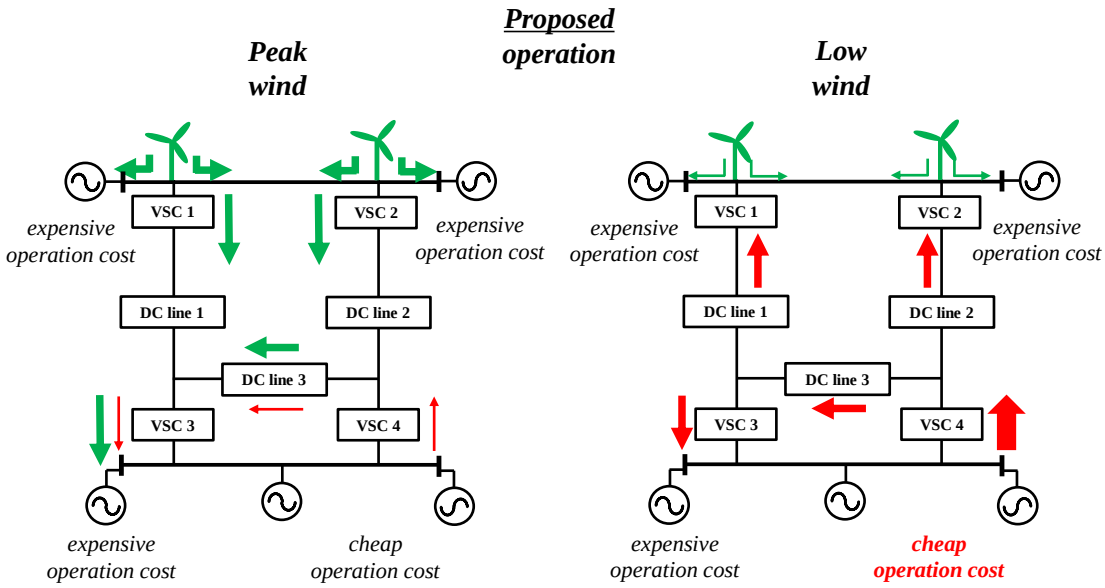

Fig. 4.5. MTDC operation by the proposed hierarchical OPF method

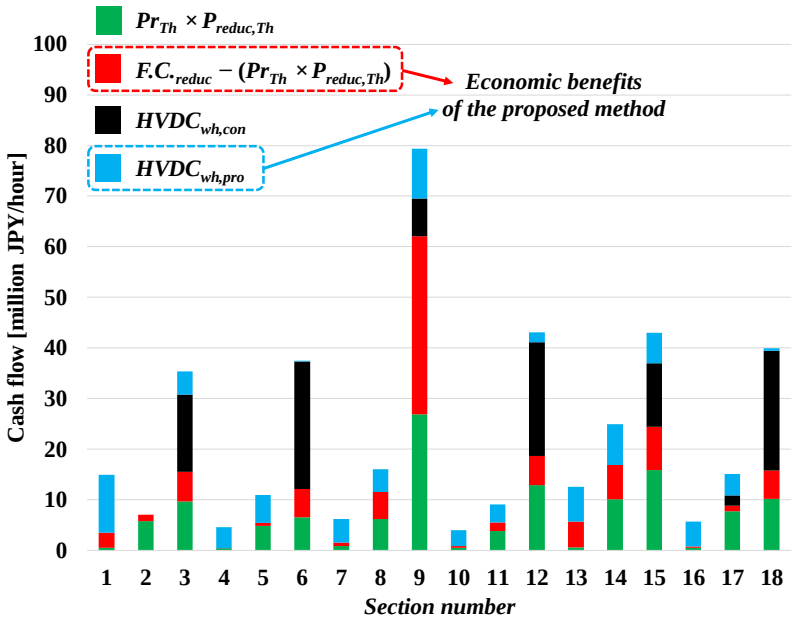

Fig. 4.6. Hourly cash flow results of MTDC *h*) with 9+9GW wind farms in each section by SSSC-OPF ($\sigma_{max,0} = 0$)

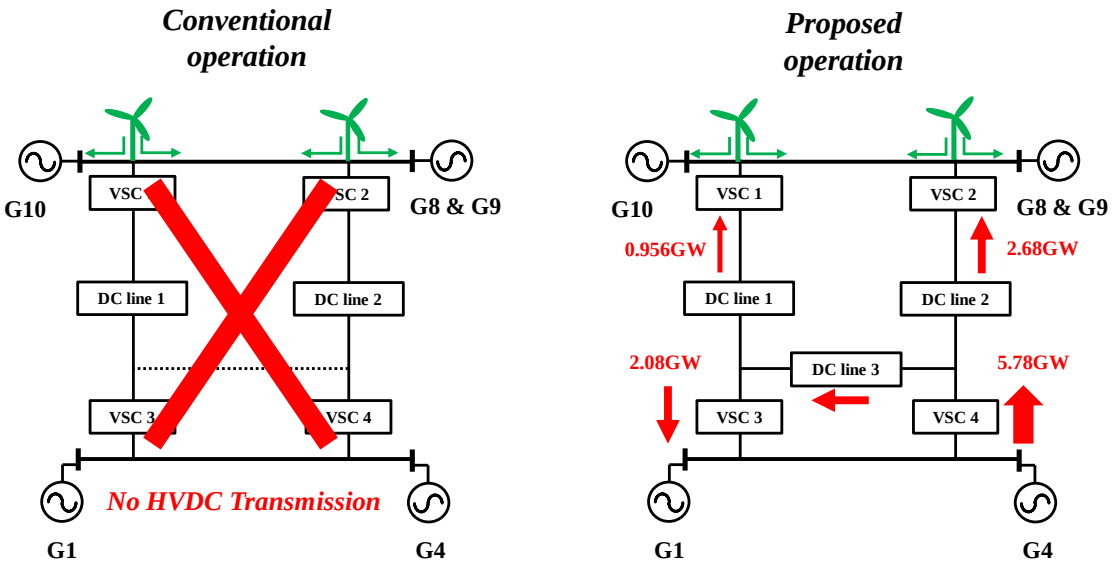

Fig. 4.7. Comparison of HVDC operations between conventional and proposed methods in Section 1

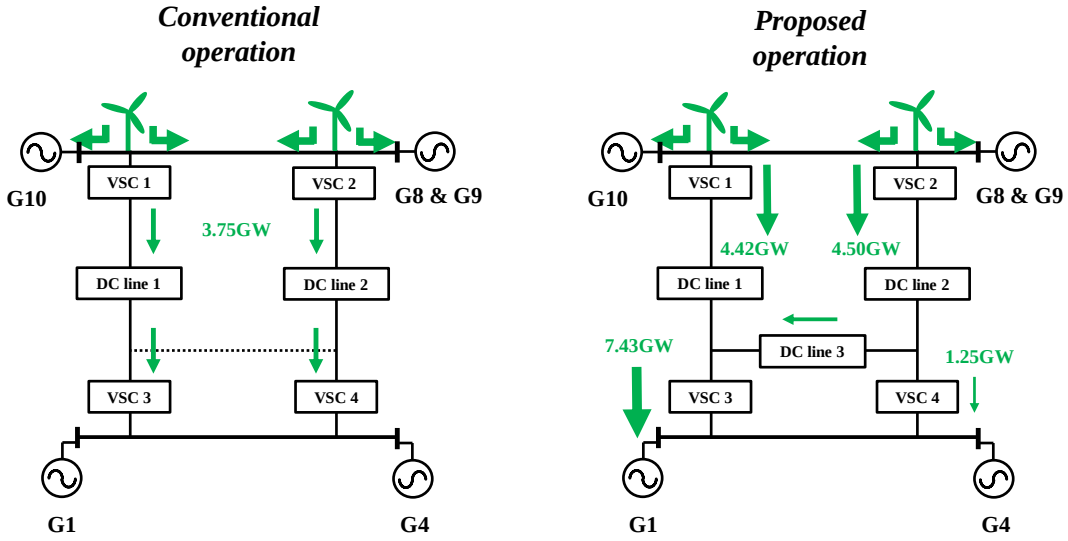

Fig. 4.8. Comparison of HVDC operations between conventional and proposed methods in Section 9

The results of NPV and PI indices by OPF and SSSC-OPF analyses are listed in Table 4.19 and Table 4.20 respectively. The highest NPV and PI are obtained by MTDC *h*) system which is capable of integrating the largest wind power hosting capacity, 9+9GW. It can be seen that despite the high investment costs of four-terminal MTDC systems, the PI result of MTDC *h*) is high. Compared to the three-terminal configurations, more effective active power transmission can be achieved by the four-terminal MTDC system, which yields high wheeling charge income.

The annual fuel cost results of Base Case with 5+5GW in OPF analysis and 2+2GW SSSC-OPF analysis are 492 billion JPY and 524 billion JPY respectively. In contrast, the results of MTDC systems in Step 1 and Step 2 are not influenced by the consideration of the small-signal stability constraint, $\sigma_{max,0} = 0$. In other words, the system models reinforced with a MTDC system is stable from the small-signal stability viewpoint. As a consequence, higher NPV and PI results of all MTDC systems are calculated in the SSSC-OPF analysis due to the increased $F.C._{reduc} - (\mathrm{Pr}_{Th} \times P_{reduc,Th})$ profits compared to the results by the OPF analysis.

Table 4.19. Economic benefit results by OPF

	***Hosting capacity* [*GW*]**	***Investment cost* [*billion JPY*]**	***NPV* [*billion JPY*]**	***PI***
Base Case	5+5			
MTDC *a*)	8+8	469	595	2.27
MTDC *b*)	6+6	308	177	1.57
MTDC *c*)	8+8	584	489	1.84
MTDC *d*)	5+5			
MTDC *e*)	6+6	443	440	1.99
MTDC *f*)	8+8	489	973	2.99
MTDC *g*)	8+8	503	513	2.02
MTDC *h*)	9+9	638	1330	3.09
MTDC *i*)	7+7	529	852	2.61

Table 4.20. Economic benefit results by SSSC-OPF ($\sigma_{max,0} = 0$)

	***Hosting capacity* [*GW*]**	***Investment cost* [*billion JPY*]**	***NPV* [*billion JPY*]**	***PI***
Base Case	2+2			
MTDC *a*)	8+8	469	906	2.93
MTDC *b*)	6+6	308	432	2.40
MTDC *c*)	8+8	584	784	2.34
MTDC *d*)	5+5	262	554	3.08
MTDC *e*)	6+6	443	702	2.58
MTDC *f*)	8+8	489	1280	3.63
MTDC *g*)	8+8	503	818	2.63
MTDC *h*)	9+9	638	1670	3.62
MTDC *i*)	7+7	529	1140	3.15

4.3 Sensitivity Analyses of Wind Power Capacity and Small-Signal Stability Constraints

4.3.1 Sensitivity Analysis of Wind Farm Capacity

Among the MTDC systems, MTDC *h*) system capable of the largest 9+9GW wind farm installation is selected for the sensitivity analysis as the representative examples. In order to focus only on the influence of wind farm capacity, the least severe small-signal stability constraint is considered. The damping ratio constraint is not considered and $\sigma_{max,0}$ is zero in the SSSC-OPF analysis here.

The results of Step 1 analysis and the reinforcement decisions with different wind farm capacities are calculated from Table 4.21 to Table 4.23. The results with all DC line capacities being zero indicate VSC converters are operated as STATCOM modes producing only reactive power outputs.

The annual cash inflow results of MTDC *h*) system with different wind farm capacities are plotted in Fig. 4.9. It can be seen in Fig. 4.9 that MTDC *h*) system with the largest 9+9GW wind farms installation produces the highest annual cash flow.

The investment costs, NPV, and PI results of MTDC *h*) system with different wind farm capacities are calculated in Table 4.24. As the wind farm capacity increases, the required investment cost of MTDC *h*) system also increases. As for the NPV results, it can be seen that higher NPV results are observed when the wind farm capacity increases. Regarding the PI results of the MTDC systems, it is noteworthy that the optimal capacity of the wind farms from the cost-efficiency viewpoint exists. The highest PI value is calculated when 5+5GW wind farms are installed. In other words, a power system operator should find the corresponding capacity of wind power plants instead of installing as much wind power plants as possible to obtain the maximum cost-efficiency.

Table 4.21. Reinforcement result of MTDC *h*) with 3+3GW wind farms by Step 1

	Reinforcement [GVA]						
	Period 1	**Period 2**	**Period 3**	**Period 4**	**Period 5**	**Period 6**	**Reinforcement decision**
VSC 1	0.50	2.0	1.7	1.6	1.5	1.6	2.0
VSC 2	1.3	0.50	1.7	1.6	0.70	0.70	1.7
VSC 3	0.80	1.2	2.0	1.7	1.5	0.70	2.0
VSC 4	0.20	0	0.70	0	1.6	0	1.6
DC line 1	0	1.3	0.80	0.60	0	0.60	1.3
DC line 2	0	0	0.80	0.40	0.60	0.30	0.80
DC line 3	0	0	0.60	0.30	0	0.20	0.60

Table 4.22. Reinforcement result of MTDC *h*) with 5+5GW wind farms by Step 1

	Reinforcement [GVA]						
	Period 1	**Period 2**	**Period 3**	**Period 4**	**Period 5**	**Period 6**	**Reinforcement decision**
VSC 1	4.3	3.6	4.1	2.0	2.0	2.4	4.3
VSC 2	3.9	2.4	3.6	1.8	1.9	0.90	3.9
VSC 3	3.4	2.5	2.1	4.9	6.6	3.2	6.6
VSC 4	0.60	0.80	0.80	0	3.0	0.30	3.0
DC line 1	2.4	0.80	2.2	2.0	1.7	2.3	2.4
DC line 2	1.8	2.2	0.80	1.7	1.7	0.90	2.2
DC line 3	1.1	1.7	0	1.6	4.5	1.0	4.5

Table 4.23. Reinforcement result of MTDC *h*) with 7+7GW wind farms by Step 1

	Reinforcement [GVA]						
	Period 1	**Period 2**	**Period 3**	**Period 4**	**Period 5**	**Period 6**	**Reinforcement decision**
VSC 1	6.1	0	3.0	6.7	2.2	2.3	6.7
VSC 2	2.4	7.4	5.4	2.5	3.0	7.6	7.6
VSC 3	3.9	2.5	5.1	4.4	6.3	7.2	7.2
VSC 4	1.1	4.5	1.5	1.8	0	2.2	4.5
DC line 1	3.5	0	2.7	4.5	2.2	1.9	4.5
DC line 2	1.7	6.9	3.3	1.9	1.9	5.8	6.9
DC line 3	0.50	2.2	1.9	0	1.8	3.4	3.4

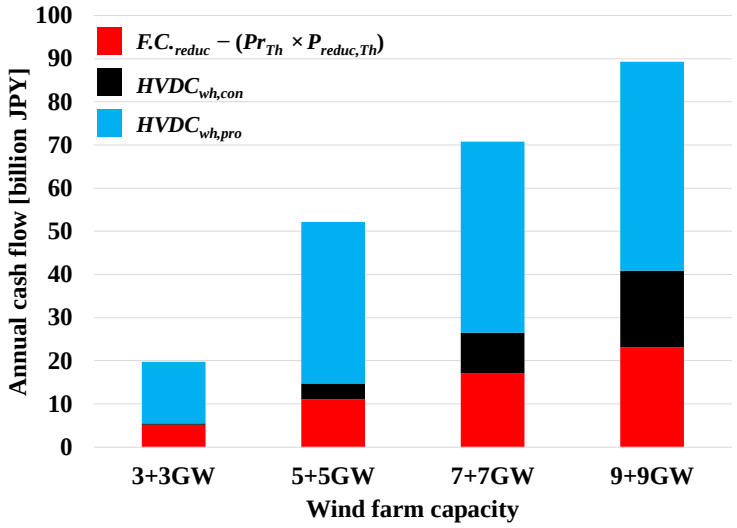

Fig. 4.9. Annual cash flow results of MTDC *h*) with different wind farm capacities

Table 4.24. Economic benefits of MTDC *h*) with different wind farm capacities

Wind farm capacity	***Inv.Cost*$_{MTDC}$ [billion JPY]**	**NPV [billion JPY]**	**Profitability Index**
3+3GW	124	386	4.11
5+5GW	303	1040	4.44
7+7GW	484	1340	3.78
9+9GW	638	1670	3.62

4.3.2. Sensitivity Analysis of Small-Signal Stability Constraints

Sensitivity analysis of the small-signal stability constraints is carried out for MTDC *h*) system which is capable of introducing the largest 9+9GW wind farms. Basically, the case with the small-signal stability constraint $\sigma_{max,0} = 0$ is considered in the SSSC-OPF analysis.

First of all, the annual fuel cost results of Base Case are calculated in Table 4.25. In the OPF analysis, the annual fuel cost of the system with 5+5GW wind farms is 492 billion JPY. However, this result is not allowed in the SSSC-OPF analysis due to unstable operations. Only up to 2+2GW wind farms can be installed in the SSSC-OPF analysis and as a consequence, the annual fuel cost of the system is 524 billion JPY.

On the other hand, the same annual fuel cost is obtained by the system with MTDC *h*) system and 9+9GW wind farms in both OPF and SSSC-OPF analyses. These cost results indicate that considering the system stabilization effect, the system model with MTDC *h*) system is more stable than Base Case system even with additional 7+7GW wind farms from the small-signal stability viewpoint. This system stabilization effect is measured as the economic benefits of MTDC *h*) system; increased $F.C._{reduc} - (\mathrm{Pr}_{Th} \times P_{reduc,Th})$ economic benefits in Fig. 4.10. As a result, the NPV and PI results of MTDC *h*) system in the SSSC-OPF analysis are also higher than those values in the OPF analysis as can be seen Table 4.26.

Table 4.25. Annual fuel cost comparison of systems by OPF and SSSC-OPF

System	Base Case, WF_{5+5GW}, OPF	Base Case, WF_{2+2GW}, SSSC-OPF	MTDC *h*), WF_{9+9GW}, OPF	MTDC *h*), WF_{9+9GW}, SSSC-OPF
Annual fuel cost [billion JPY]	492	524	457	457

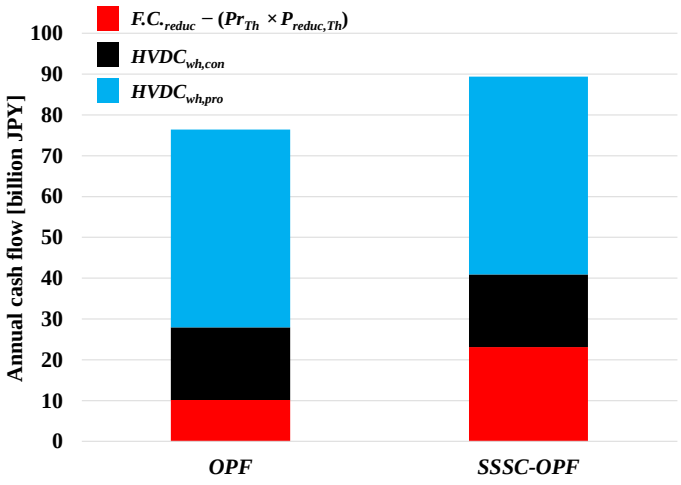

Fig. 4.10. Annual cash flow results of MTDC *h*) with 9+9GW wind farms by OPF and SSSC-OPF

Table 4.26. Economic benefits comparison of MTDC *h*) with 9+9GW wind farms by OPF and SSSC-OPF

	***Inv. Cost*$_{MTDC}$ [billion JPY]**	**NPV [billion JPY]**	**Profitability Index**
OPF	638	1330	3.09
SSSC-OPF	638	1670	3.62

In realistic power system operations, the damping ratios of a system operation are also taken into consideration to guarantee fast damping characteristics of the operations. In this dissertation, two damping ratio constraints, SSSC-OPF with ξ_{min} = 5% and ξ_{min} = 6% are surveyed. In case of ξ_{min} = 7%, the solutions in all Base Case system operations do not exist.

In Base Case system, 2+2GW wind farms can be installed for both ξ_{min} = 5% and ξ_{min} = 6% damping constraints. The installation of 9+9GW wind farms are allowed with MTDC *h*) system for both ξ_{min} = 5% and ξ_{min} = 6% scenarios.

Sections 3 and 16 are selected as the representative cases to explain the underlying principle of the sensitivity analysis. In Fig. 4.11, the eigenvalues of Base Case by the SSSC-OPF, ξ_{min} = 5% analysis with 2+2GW wind farms in Section 3 are drawn. Three eigenvalue pairs in Table 4.27 are revealed to have the damping ratios lower than 6%. These eigenvalues are affected when the constraint of ξ_{min} = 6% is considered in the SSSC-OPF analysis. The participation factor results of generators indicate that all three eigenvalue pairs are influenced by G6 in common. Therefore, the most effective way to improve the damping ratios of these eigenvalue pairs is adjusting the active power production of G6 rather than other generators in the SSSC-OPF, ξ_{min} = 6% analysis. This can also be checked in Table 4.28 where the active power productions of the thermal power plants are calculated. The production of G6 in the SSSC-OPF, ξ_{min} = 6% analysis is reduced by 30% compared to the case with ξ_{min} = 5% constraint. The G1 and G4 productions are increased to satisfy the active power supply and balance. Since the production of G6 with one of the cheapest fuel cost coefficients is reduced and instead, that of G1 is increased, the hourly fuel cost of the SSSC-OPF, ξ_{min} = 6% analysis in Section 3 is more expensive than the cost of the SSSC-OPF, ξ_{min} = 5% analysis by 3.18 million JPY / hour.

The results in Section 16 can also be interpreted similarly. The eigenvalues obtained by the SSSC-OPF, ξ_{min} = 5% analysis in Fig. 4.12 show that three eigenvalue pairs are influenced by ξ_{min} = 6% damping constraint. By calculating the participation factors of these eigenvalues, it is revealed that four generators; G2, G4, G6, and G7 give high participations on these eigenvalues. Considering that G2 and G7 are nuclear power plant models whose productions are fixed, the productions of G4 and G6 are needed to be adjusted to improve the damping ratios of the oscillation modes. In fact, the productions of G4 and G6 are in their respective maximum values. These productions are reduced and instead, those of G1 and G10 with the next cheapest fuel cost coefficients are increased to satisfy the active power supply and demand balance. As a result, the hourly fuel cost of the SSSC-OPF, ξ_{min} = 6% analysis is higher by 14.3 million JPY / hour than the cost in ξ_{min} = 5% analysis in Section 16.

The comparisons of the fuel costs in other sections can also be explained with this basic principle. To sum up, compared to the annual fuel cost of Base Case system with 2+2GW wind

farms in the SSSC-OPF, ξ_{min} = 5% analysis, the cost is increased by 44 billion JPY in the SSSC-OPF, ξ_{min} = 6% analysis as can be seen in Table 4.31.

In contrast, the SSSC-OPF solutions of the system model with MTDC *h*) system and 9+9GW wind farms are not changed by the considerations of both ξ_{min} = 5% and ξ_{min} = 6% damping constraints. Hence, it can be inferred that compared to Base Case, the system reinforced with MTDC *h*) is stable even with additional 7+7GW wind farms from the small-signal stability viewpoint. As a result, Fig. 4.13 indicates the fuel cost reduction benefit by the proposed method $F.C._{reduc} - (\mathrm{Pr}_{Th} \times P_{reduc,Th})$ becomes higher as more strict small-signal stability constraints are considered in the SSSC-OPF analysis. The NPV and PI results of MTDC *h*) system in the SSSC-OPF, ξ_{min} = 6% in Table 4.32 are also the highest among the economic benefits calculated by all small-signal stability constraint scenarios.

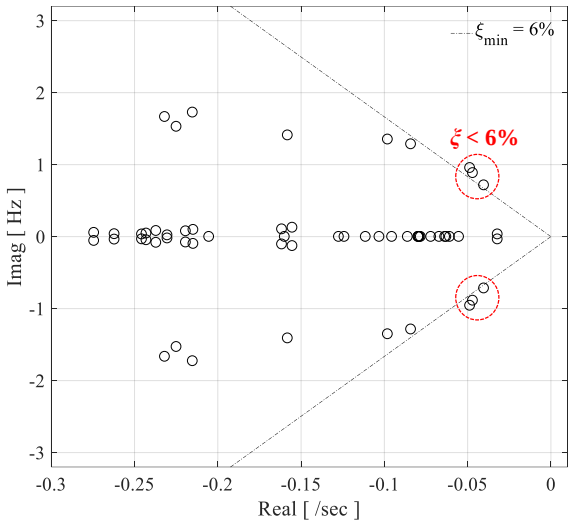

Fig. 4.11. Eigenvalues of Base Case with 2+2GW wind farms, ξ_{min} = 5% in Section 3

Table 4.27. Oscillation modes with weak damping of Base Case with 2+2GW wind farms, ξ_{min} = 5% in Section 3

Mode number	Eigenvalue	ξ	High participation
Mode 1	–0.487/sec ± *j*0.957Hz	5.08%	G6, G7
Mode 2	–0.403/sec ± *j*0.716Hz	5.62%	G2, G3, G6, G7
Mode 3	–0.470/sec ± *j*0.886Hz	5.29%	G4, G5, G6

Table 4.28. Thermal power plant productions comparison of Base Case with 2+2GW wind farms, SSSC-OPF ξ_{min} = 5% and ξ_{min} = 6% in Section 3

Generator	Active power production [GW]	
	SSSC-OPF, ξ_{min} = 5%	SSSC-OPF, ξ_{min} = 6%
G1	0.140	2.70
G4	9.10	9.43
G6	9.34	6.55
G8	0.175	0.201
G9	0.175	0.175
G10	0.100	0.100

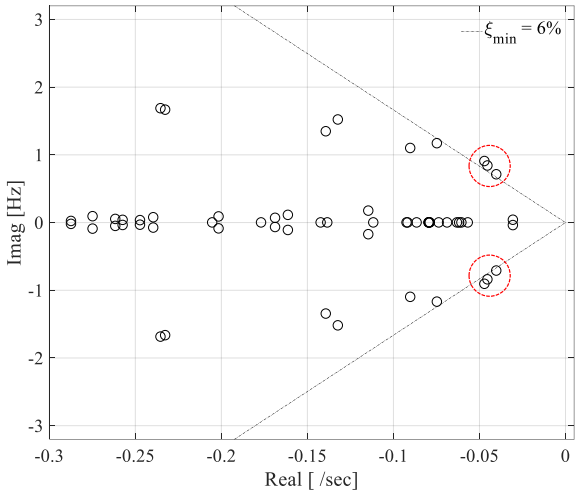

Fig. 4.12. Eigenvalues of Base Case with 2+2GW wind farms, ξ_{min} = 5% in Section 16

Table 4.29. Oscillation modes with weak damping of Base Case with 2+2GW wind farms, ξ_{min} = 5% in Section 16

Mode number	Eigenvalue	ξ	High participation
Mode 1	–0.453/sec ± *j*0.841Hz	5.38%	G4, G2
Mode 2	–0.470/sec ± *j*0.906Hz	5.18%	G7, G6
Mode 3	–0.401/sec ± *j*0.711Hz	5.64%	G6, G2

Table 4.30. Thermal power plant productions comparison of Base Case with 2+2GW wind farms, SSSC-OPF ξ_{min} = 5% and ξ_{min} = 6% in Section 16

Generator	Active power production [GW]	
	SSSC-OPF, ξ_{min} = 5%	SSSC-OPF, ξ_{min} = 6%
G1	1.05	6.55
G4	11.0	7.48
G6	11.0	6.58
G8	0.175	0.175
G9	0.175	0.175
G10	0.100	2.40

Table 4.31. Annual fuel cost comparison of systems by SSSC-OPF, ξ_{min} = 5% and ξ_{min} = 6%

System	Base Case, WF_{2+2GW}, SSSC-OPF, ξ_{min} = 5%	Base Case, WF_{2+2GW}, SSSC-OPF, ξ_{min} = 6%	MTDC *h*), WF_{9+9GW}, SSSC-OPF, ξ_{min} = 5%	MTDC *h*), WF_{9+9GW}, SSSC-OPF, ξ_{min} = 6%
Annual fuel cost [billion JPY]	534	578	457	457

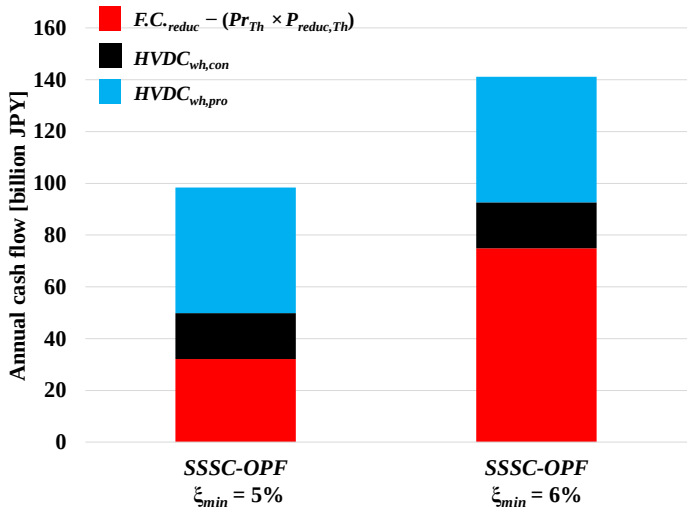

Fig. 4.13. Annual cash flow results of MTDC *h*) with 9+9GW wind farms by SSSC-OPF, ξ_{min} = 5% and ξ_{min} = 6%

Table 4.32. Economic benefits comparison of MTDC *h*) with 9+9GW wind farms by SSSC-OPF, ξ_{min} = 5% and ξ_{min} = 6%

	$Inv.Cost_{MTDC}$ [billion JPY]	NPV [billion JPY]	Profitability Index
SSSC-OPF, ξ_{min} = 5%	638	1930	4.02
SSSC-OPF, ξ_{min} = 6%	638	3050	5.78

5. Evaluations with Transient Stability Constraints

In this chapter, numerical results considering the transient stability constraints of AC and DC grids are analyzed. The configuration of MTDC *h*) system which enables the largest wind power hosting capacity in Chapter 4 is adopted here. The communication link between the left wind farm and the nearby VSC 1 station is taken into consideration. Similarly, the right wind farm and the nearby VSC 2 station have mutual communication link. These links are to deliver wind power output suppression commands when the corresponding VSC is blocked. When a VSC is not able to control its active and reactive power output, a system operation with peak wind outputs becomes unstable without the wind power output suppressions. For instance, the left wind farm output is suppressed to zero immediately after VSC 1 is blocked. The communication latencies between the wind power plants and the VSCs are neglected.

The wind power hosting capacity of MTDC *h*) is revealed to be 5+5GW when the transient stability constraints of AC and DC grids are considered. The PCC bus voltages of wind-farm-connected VSCs are unstable if the total installed wind farm capacity exceeds 5+5GW. As an example, the unstable PCC bus voltage phenomenon by VSC 1 in case of AC fault 1 occurrence is plotted in Fig. 5.1. The fault occurs at 1 sec, which is cleared by removing the faulted transmission line at 1.07 sec.

The unstable PCC bus voltage phenomenon can be explained using $P - V$ curves with low and high wind power plant capacities in Fig. 5.2. Black curves represent the active power and AC voltage relationship in the pre-fault state. After the AC transmission line fault occurrence in Fig. 5.2, the fault is cleared and the faulted AC transmission line is removed. The red curves indicate the active power and AC voltage relationship in this post-fault state. The static characteristic of wind power plant model is represented by the green lines.

In case of low wind power plant capacity, the point of intersection of the green line and the red curve can be found. In other words, the post-fault state is feasible operation when the wind power plant capacity is low. On the other hand, the point of intersection of the green line and the red curve does not exist when the wind power plant capacity is high. The oscillation pattern of the voltage profile in Fig. 5.1 can be explained by this absence of the point of intersection. In fact, this AC voltage oscillation is not the actual system voltage, but represents the absence of the convergence calculation solution in Appendix. After AC fault 1 occurrence, the convergence calculation in Fig. A.1, Appendix tries to find feasible solution, but it fails.

Additional AC transmission lines near the wind power plants are required to increase this wind power hosting capacity considering the transient stability constraints. With the installation of additional AC transmission lines, the post-fault red $P - V$ curve and the green lines for the wind power plant in Fig. 5.2 have a point of intersection again.

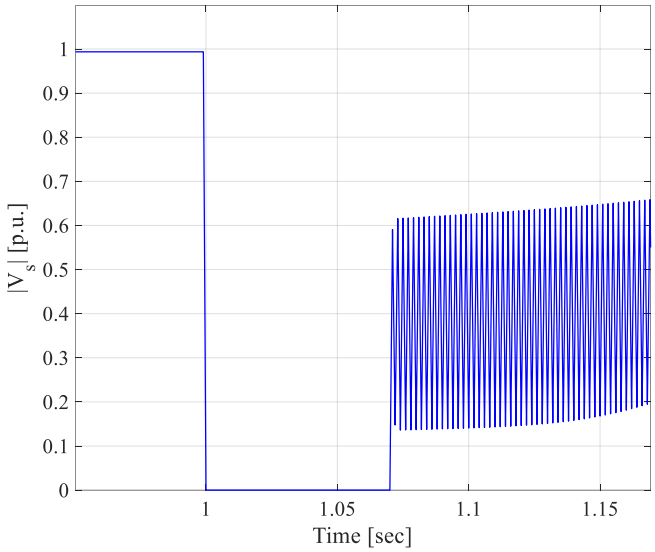

Fig. 5.1. An example of unstable PCC bus voltage by VSC 1

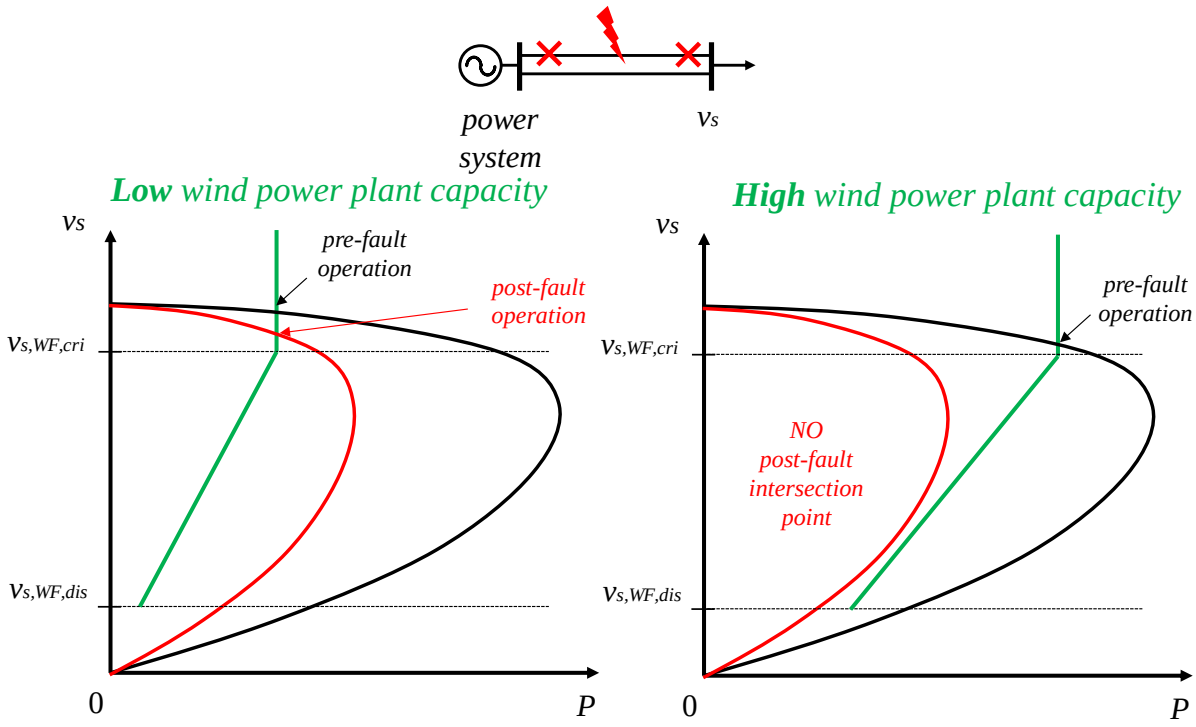

Fig. 5.2. $P-V\,(v_s)$ curves with low and high wind power plant capacities

The results of Step 1 reinforcements and investment costs by SSSC-OPF and transient stability constrained optimal power flow (TSCOPF) analyses are calculated from Table 5.1 to Table 5.4. It can be seen that the reinforcement capacities and total investment costs of VSC converters and DC lines are increased by the transient stability constraints. Bidirectional hybrid DC CBs are also installed at both ends of each DC transmission line in TSCOPF analysis. This leads to additional costs of DC CBs and the increased total investment cost as well.

Table 5.1. Reinforcement result of MTDC *h*) with 5+5GW wind farms by SSSC-OPF Step 1

	Reinforcement [GVA]						
	Period 1	**Period 2**	**Period 3**	**Period 4**	**Period 5**	**Period 6**	**Reinforcement decision**
VSC 1	4.3	3.6	4.1	2.0	2.0	2.4	4.3
VSC 2	3.9	2.4	3.6	1.8	1.9	0.90	3.9
VSC 3	3.4	2.5	2.1	4.9	6.6	3.2	6.6
VSC 4	0.60	0.80	0.80	0	3.0	0.30	3.0
DC line 1	4.3	3.6	4.1	2.0	2.0	2.4	4.3
DC line 2	3.9	2.4	3.6	1.8	1.9	0.90	3.9
DC line 3	3.4	2.5	2.1	4.9	6.6	3.2	6.6

Table 5.2. Investment costs of MTDC *h*) with 5+5GW wind farms by SSSC-OPF Step 1

	Investment cost
VSC	249 billion JPY
DC line	53.5 billion JPY
DC circuit breaker	

Table 5.3. Reinforcement result of MTDC *h*) with 5+5GW wind farms by TSCOPF Step 1

	Reinforcement [GVA]						
	Period 1	**Period 2**	**Period 3**	**Period 4**	**Period 5**	**Period 6**	**Reinforcement decision**
VSC 1	4.5	5.3	4.4	6.1	5.3	6.3	6.3
VSC 2	7.8	7.0	7.9	6.5	8.0	6.4	8.0
VSC 3	2.9	4.1	1.3	5.7	4.7	3.7	5.7
VSC 4	7.1	3.3	7.2	3.7	3.9	3.1	7.2
DC line 1	1.9	2.8	0	2.8	0.90	2.9	2.9
DC line 2	1.2	3.4	1.9	1.4	0.20	2.6	3.4
DC line 3	0.80	1.4	1.2	2.2	1.2	0.70	2.2

Table 5.4. Investment costs of MTDC *h*) with 5+5GW wind farms by TSCOPF Step 1

	Investment cost
VSC	381 billion JPY
DC line	66.7 billion JPY
DC circuit breaker	119 billion JPY

The hourly fuel cost results of the system with MTDC *h*) and 5+5GW wind farms calculated by hierarchical SSSC-OPF and TSCOPF analyses are listed in Table 5.5. The influence of the transient stability constraints on the fuel costs can be inferred from Table 5.5. It should be reminded that the reinforcement capacities of MTDC *h*) system obtained by TSCOPF analysis are larger than those by SSSC-OPF analysis.

It is noteworthy that the fuel cost increments in Sections 3, 5, 6, 9, 12, 15, 17, and 18 are less than 1% whereas noticeable, 4.61 ~ 32.4% in other section numbers. To sum up, the annual fuel costs by SSSC-OPF and TSCOPF analyses are 490 billion JPY and 537 billion JPY respectively.

As for the section numbers with more than 1% of fuel cost increments in TSCOPF analysis, the fuel costs considering only four DC fault locations are calculated in Table 5.6. In such cases, the fuel cost increments in TSCOPF analysis compared to the costs in SSSC-OPF analysis are relatively negligible, less than 2% in Table 5.6 except Section 13. From these results, it can be inferred that the cost increments in TSCOPF analysis are mainly influenced by the transient stability constraints after the occurrence of one of the AC faults.

Active power productions of VSCs 1 and 2 in all section numbers by SSSC-OPF are calculated in Table 5.7. In the section numbers with less than 1% fuel cost increments in TSCOPF analysis, the active power production values of VSCs 1 and 2 are negative. On the contrary, positive active power productions of VSCs 1 and 2 are calculated in SSSC-OPF analysis in cases of the section numbers with higher than 4% fuel cost increments in TSCOPF analysis.

These results can be interpreted as follows. The direction of active power transmission between the upper and lower areas is determined by the amount of the upper area active power consumption and the total wind power output. If the wind power output is sufficient to supply the upper area power consumption, the rest of the wind power output is transmitted towards the lower area. The control system and parameters of MTDC *h*) system in Chapter 2 are designed to cope with this situation with high wind power output. In contrast, when the wind power output is low, the active power produced in the lower area is transmitted towards the upper area to supply the upper area power consumption considering the expensive fuel cost coefficients of the upper area thermal power plants. The high fuel cost increments in Table 5.5 and Table 5.6 indicate the developed control system and parameters are not effective to satisfy the transient stability constraints in case of one of the AC fault occurrences when VSCs 1 and 2 operate in inverter-mode in the pre-fault state.

Section 1 with the highest fuel cost increment 32.4% by TSCOPF is chosen to be discussed as the representative case. The DC grid power flow results obtained by SSSC-OPF and TSCOPF analyses are compared in Fig. 5.3. In SSSC-OPF analysis, VSCs 1 and 2 produce active power P_s towards AC grid side to supply the upper area power consumption. The trajectories of DC bus voltages in Fig. 5.4 imply that using the control method and parameters proposed in Chapter 2, DC bus voltages cannot be controlled effectively when AC fault 2 occurs. Instead, the active power production in the upper area is increased so that VSCs 1 and 2 operate in rectifier-mode by TSCOPF analysis. In particular, since the fuel cost coefficients of G10 are the cheapest among G8, G9, and G10, the increment of G10 production in TSCOPF analysis is the most noticeable, more than 4GW in Table 5.8. Similarly, this phenomenon is also observed in other section numbers with high fuel cost increments in TSCOPF analysis except Sections 7, 8, and 9.

4.58% ~ 6.55% of fuel cost increments in TSCOPF analysis are calculated in Sections 7, 8, and 9 in Table 5.5 despite VSCs 1 and 2 operate in rectifier-mode. These fuel cost increments indicate that the SSSC-OPF solution is not able to satisfy the transient stability constraints in the summer peak-load conditions in case of one of the AC fault occurrences.

The following approaches can be examined to relieve the fuel cost increments in TSCOPF analysis. First of all, the developments of more effective VSC HVDC control systems are required. To be specific, a control method effective from the DC bus voltages viewpoint is necessary to solve the unstable DC bus voltage problem in Fig. 5.4 when the wind power output is low. Another approach is the temporary disconnection of the VSC HVDC system. The primary objective of the multi-terminal VSC HVDC system is the installation of the large-scale wind power plants. The multi-terminal VSC HVDC system with the control system and parameters in Chapter 2 is designed for the conditions with high wind power output. In contrast, the power system operation without the multi-terminal VSC HVDC system is still feasible when the wind power output is not high. Therefore, the temporary disconnection of the multi-terminal VSC HVDC system after an AC fault occurrence can be a good approach in the section numbers with high fuel cost increments in TSCOPF analysis to reduce them.

Table 5.5. Hourly fuel costs between hierarchical SSSC-OPF and TSCOPF (wind farm capacity : 5+5GW, system model with MTDC *h*))

Section number	Hourly fuel cost [million JPY / hour]		Fuel cost difference [%]
	SSSC-OPF	TSCOPF	
Section 1	48.5	64.2	32.4
Section 2	43.2	46.5	7.64
Section 3	32.9	33.0	0.304
Section 4	41.2	43.1	4.61
Section 5	37.3	37.4	0.268
Section 6	29.1	29.1	0
Section 7	138	145	5.07
Section 8	131	137	4.58
Section 9	88.6	94.4	6.55
Section 10	56.9	71.5	25.7
Section 11	53.3	64.1	20.3
Section 12	37.7	37.8	0.265
Section 13	69.9	78.9	12.9
Section 14	56.3	65.1	15.6
Section 15	43.0	43.2	0.465
Section 16	61.0	73.8	21.0
Section 17	41.7	42.0	0.719
Section 18	33.5	33.7	0.597

Table 5.6. Hourly fuel costs between hierarchical SSSC-OPF and TSCOPF with only four DC faults (wind farm capacity : 5+5GW, system model with MTDC *h*))

Section number	Hourly fuel cost [million JPY / hour]		Fuel cost difference [%]
	SSSC-OPF	TSCOPF (only four DC faults are considered)	
Section 1	48.5	49.4	1.85
Section 2	43.2	43.6	0.892
Section 3			
Section 4	41.2	41.6	0.889
Section 5			
Section 6			
Section 7	138	139	0.800
Section 8	131	132	0.448
Section 9	88.6	88.6	0
Section 10	56.9	57.1	0.382
Section 11	53.3	53.7	0.684
Section 12			
Section 13	69.9	74.2	6.14
Section 14	56.3	56.9	1.08
Section 15			
Section 16	61.0	61.4	0.637
Section 17			
Section 18			

Table 5.7. VSCs 1 and 2 active power productions of MTDC *h*) system with 5+5GW wind farms by SSSC-OPF analysis

	Active power production P_s [GW]	
	VSC 1	**VSC 2**
Section 1	1.14	0.465
Section 2	0.476	0.533
Section 3	–1.54	–1.19
Section 4	0.209	0.290
Section 5	–0.479	–0.399
Section 6	–2.40	–2.12
Section 7	–0.691	–0.395
Section 8	–0.767	–0.499
Section 9	–1.28	–1.26
Section 10	0.585	0.466
Section 11	0.168	0.124
Section 12	–2.40	–2.11
Section 13	0.739	0.598
Section 14	0.515	0.327
Section 15	–1.47	–1.10
Section 16	0.401	0.374
Section 17	–0.616	–0.445
Section 18	–2.32	–2.18

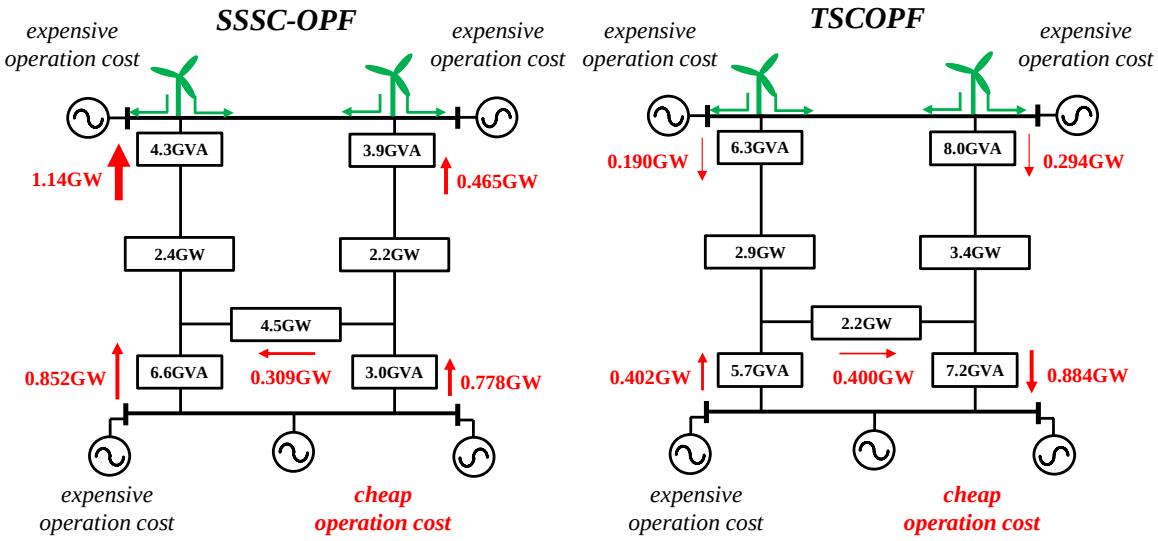

Fig. 5.3. Comparison of DC grid power flow results with 5+5GW wind farms in Section 1 by SSSC-OPF and TSCOPF

Table 5.8. Active power productions of thermal power plants in Section 1 by SSSC-OPF and TSCOPF

	Active power production [GW]	
	SSSC-OPF	**TSCOPF**
G1	0.721	0.786
G4	11.0	8.94
G6	11.0	8.12
G8	0.175	0.191
G9	0.175	0.175
G10	0.100	4.77

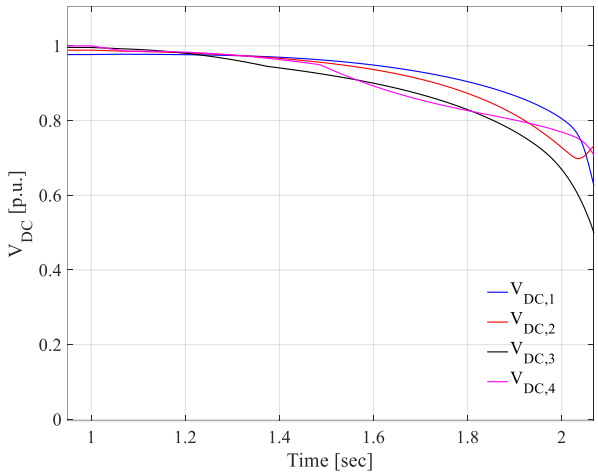

Fig. 5.4. Unstable DC bus voltage trajectories after AC fault 2 in Section 1 by SSSC-OPF

Time-domain simulation results in Section 6 obtained by the hierarchical TSCOPF Step 1 and Step 2 analyses with 5+5GW wind farms are plotted as representative examples. The amount of the active power transmission from the upper area towards the lower area is the largest due to the lowest upper area load consumptions and peak wind outputs. Hence, Section 6 condition can be interpreted as the most critical scenario among all peak wind power output conditions.

4th order Runge-Kutta method is adopted for the integration calculation in time-domain simulation. The unit time step for AC faults simulation is 1*ms*. As for DC faults, the unit time step during the first 1.5 seconds after a fault occurrence is 0.2*ms*. Since the behaviors of HVDC grids are faster than those of conventional AC grids, a shorter unit time step is desirable for the calculation to obtain accurate results. This time step should be determined considering the accuracy of the results and computational burden. Based on these aspects, the unit time step after 1.5 seconds of a fault occurrence is 1*ms*. These different time step settings enable us to simulate sub-transient system behaviors accurately and obtain the results quickly.

The time-domain simulation results for all five AC faults and four DC faults are plotted from Fig. 5.5 to Fig. 5.13. As for the signs of P_s and Q_s, positive values of P_s and Q_s indicate a VSC produces active and leading reactive power outputs and injects them into AC grid side. Either AC fault or DC fault occurs at 1 second. In case of an AC fault occurrence, the fault is removed after 70*ms* by opening the faulted AC line which is reconnected after 1 second. Hence, the system is recovered at 2.07 seconds in the following figures below. In case of a DC fault occurrence, artificial zero DC current is produced by hybrid DC CBs after 5*ms*. Then, the DC fault can be removed by removing the faulted DC line. The system can be recovered after V_{DC} recovery process as explained in Chapter 2. It is revealed that the solution obtained by the hierarchical TSCOPF analysis is stable while satisfying all transient stability constraints for all fault locations.

First of all, the time-domain simulation results with AC fault 1 are drawn in Fig. 5.5. It can be seen in Fig. 5.5(a) and (b) that the fluctuations of generator rotor-angles and rotational speeds are relatively lower than those with other AC faults. The reason can be inferred from the active power productions of the thermal power plants in Table 5.9. The active power productions of G8, G9, and G10 are very low, in their respective minimum production values. Therefore, the influence of an AC fault near these power plants is relatively lower than that of other AC faults.

As can be seen in Fig. 5.5(c) and (d), the active and reactive power productions of VSC 1 are zero during 1 ~ 1.07s. In Fig. 5.5(e), the PCC bus voltage v_s of VSC 1 drops below 0.2 *p.u.*. As a result, VSC 1 is blocked during AC fault 1. The active power production of the left wind farm is suppressed to zero when VSC 1 is blocked. This means the total active power production in the upper area is reduced. This results in the decelerations of G8, G9, and G10 after AC fault 1 occurrence in Fig. 5.5(b).

In the pre-fault state during 0 ~ 1s, VSCs 1, 2, and 4 produce approximately 5,000MVAR of leading reactive power output in Fig. 5.5(d). This implies the necessity of VSC converter stations instead of LCC-based converters. In order to investigate the necessity of the reactive power output controllability, the preliminary simulation with the reactive power outputs of all VSCs being zero is carried out. In such case, the solutions of TSCOPF analysis are not found when 5+5GW wind farms are installed.

In the pre-fault state, both VSCs 1 and 2 inject active power into the DC grid side for wind power transmission towards the lower area. During AC fault 1 occurrence, $P_{s,1}$ in Fig. 5.5(c) cannot be transmitted when VSC 1 is blocked. Therefore, DC bus 1 voltage $V_{DC,1}$ drop near VSC 1 is measured after AC fault 1 occurrence in Fig. 5.5(f).

***AC fault 1* (*AC fault near VSC 1*)**

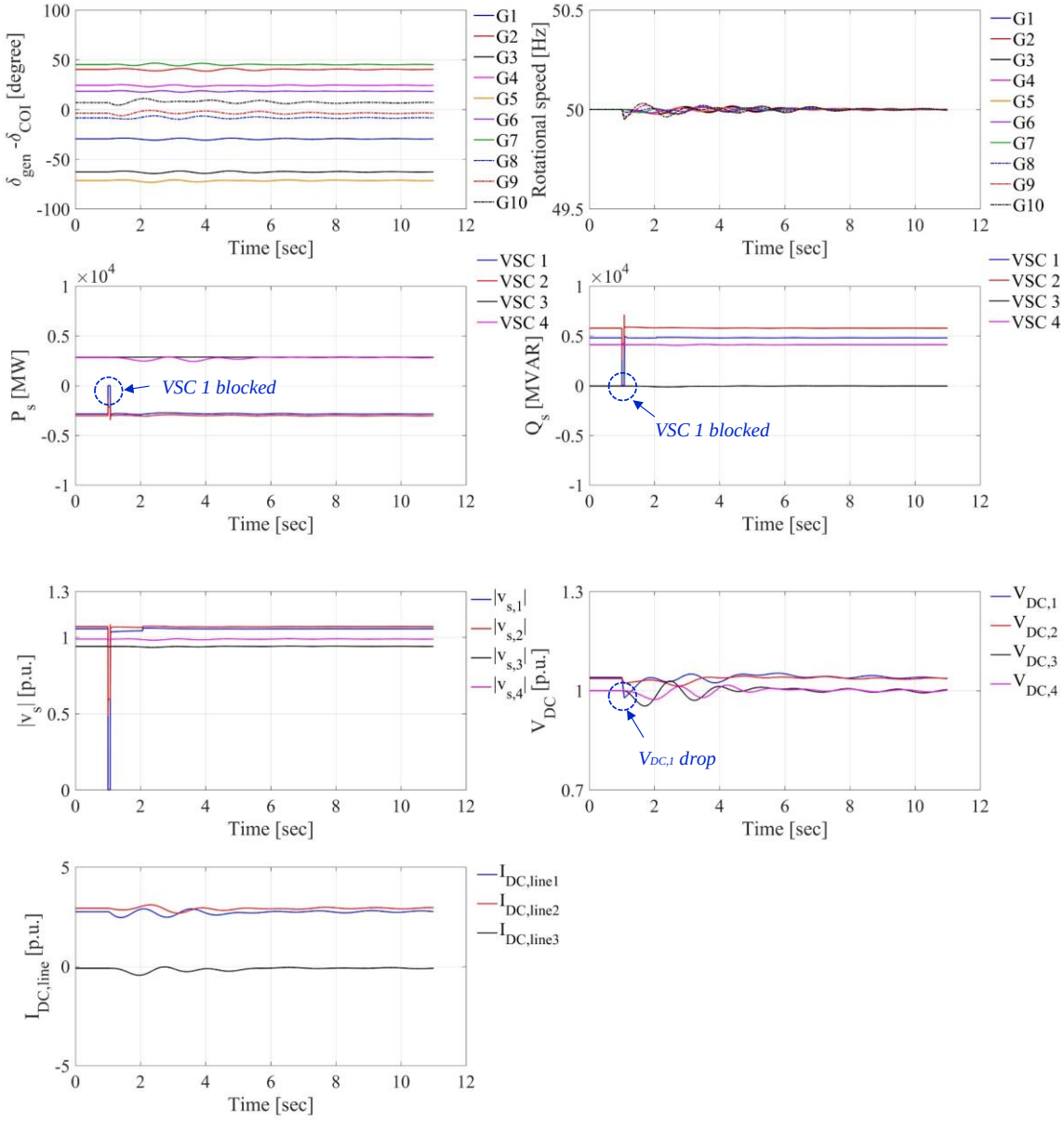

Fig. 5.5. Time-domain simulation results with AC fault 1 by hierarchical TSCOPF in Section 6

(a) Trajectories of generators' rotor-angles with respect to COI
(b) Trajectories of generators' rotational speed
(c) Trajectories of VSC active power outputs
(d) Trajectories of VSC reactive power outputs
(e) Trajectories of VSC PCC bus voltage magnitudes
(f) Trajectories of DC bus voltages
(g) Trajectories of DC transmission line current flows

Table 5.9. Active power productions of thermal power plants by hierarchical TSCOPF analysis in Section 6

	Active power production [GW]
G1	0.140
G4	4.48
G6	4.38
G8	0.175
G9	0.175
G10	0.100

The time-domain simulation results with AC fault 2 are described in Fig. 5.6. The magnitudes of the transient fluctuations in Fig. 5.6 are relatively larger than those in Fig. 5.5. In Fig. 5.6(c), sudden active power outputs P_s changes are observed, especially by VSC 4 near t = 1.7s. DC bus 4 voltage near VSC 4 swells above 0.05 *p.u.* compared to the pre-fault operation at this moment, which triggers V_{DC} droop controller. The sudden active power outputs $P_{s,3}$ change by VSC 3 in Fig. 5.6(c) can also be explained with the same principle.

After the fault occurrence, all DC bus voltages in Fig. 5.6(f) swell above their respective pre-fault values. As can be seen in Fig. 5.6(c), the active power output $P_{s,4}$ of VSC 4 is reduced after the fault occurrence. In other words, the amount of active power ejection from DC grid towards AC grid by VSC 4 is reduced after the fault occurrence. Consequently, the unbalance of active power in the entire DC grid results in these DC bus voltage swells.

The trajectories with other three AC fault locations plotted in Fig. 5.7 to Fig. 5.9 can also be explained with similar explanations above. In case of either AC fault 3 or AC fault 4 occurrence, the corresponding VSC converter is blocked if the PCC bus voltage magnitude drops below 0.2 *p.u.*. The active and reactive power outputs of the blocked converter are zero during the fault occurrence. As for the relationship between DC bus voltages and the active power productions of VSCs, the reduced active power production of the inverter-mode converter in the pre-fault operation leads to the DC bus voltage swells.

***AC fault 2* (*AC tie-line side fault*)**

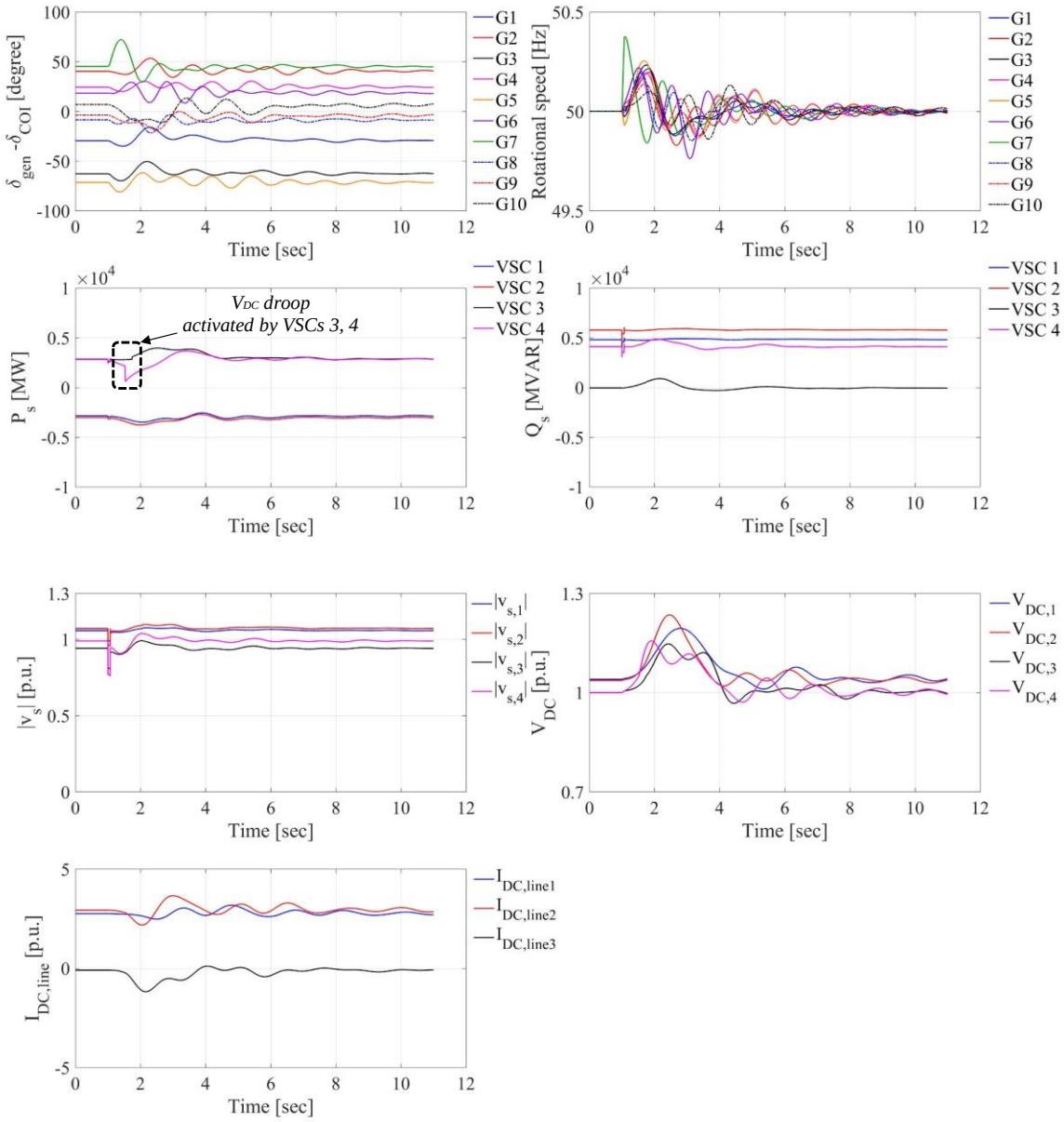

Fig. 5.6. Time-domain simulation results with AC fault 2 by hierarchical TSCOPF in Section 6
(a) Trajectories of generators' rotor-angles with respect to COI
(b) Trajectories of generators' rotational speed
(c) Trajectories of VSC active power outputs
(d) Trajectories of VSC reactive power outputs
(e) Trajectories of VSC PCC bus voltage magnitudes
(f) Trajectories of DC bus voltages
(g) Trajectories of DC transmission line current flows

***AC fault 3* (*AC fault near VSC 3*)**

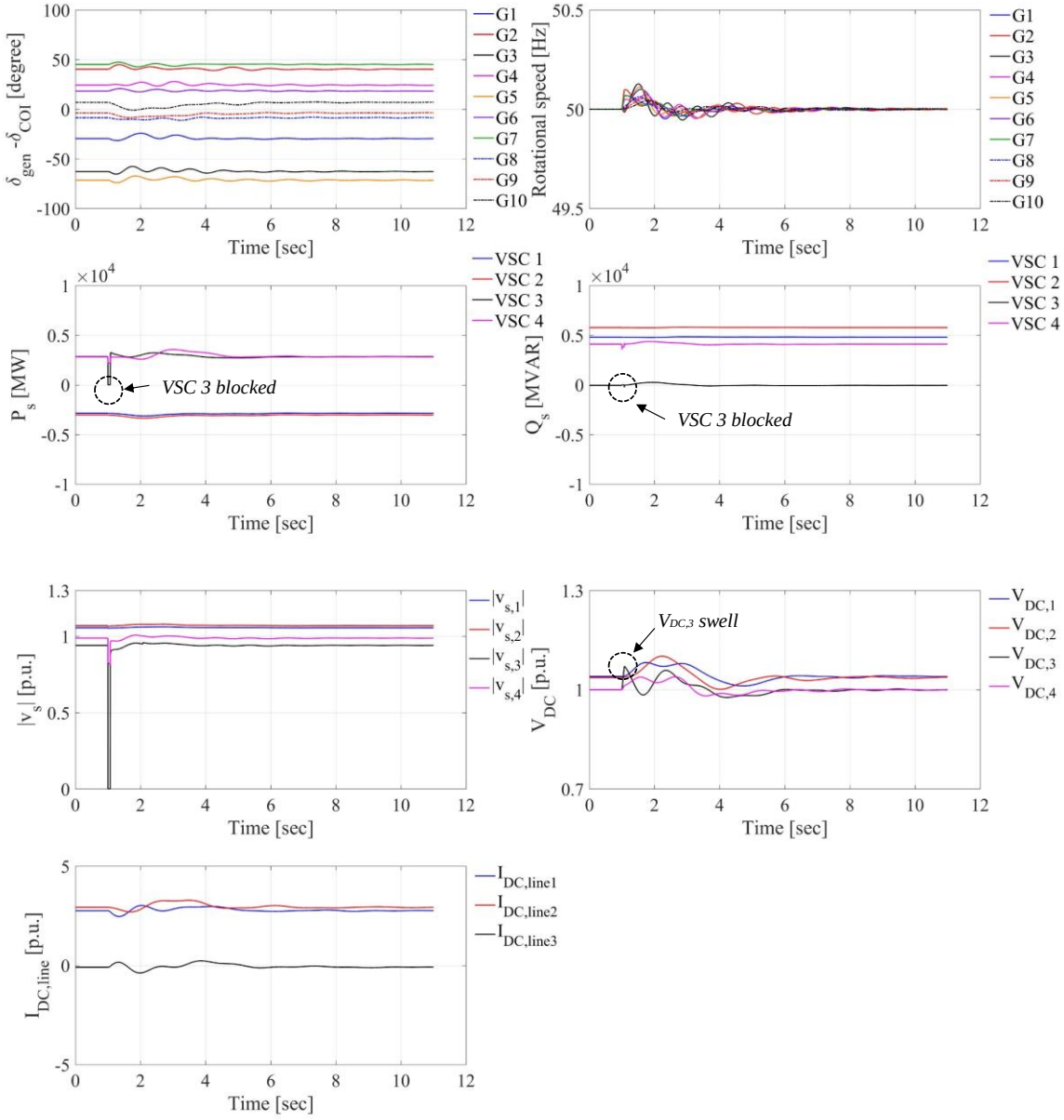

Fig. 5.7. Time-domain simulation results with AC fault 3 by hierarchical TSCOPF in Section 6
(a) Trajectories of generators' rotor-angles with respect to COI
(b) Trajectories of generators' rotational speed
(c) Trajectories of VSC active power outputs
(d) Trajectories of VSC reactive power outputs
(e) Trajectories of VSC PCC bus voltage magnitudes
(f) Trajectories of DC bus voltages
(g) Trajectories of DC transmission line current flows

***AC fault 4* (*AC fault near VSC 4*)**

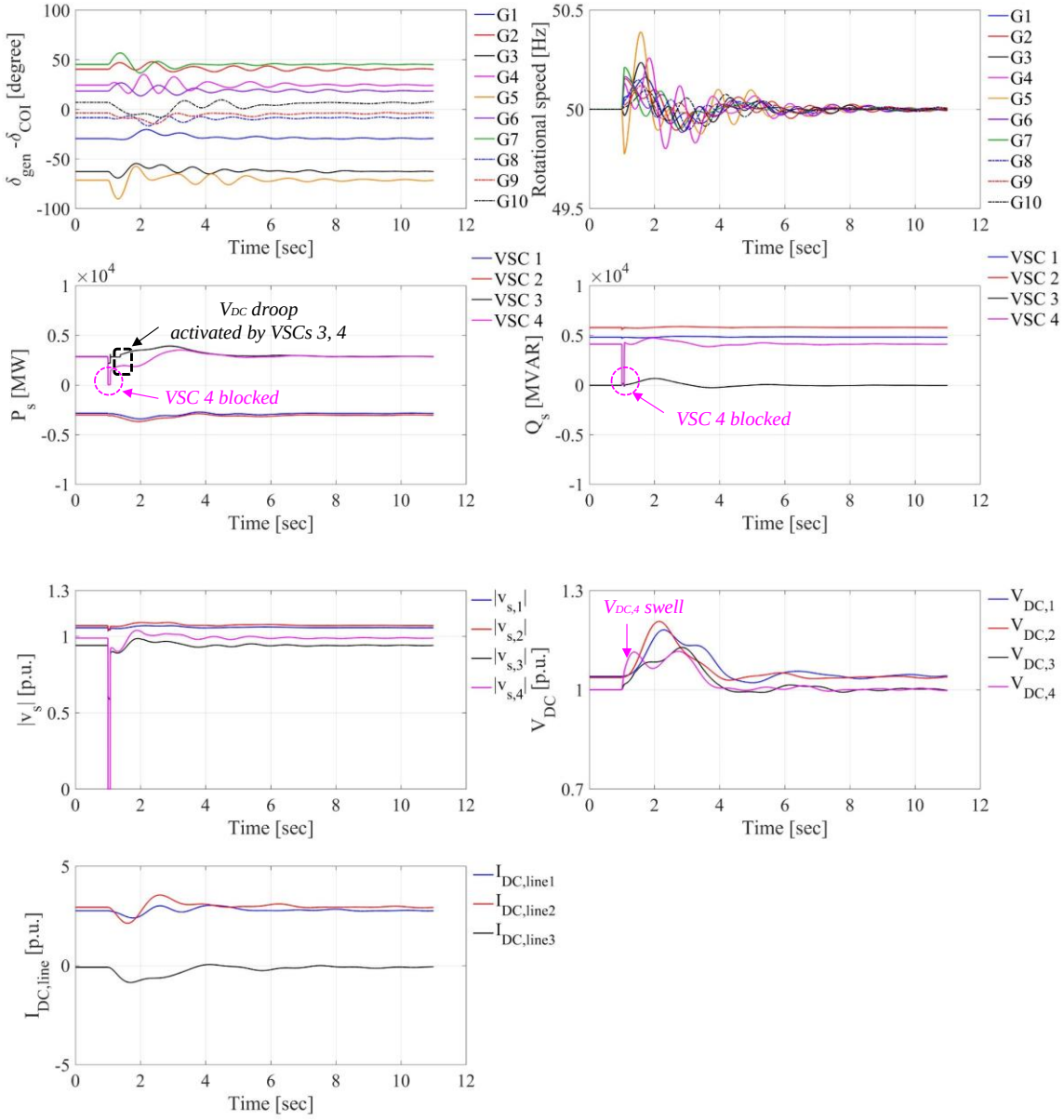

Fig. 5.8. Time-domain simulation results with AC fault 4 by hierarchical TSCOPF in Section 6
(a) Trajectories of generators' rotor-angles with respect to COI
(b) Trajectories of generators' rotational speed
(c) Trajectories of VSC active power outputs
(d) Trajectories of VSC reactive power outputs
(e) Trajectories of VSC PCC bus voltage magnitudes
(f) Trajectories of DC bus voltages
(g) Trajectories of DC transmission line current flows

***AC fault 5* (*AC fault close to AC bus 35*)**

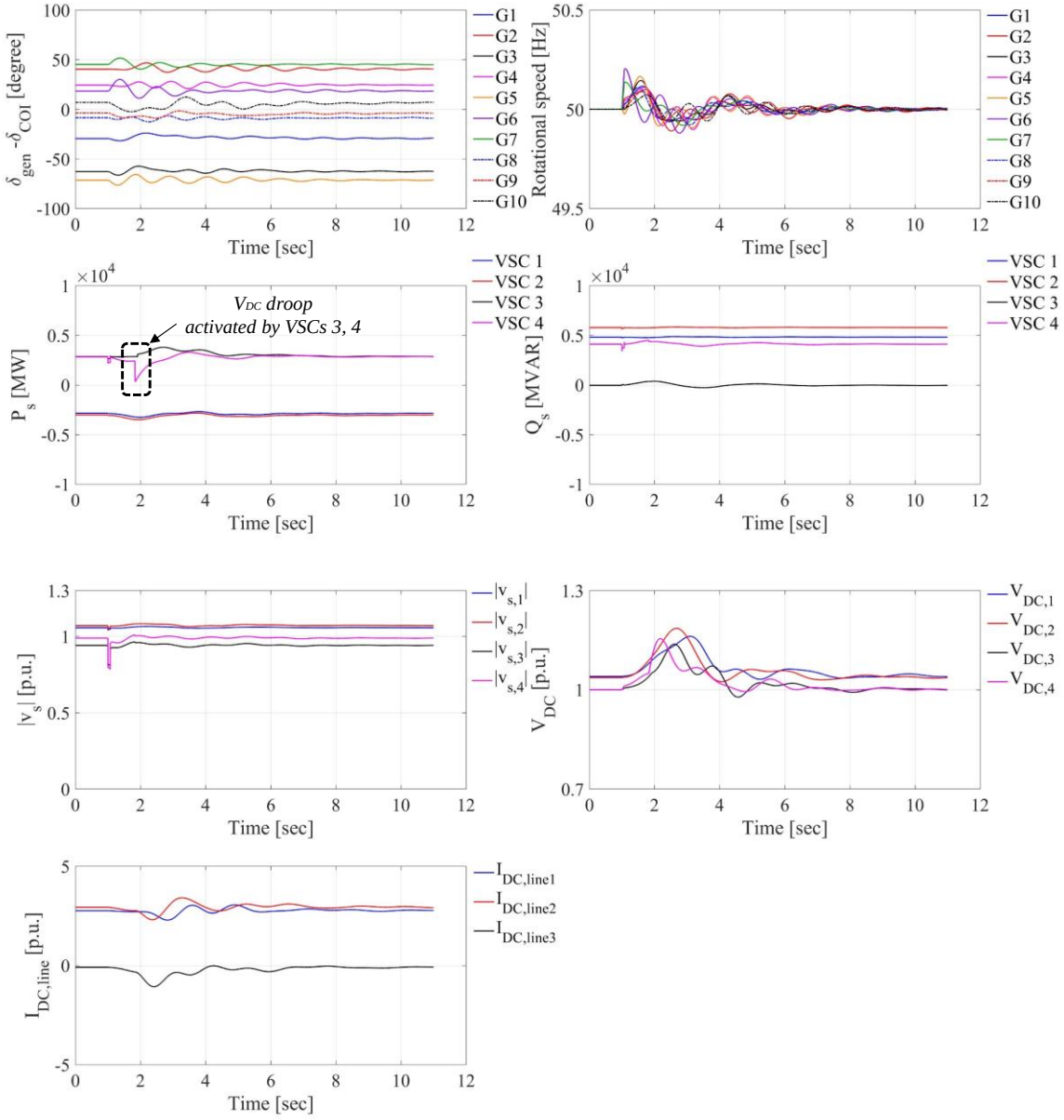

Fig. 5.9. Time-domain simulation results with AC fault 5 by hierarchical TSCOPF in Section 6
(a) Trajectories of generators' rotor-angles with respect to COI
(b) Trajectories of generators' rotational speed
(c) Trajectories of VSC active power outputs
(d) Trajectories of VSC reactive power outputs
(e) Trajectories of VSC PCC bus voltage magnitudes
(f) Trajectories of DC bus voltages
(g) Trajectories of DC transmission line current flows

The time-domain simulation results with DC faults 1 and 2 are plotted in Fig. 5.10 and Fig. 5.11 respectively. After DC fault 1 occurrence, VSC 1 is blocked to protect the converter. As a consequence, the left wind farm is required to suppress its power production to zero. This results in the similar decelerations phenomenon of G8, G9, and G10 in Fig. 5.10(b) as that in Fig. 5.5(b).

In Fig. 5.10(d) and (e), abrupt Q_s and v_s changes are observed by VSCs 1 and 2 at t = 1s and 1.155s. These phenomena are due to the operations of the wind farms. At t = 1s and 1.155s, VSC 1 is blocked and de-blocked. As a result, the active power production of the left wind farm is suppressed to zero and recovered at these moments. On top of that, the production of the right wind farm also depends on the magnitude of $v_{s,2}$ which shows abrupt change at these moments. These abrupt wind power output changes lead to the sudden fluctuations of Q_s and v_s near the wind farms.

As can be seen in Fig. 5.10(f), DC bus 1 voltage near VSC 1 drops to zero after DC fault 1 occurrence. After t = 1.155s, VSC 1 is de-blocked and able to produce active and reactive power outputs. V_{DC} recovery process is executed for the DC voltage at the fault location to be recovered close to the pre-fault value. If the DC faulted transmission line is re-operated without this V_{DC} recovery process, huge DC transmission line currents flow as explained in Chapter 2. The reactive power output reference Q_s^* is assigned to be identical to the pre-fault production, $Q_{s,0}$. Active power is supplied by VSC 1 from AC grid towards DC grid during V_{DC} recovery process as drawn in Fig. 5.10(c). This V_{DC} recovery process is finished after DC bus 1 voltage is recovered above 0.8 *p.u.*.

It is shown in Fig. 5.10(g) that the faulted DC transmission line 1 does not operate during DC fault 1 and V_{DC} recovery process. It is re-connected and DC transmission line 1 current starts to flow after V_{DC} recovery process is finished.

This explanation is also valid for the time-domain simulation results with DC fault 2 in Fig. 5.11.

***DC fault 1* (*DC fault near VSC 1*)**

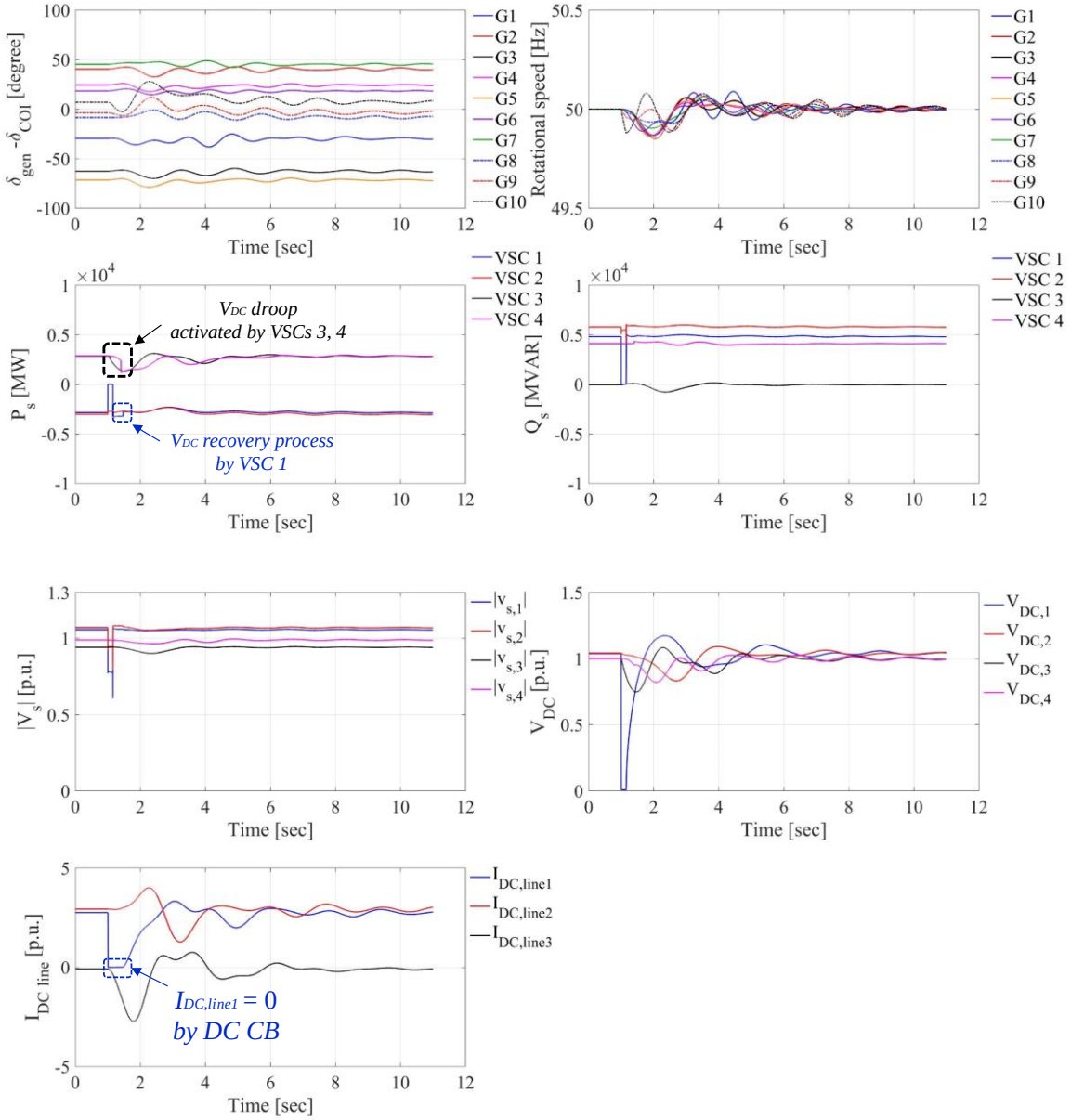

Fig. 5.10. Time-domain simulation results with DC fault 1 by hierarchical TSCOPF in Section 6
(a) Trajectories of generators' rotor-angles with respect to COI
(b) Trajectories of generators' rotational speed
(c) Trajectories of VSC active power outputs
(d) Trajectories of VSC reactive power outputs
(e) Trajectories of VSC PCC bus voltage magnitudes
(f) Trajectories of DC bus voltages
(g) Trajectories of DC transmission line current flows

DC fault 2 (DC fault near VSC 2)

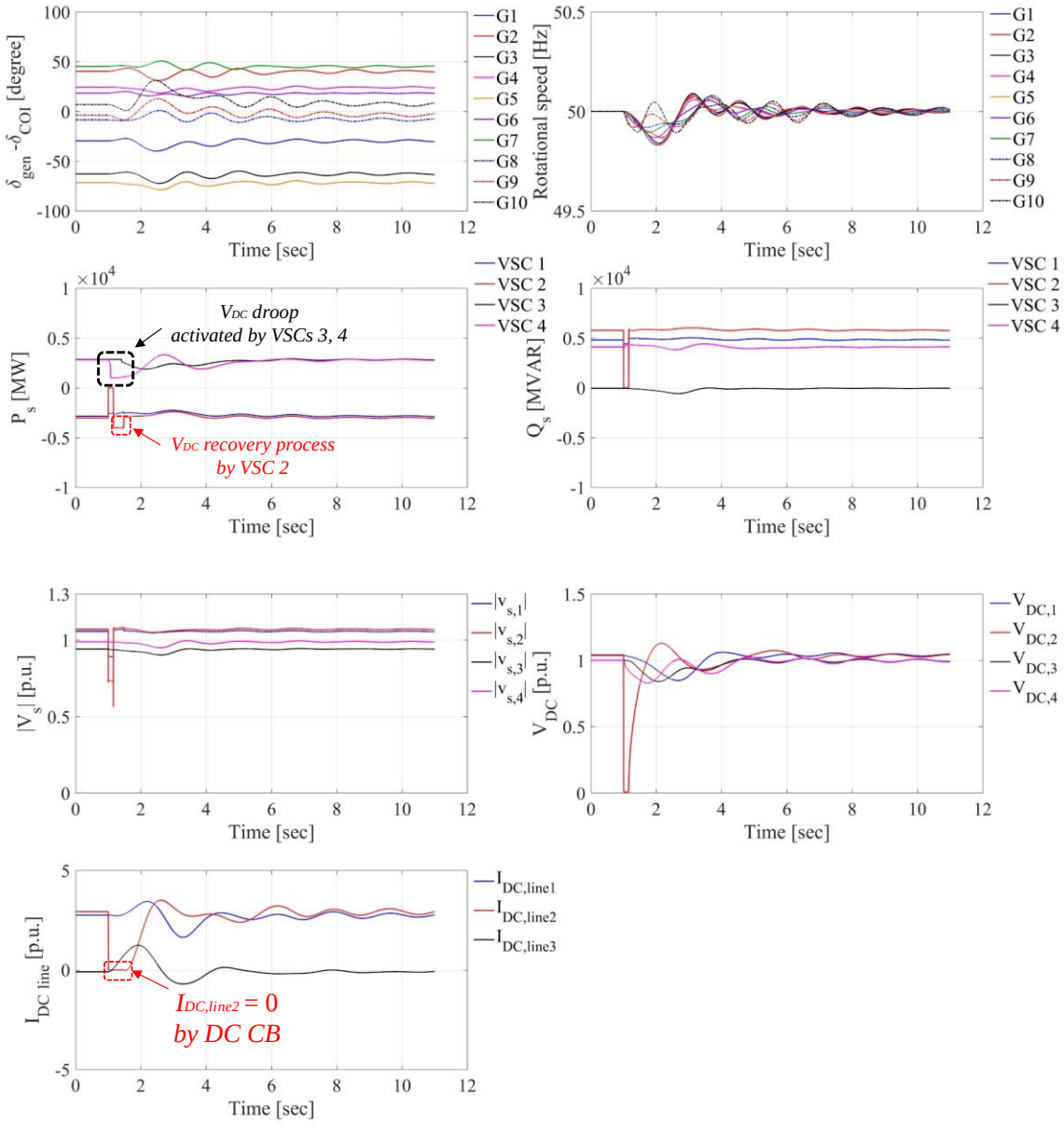

Fig. 5.11. Time-domain simulation results with DC fault 2 by hierarchical TSCOPF in Section 6

(a) Trajectories of generators' rotor-angles with respect to COI

(b) Trajectories of generators' rotational speed

(c) Trajectories of VSC active power outputs

(d) Trajectories of VSC reactive power outputs

(e) Trajectories of VSC PCC bus voltage magnitudes

(f) Trajectories of DC bus voltages

(g) Trajectories of DC transmission line current flows

The time-domain simulation results with DC fault 3 are shown in Fig. 5.12.

It is noteworthy to focus on the fluctuations of G1 in Fig. 5.12(a) and (b). In the pre-fault operation, VSC 3 is in inverter-mode supplying active power towards AC grid side. This active power cannot be supplied when VSC 3 is blocked during the fault occurrence. This active power imbalance near G1 triggers the deceleration of G1 rotational speed close to 49.9Hz while VSC 3 is blocked during t = 1 ~ 1.155s. After the fault is cleared, V_{DC} recovery process is carried out by VSC 3. During this period, more than 4,000MW of active power is supplied from AC grid towards DC grid by VSC 3 as can be seen in Fig. 5.12(c). As a consequence, the rotational speed of G1 decreases further near 49.6Hz in Fig. 5.12(b).

During V_{DC} recovery process, even though the reactive power output reference is assigned to be its pre-fault value, the practical reactive power output of VSC 3 is not perfectly matched with the pre-fault value as can be seen in Fig. 5.12(d). This is due to the fact that the active power output of VSC 3 is also different from the pre-fault active power output in Fig. 5.12(c). The deviation of VSC 4 reactive power output during V_{DC} recovery process in Fig. 5.13(d) after DC fault 4 can also be explained by this principle. These behaviors are noticeable for the VSCs with inverter-mode in the pre-fault operation.

In the pre-fault state, wind power is transmitted into the DC grid by VSCs 1 and 2. After DC fault 3, the active power injected by VSC 1 into the DC grid cannot be transmitted since the DC transmission line 1 is disconnected. This results in the active power imbalance at DC bus 1. Hence, DC bus 1 voltage swell near 1.38 *p.u.* is observed in Fig. 5.12(f).

In case of DC fault 3 occurrence, the DC transmission lines 1 and 3 are disconnected during the fault occurrence and V_{DC} recovery process. As a consequence, the DC transmission line current flows through these lines are zero as plotted in Fig. 5.12(g).

The time-domain simulation results with DC fault 4 in Fig. 5.13 can also be interpreted in the similar way.

***DC fault 3* (*DC fault near VSC 3*)**

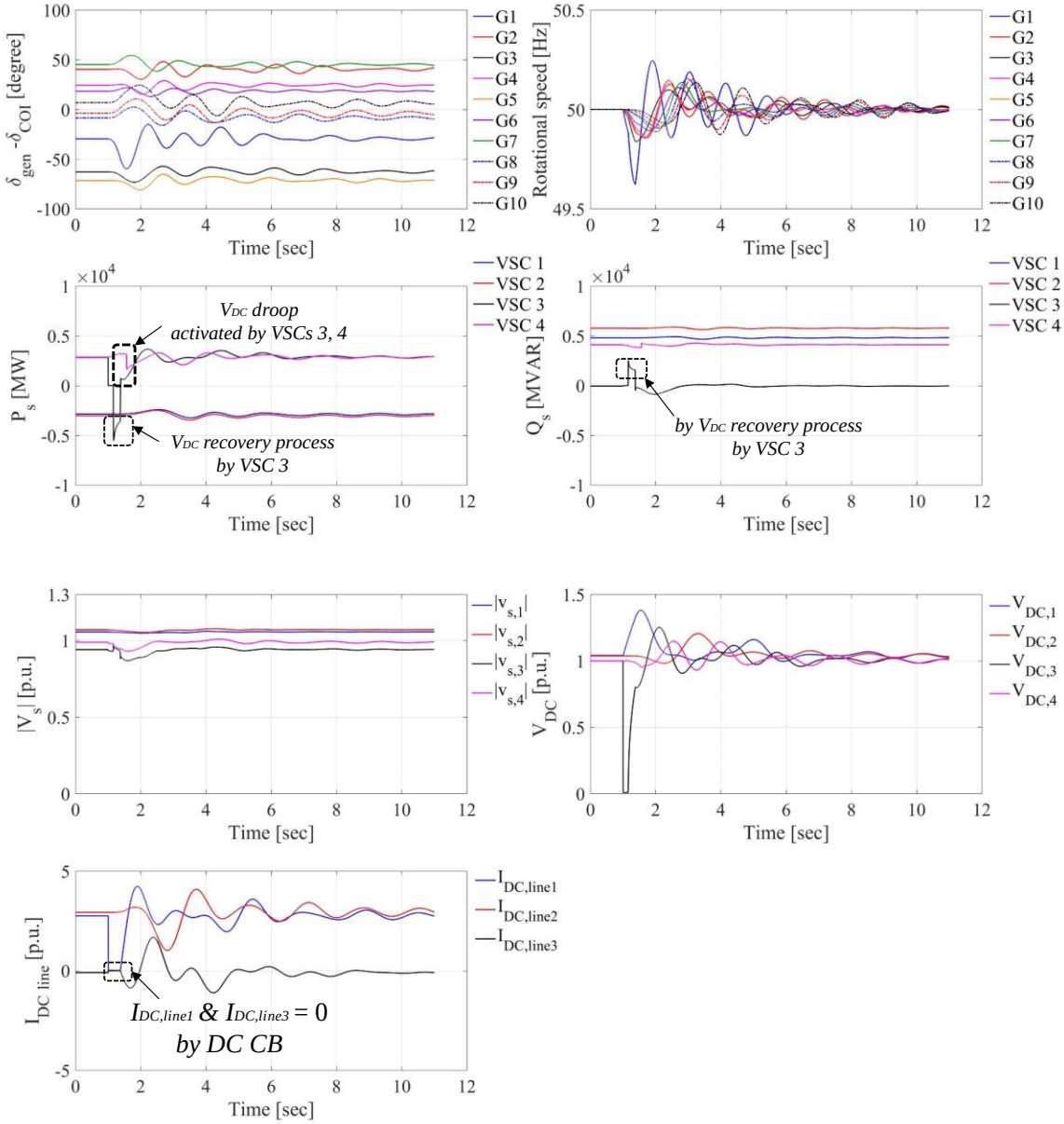

Fig. 5.12. Time-domain simulation results with DC fault 3 by hierarchical TSCOPF in Section 6
(a) Trajectories of generators' rotor-angles with respect to COI
(b) Trajectories of generators' rotational speed
(c) Trajectories of VSC active power outputs
(d) Trajectories of VSC reactive power outputs
(e) Trajectories of VSC PCC bus voltage magnitudes
(f) Trajectories of DC bus voltages
(g) Trajectories of DC transmission line current flows

DC fault 4 (DC fault near VSC 4)

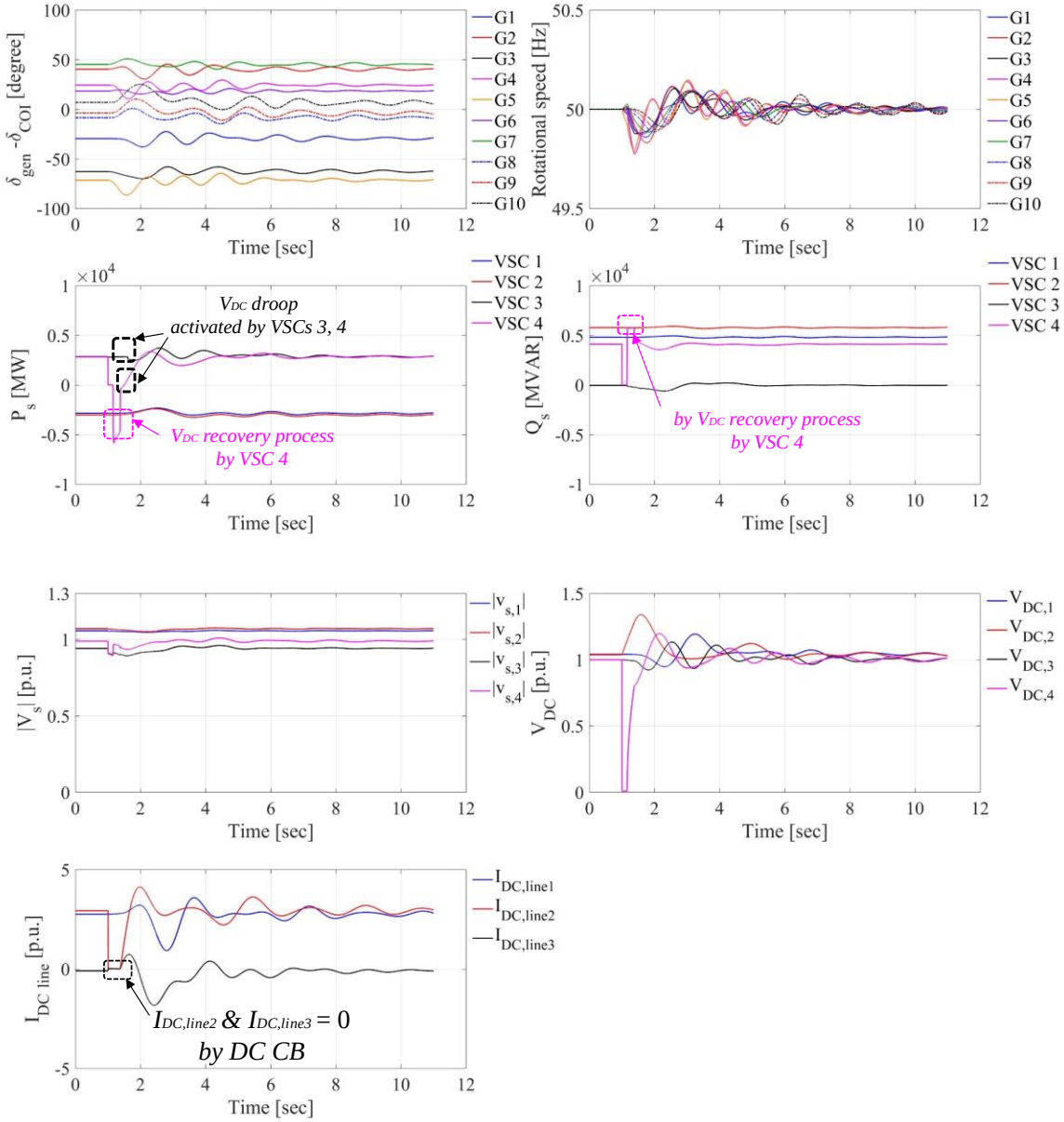

Fig. 5.13. Time-domain simulation results with DC fault 4 by hierarchical TSCOPF in Section 6
(a) Trajectories of generators' rotor-angles with respect to COI
(b) Trajectories of generators' rotational speed
(c) Trajectories of VSC active power outputs
(d) Trajectories of VSC reactive power outputs
(e) Trajectories of VSC PCC bus voltage magnitudes
(f) Trajectories of DC bus voltages
(g) Trajectories of DC transmission line current flows

6. Conclusions and Future Works

The large-scale installations of renewable energy sources in power systems are currently inevitable issues. Focusing on the large amount of wind energy utilization in Japan, the necessity of long-distance transmission has been discussed. Two critical problems, the power system stability aggravation triggered by the large-scale long-distance transmission and the low economic benefits of the transmission systems have been explained to be overcome.

In this context, hierarchical stability constrained optimal power flow in mixed AC / multi-terminal VSC HVDC systems with large-scale wind power plants has been formulated. This aims at solving the critical problems of wind power transmission. Firstly, by considering the power system stability as additional inequality constraints of the optimization process, the obtained solution is stable from the stability viewpoints. Furthermore, the capacity factor and as a result, the economic benefits obtained by the transmission system can be increased by flexible multi-terminal VSC HVDC system operations.

As the power system model, the IEEJ EAST 10-machine System Model has been adopted to simulate the large-scale wind power plants installation in Japan. The reinforcement with either AC transmission system or a multi-terminal VSC HVDC system has been considered for the installation of the wind power plants if necessary.

Hierarchical stability constrained optimal power flow approach has been suggested considering both the reinforcements and operations of the power system models. Various scenarios with different seasons, load patterns, and wind power outputs have been analyzed. Small-signal stability and transient rotor-angle stability of AC grid have been considered since this rotor-angle stability issue is the most critical constraint for the long-distance inter-area AC power transmission in the current Japanese power system. Moreover, the transient PCC bus voltages of a VSC HVDC system, transient DC bus voltages, and the fluctuations of DC transmission line current flows have also been taken into account for proper VSC HVDC system operation.

To begin with, the wind power hosting capacities considering the small-signal stability constraint have been calculated for the aim of the installation of the large-scale wind power plants. Compared to the AC transmission systems whose wind power hosting capacities are limited by the small-signal stability, the hosting capacities of MTDC systems are revealed to be larger. Among many MTDC systems, the MTDC system which enables the largest wind power hosting capacity has been found.

Given the hosting capacity results, the economic benefit analysis considering the reinforcement decisions and operations of the MTDC systems has been carried out to evaluate the benefits obtained by the proposed hierarchical OPF method. Based on the economic benefit analysis, the sensitivity analysis of the wind power capacities and the small-signal stability constraints has been carried out.

The influence of the transient stability constraints on the hosting capacity has been investigated. It has been revealed that the transient PCC bus voltage issue when an AC fault near the wind power plants is the most critical factor limiting the hosting capacity. The reinforcements of AC transmission lines near the wind power plants are needed to increase the hosting capacity.

The MTDC reinforcement and system operation results considering the transient stability constraints have been discussed. In order to focus on the influence of the transient stability constraints, the results with and without the transient stability constraints have been compared. Time-domain simulation results with AC and DC faults have been explained to understand the transient behaviors of mixed AC / multi-terminal VSC HVDC systems with the wind power plants.

The detailed conclusion of each chapter is summarized below. The accomplishments of this dissertation are expected to expedite future power systems with renewable energy sources using VSC HVDC systems.

Chapter 1

For the aim of massive wind energy utilizations in Japan, the necessity of HVDC transmission systems has been suggested for the long-distance large-scale wind power transmission. The characteristics of LCC and VSC based HVDC systems are compared. The basic multi-terminal topologies and VSC converter configurations have been explained. The related previous works regarding the transmission expansion planning and operation of VSC HVDC systems for the transmission of renewable energy source outputs have been surveyed to distinguish the major contributions of this dissertation from the works. The objectives and structure of this dissertation have been summarized.

Chapter 2

To begin with, the synchronous generator model of conventional AC system has been explained. The synchronous generator model is modified based on feasible assumptions for time-domain simulation. Each synchronous generator model has been considered to be equipped with AVR and GOV systems with first order lag transfer functions. Voltage and frequency dependencies of AC system loads have been discussed. In this dissertation, all AC system loads have been considered as static constant impedance characteristic models for the simplicity. The aggregated wind power plants modeled as static loads considering the FRT requirement have been included as well.

Many types of VSC HVDC system models have been summarized. Among them, the average value model with control system has been adopted and explained only considering symmetrical bi-pole behaviors of power system models. As regards the DC voltage control cooperation of multi-terminal VSC HVDC systems, voltage margin method and DC voltage droop control have been discussed. The modified DC voltage control cooperation which utilizes the characteristics of both methods has been adopted in this dissertation. The FRT requirement of VSC HVDC systems has been considered.

The protection strategy of mixed AC / multi-terminal VSC HVDC systems has been explained. Hybrid-type DC circuit breakers have been adopted to clear DC faulted sections and produce artificial zero DC current quickly and selectively. After a DC fault clearance, DC voltage recovery process is carried out if a significant DC voltage drop occurs.

A Japanese power system model with wind power plants has been adopted to simulate the long-distance large-scale wind power transmission scenario in Japan. In order for the installations

of the large-scale wind power plants, power system reinforcements with either new AC transmission systems or a MTDC system have been considered if necessary.

Chapter 3

Instead of the strict long-term economic benefit analysis during the whole life-time of a VSC HVDC system, a simplified annual analysis has been suggested. One year has been classified into different section numbers depending on the conditions of seasons, load patterns, and wind power outputs.

Hierarchical stability constrained optimal power flow has been formulated to calculate the reinforcement decisions and operations of MTDC systems. Since power system stability is the critical issue as for the long-distance large-scale wind power transmission, the small-signal stability constraints, the transient fluctuations of generators' rotor-angles, PCC bus voltages, DC bus voltages, and DC transmission line current flows have been taken into account as additional constraints. As a consequence, the obtained OPF solutions are stable from all these stability viewpoints.

In order to solve this optimization problem, differential evolution algorithm has been adopted. The stability constraints can be easily handled using fitness functions and penalty values in this evolutionary algorithm.

Chapter 4

To begin with, the wind power hosting capacities of power system models considering the small-signal stability constraints have been surveyed. It has been revealed that unlike pure AC systems which suffer from the small-signal instability problem, the system model reinforced with a MTDC system is free from such problem.

Several different multi-terminal topologies have been considered. The corresponding hosting capacities of the MTDC systems have been calculated. The critical factor determining different hosting capacities is AC transmission line capacities nearby the inverter-mode VSCs. The MTDC system which enables the largest wind power hosting capacity has been revealed that AC transmission lines nearby the inverter-mode VSCs have sufficient capacities. Considering the largest hosting capacity is constrained by the minimum thermal power plant production limits, additional energy storage systems are required to increase the wind power hosting capacity.

A novel economic benefit analysis has been proposed to evaluate the economic benefits obtained by the installations of wind power plants, MTDC reinforcements, and operations. The fuel cost reduction effects and increased wheeling charge incomes of MTDC systems have been included in cash inflow terms. As for the fuel cost reduction effect, the contributions of wind power plants and the proposed method using MTDC systems have been defined separately to exclude the effect by the wind power plants. Net present values and profitability indices have been calculated to evaluate the economic benefits of the proposed method using MTDC systems.

By the sensitivity analysis of wind power capacity, the following discussions have been obtained. As the total capacity of the wind power plants increases, higher annual cash flow and NPV of the MTDC system have been obtained. Regarding the MTDC investment efficiency, the

results of PI indicate the wind power capacity which results in the maximum investment efficiency exists.

The sensitivity analysis of small-signal stability constraints has also been carried out. Different damping ratio constraints have been taken into account in the analysis. When a strict damping ratio constraint is considered in a system without any MTDC systems, the annual fuel cost result is increased. On the contrary, the annual fuel cost of the system with a MTDC system is not influenced by the same damping ratio constraint thanks to the system stabilization effect of the MTDC system. The increased fuel cost reduction benefit of the MTDC system has been obtained by the considerations of strict damping ratio constraints. As a result, the results of NPV and PI have also been increased.

Chapter 5

It has been revealed that the wind power hosting capacity is reduced by the consideration of the transient stability constraints. Transient voltage instability after the AC fault occurrence near the wind power plants is critical. From this aspect, AC transmission line reinforcements close to the wind power plants are required to increase wind power hosting capacity.

Given the hosting capacity, the hierarchical TSCOPF analysis has been carried out to obtain system reinforcement and operations. The developed hierarchical TSCOPF analysis is able to give the solutions which are stable against critical AC and DC faults. Time-domain simulation results with these AC and DC faults have been explained to understand the transient behaviors of the mixed AC / multi-terminal VSC HVDC system with the wind power plants.

The influences of the transient stability constraints on the reinforcement and fuel costs have been investigated. Firstly, the required multi-terminal VSC HVDC system reinforcement capacity is increased when the transient stability constraints are considered. Regarding the fuel costs, different influences of the transient stability constraints have been observed depending on the wind power output conditions. When the wind power output is sufficient to supply the nearby load consumption, the rest of the wind power is transmitted towards the large demand area. Since the VSC HVDC reinforcement, control system, and parameters are designed for this wind power transmission scenario, the fuel cost increments in TSCOPF analysis compared to the costs in SSSC-OPF analysis are relatively low when a sufficient amount of wind power is produced. On the contrary, substantial fuel cost increments have been calculated by TSCOPF analysis in other conditions. In order to relieve these fuel cost increments, an improved DC voltage control strategy is required. Instead of controlling VSC converters, the temporary disconnection of the multi-terminal VSC HVDC system is also possible.

Future works

Firstly, the utilizations of MTDC systems with different control strategies are necessary. In this dissertation, the most widely adopted conventional vector current control is utilized as the control strategy of VSC HVDC system. On top of that, DC voltage droop controls with voltage margins are used for some VSC converters. However, different results can be obtained if other improved control methods of MTDC systems are applied in the analysis. In particular, an improved DC voltage control method is also necessary to relieve the fuel cost increments in TSCOPF analysis explained in Chapter 5.

The second future work is the analysis with optimized control system parameters. The control system parameters are determined by trial and error approaches. Although this method is still acceptable when the transmission system operator is aware of effective control system parameters, theoretical background and improved dynamic behaviors of MTDC systems can be achieved by the optimization of control system parameters. General applications of the proposed method in other power system models with optimized control system parameters are also expected.

The works related to wind power plant models are also required. In this dissertation, wind power plants are modeled as simple static aggregated loads. On the other hand, it is worth considering the dynamic behaviors of different popular wind turbine types such as doubly-fed induction generator (DFIG), permanent magnet synchronous generator (PMSG), and so on. By considering the dynamic behaviors and the control systems of these wind power plants, reduced investment and fuel cost results are assumed to be obtained.

Another work regarding wind power plants is the consideration of wind power output suppression. Since wind power hosting capacities have been investigated in this dissertation, the suppression of wind power output is not allowed except the post-fault N-1 criterion feasibility analysis. If the wind power output suppression is allowed, different economic benefit analysis and business model of MTDC systems can be developed.

The next topic is relevant to the modeling of VSC HVDC system. HVDC systems with MMC technology are attracting much attention for large-scale high voltage-level HVDC implementations recently. The most distinctive point of MMC HVDC systems compared to conventional two or three-level-based VSC HVDC systems is the operations of sub-modules. However, this work should be carried out carefully since the representation of all MMC sub-module behaviors requires high computational burden.

The introductions of additional energy storage systems can be considered to utilize more wind energy. In Chapter 4, 9+9GW of wind power hosting capacity has been calculated. This hosting capacity is limited by the constraint of thermal power plants' lower active power production limits. These minimum active power production constraints are violated when more than 9+9GW wind farms are installed in cases of spring and autumn low-load conditions with rated wind power output. This can be overcome by additional energy storage systems. Different economic benefit analysis integrating these storage facilities will be necessary in these scenarios.

The scenario considering the reinforcements of both AC and VSC HVDC transmission is needed to be discussed. In Chapter 5 considering the transient stability constraints, the wind power hosting capacity is constrained by the transient voltage stability issue. Additional AC transmission

lines are necessary to solve this problem. In such case, the economic benefit analysis covering both AC and VSC HVDC transmission systems should also be developed.

The analysis considering not only the economic aspects, but environmental issues should be discussed. Since only the fuel costs of the thermal power plants are taken into account in the objective functions of the OPF analysis, the active power productions of coal-fired power plants with cheap fuel cost coefficients are relatively higher than other types of thermal power plants, which may not be desirable from the environmental viewpoint. In this context, other analysis models considering both economic and environmental aspects are necessary.

The last future work is the comparison between multi-terminal and point-to-point VSC HVDC systems with the transient stability constraints. The concept of flexible multi-terminal VSC HVDC operation has been suggested in this dissertation. However, this requires the installations of bidirectional hybrid DC CBs at the both ends of every DC transmission line to produce artificial zero DC current if a DC fault occurs. This yields additional investment costs to configure a multi-terminal topology. On the contrary, even though the operation flexibilities of VSC HVDC systems are reduced in cases of point-to-point configurations, a DC fault in a point-to-point VSC HVDC system can be cleared without expensive hybrid DC CBs by the loss of the entire faulted point-to-point VSC HVDC system. Hence, the economic benefit comparison between point-to-point and multi-terminal configurations considering transient stability constraints is worth to be investigated. In this context, the economic benefit comparison among different multi-terminal configuration considering the transient stability constraints is also necessary. Especially, the implementations of the three-terminal topologies in Chapter 4 without using DC CBs are also worth analyzing. In such cases, several three-terminal topologies without DC CBs may be evaluated to be more economical than four-terminal configurations using DC CBs.

Reference

[1] Target & Roadmap for Japanese Wind Power, Japan Wind Power Association," July, 2016

[2] D. Jovcic and K. Ahmed, *High voltage direct current transmission: converters, systems and DC grids*, John Wiley & Sons, 2015

[3] D. Van Hertem, O. Gomis-Bellmunt, and J. Liang, *HVDC grids For Offshore and Supergrid of the Future*, John Wiley & Sons, 2016

[4] A. Raza, X. Dianguo, S. Xunwen, L. Weixing, and B. W. Williams, "A novel multiterminal VSC-HVdc transmission topology for offshore wind farms" *IEEE Trans. on Industry Applications*, vol. 53, no. 2, pp. 1316-1325, Nov. 2016.

[5] W. Leterme, P. Tielens, S. De Boeck, and D. Van Hertem, "Overview of grounding and configuration options for meshed HVDC grids", *IEEE Trans. Power Delivery*, vol. 29, no. 6, pp.2467-2475, Dec. 2014.

[6] A. Lotfjou, Y. Fu, and M. Shahidehpour, "Hybrid AC/DC Transmission Expansion Planning," *IEEE Trans. Power Delivery*, vol. 27, no. 3, pp. 1620-1628, May. 2012.

[7] A. H. Deminguez, L. H. Macedo, A. H. Escobar, and R. Romero, "Multistage Security-Constrained HVAC/HVDC Transmission Expansion Planning With a Reduced Search Space," *IEEE Trans. Power Systems*, vol. 32, no. 6, pp. 4805-4817, Feb. 2017.

[8] V. L. M. Escobar, L. R. A. Romero, Z. A. H. Escobar, and R. R. A. Gallego, "Long term transmission expansion planning considering generation-demand scenarios and HVDC lines," in *2016 IEEE PES T&D-LA*, Morelia, Mexico, 2016, pp. 1-6.

[9] A. H. Dominguez, A. H. E. Zuluaga, L. H. Macedo, and R. Romero, "Transmission network expansion planning considering HVAC/HVDC lines and technical losses," in *2016 IEEE PES T&D-LA*, Morelia, Mexico, 2016, pp. 1-6.

[10] O. A. Mousavi, C. Y. Evrenosoglu, and M. Z. Bockarjova, "Optimal location and sizing of HVDC converters for same-tower AC-DC overhead lines," in *2015 IEEE Eindhoven PowerTech*, Eindhoven, Netherlands, 2015, pp. 1-6.

[11] H. D. Mojarrad, H. Rastegar, and G. B. Gharehpetian, "Probabilistic multi-objective HVDC/AC transmission expansion planning considering distant wind/solar farms," *IET Science, Measurement & Technology*, vol. 10, no. 2, pp.140-149, Mar. 2016.

[12] S. S. Torbaghan, M. Gibescu, B. G. Rawn, and M. V. D. Meijden, "A Market-Based Transmission Planning for HVDC Grid–Case Study of the North Sea," *IEEE Trans. Power Systems*, vol. 30, no. 2, pp. 784-794, Jul. 2014.

[13] H. Ergun, B. Rawn, R. Belmans, and D. V. Hertem, "Stepwise Investment Plan Optimization for Large Scale and Multi-Zonal Transmission System Expansion," *IEEE Trans. Power Systems*, vol. 31, no. 4, pp. 2726-2739, Oct. 2015.

[14] A. Elahidoost, L. Furieri, E. Tedeschi, and M. Kamgarpour, "Optimizing HVDC Grid Expansion and Control for Enhancing DC Stability," in *2018 PSCC*, Dublin, Ireland, 2018, pp. 1-7.

[15] A. A. V. D. Meer, M. Ndreko, J. A. Bos, M. Gibescu, M. A. M. M. V. D. Meijden, and W. L. Kling, "Stability assessment of VSC-HVDC connected large-scale offshore wind power: A North-Sea region case study," in *2015 IEEE Eindhoven PowerTech*, Eindhoven,

Netherlands, 2015, pp. 1-6.
[16] A. Fuchs and M. Morari, “Placement of HVDC links for power grid stabilization during transients,” in *2013 IEEE Grenoble Conference*, Grenoble, France, 2013, pp. 1-6
[17] S. Q. Bu, W. Du, H. F. Wang, Y. Liu, and X. Liu, “Investigation on economic and reliable operation of meshed MTDC/AC grid as impacted by offshore wind farms,” *IEEE Trans. Power Systems*, vol. 32, no. 5, pp. 3901-3911, Sep. 2017.
[18] S. Kim, A. Yokoyama, T. Takano, H. Hashimoto, and Y. Izui, “Economic benefit evaluation of multi-terminal VSC HVDC systems with wind farms based on security-constrained optimal power flow,” in *the 12th IEEE PES PowerTech*, Manchester, UK, 2017, pp. 1-6.
[19] S. Kim, A. Yokoyama, T. Takano, Y. Izui, and H. Hashimoto, “Economic benefits comparison between point-to-point and multi-terminal VSC HVDC systems with large-scale wind farms,” *IEEJ Trans. Electrical and Electronic Engineering*, vol. 13, no. 11, pp. 1595-1602, May. 2018.
[20] V. Saplamidis, R. Wiget, and G. Andersson, “Security constrained optimal power flow for mixed AC and multi-terminal HVDC grids,” in *2015 IEEE Eindhoven PowerTech*, Eindhoven, Netherlands, 2015, pp. 1-6.
[21] J. Cao, W. Du, and H. Wang, “An improved corrective security constrained OPF for meshed AC/DC grids with multi-terminal VSC-HVDC,” *IEEE Trans. Power Systems*, vol. 31, no. 1, pp. 485-495, Jan. 2016.
[22] Y. Zhang, K. Gao, Z. Han, P. Yu, Y. Chen, and J. Ma, “Multi-objectives OPF of AC-DC systems considering VSC-HVDC integration,” in 2016 *IEEE PES APPEEC*, Xian, China, 2016, pp. 929-933.
[23] W. Feng, L. A. Tuan, L. B. Tjernberg, A. Mannikoff, and A. Bergman, “A new approach for benefit evaluation of multiterminal VSC–HVDC using a proposed mixed AC/DC optimal power flow,” *IEEE Trans. Power Delivery*, vol. 29, no. 1, pp. 432-443, Feb. 2014.
[24] A. Nikoobakht, J. Aghaei, T. Niknam, V. Vahidinasab, H. Farahmand, and M. Korpas, “Towards robust OPF solution strategy for the future AC/DC grids: case of VSC-HVDC-connected offshore wind farms,” *IET Renewable Power Generation*, vol. 12, no. 6, pp.691-701, Apr. 2018.
[25] 電力系統過渡解析論. オーム社, 1984. (in Japanese)
[26] P. Kundur, *Power system stability and control*. New York: McGraw-hill, 1994.
[27] Grid-interconnection Code JEAC 9701-2016, pp. 333-334 and pp. 177-178 (in Japanese)
[28] H. Saad, J. Peralta, S. Dennetiere, J. Mahseredjian, J. Jatskevich, J.A. Martinez, A. Davoudi, M. Saeedifard, V. Sood, X. Wang, J. Cano, and A. Mehrizi-Sani, “Dynamic averaged and simplified models for MMC-based HVDC transmission systems”, *IEEE Trans. Power Delivery*, vol. 28, no. 3, pp.1723-1730, Jul. 2013.
[29] W. Wang and M. Barnes, “Power flow algorithms for multi-terminal VSC-HVDC with droop control”, *IEEE Trans. Power Systems*, vol. 29, no. 4, pp.1721-1730, Jul. 2014.
[30] C. Dierckxsens, K. Srivastava, M. Reza, S. Cole, J. Beerten, and R. Belmans, “A distributed DC voltage control method for VSC MTDC systems,” *Electric Power Systems Research*, vol. 82, no. 1, pp. 54–58, Jan. 2012.

[31] T. M. Haileselassie and K. Uhlen, “Impact of DC line voltage drops on power flow of MTDC using droop control”, *IEEE Trans. Power Systems*, vol. 27, no. 3, pp.1441-1449, Aug. 2012.

[32] O. Gomis-Bellmunt, J. Liang, J. Ekanayake, and N. Jenkins, “Voltage-Current characteristics of multiterminal HVDC-VSC for offshore wind farms,” *Electric Power Systems Research*, vol. 81, no. 2, pp. 440-450, Feb. 2011.

[33] ENTSO-E Draft Network Code on High Voltage Direct Current Connections and DC-connected Power Part Modules, Apr 2014.

[34] M. Callavik, A. Blomberg, J. Häfner, and B. Jacobson, “The hybrid HVDC breaker”, *ABB Grid Systems Technical Paper 361*, pp. 143-152, 2012.

[35] J. Yang, J. E. Fletcher, and J. O’Reilly, “Short-circuit and ground fault analyses and location in VSC-based DC network cables”, *IEEE Trans. Industrial Electronics*, vol. 59, no. 10, pp. 3827-3837, Jul. 2012.

[36] G. Tang, Z. Xu, and Y. Zhou, “Impacts of three MMC-HVDC configurations on AC system stability under DC line faults”, *IEEE Trans. Power Systems*, vol. 29, no. 6, pp. 3030-3040, Apr. 2014.

[37] “IEEJ EAST 10–machine System Model, Web page : http://www.iee.jp/pes/?page_id=496,” The Institute of Electrical Engineers in Japan, 2000.

[38] O. Ziaee and F. F. Choobineh, “Optimal location-allocation of TCSC devices on a transmission network,” *IEEE Trans. Power Systems*, vol. 32, no. 1, pp. 94-102, Apr. 2017.

List of Publications

Transaction / Journal Papers

[1] Sangwon Kim, Akihiko Yokoyama, Tomihiro Takano, Yoshio Izui, Hiroyuki Hashimoto, "Economic Benefits Comparison between Point-to-Point and Multi-Terminal VSC HVDC Systems with Large-Scale Wind Farms", 電気学会共通英文論文誌(IEEJ Transactions on Electrical and Electronic Engineering), Vol. 13, No. 11, pp. 1595-1602, Nov. 2018

[2] Sangwon Kim, Akihiko Yokoyama, Yusuke Takaguchi, Tomihiro Takano, Kazuyuki Mori, Yoshio Izui,"Small–Signal Stability Constrained Optimal Power Flow Analysis on Multi–Terminal VSC–HVDC Systems with Large–Scale Wind Farms", 電気学会共通英文論文誌(IEEJ Transactions on Electrical and Electronic Engineering), Vol. 14, No. 7, pp. 1033-1046, Jul. 2019

[3] Sangwon Kim, Akihiko Yokoyama, Yusuke Takaguchi, Tomihiro Takano, Kazuyuki Mori, Yoshio Izui, "A Novel Economic Analysis on Multi-Terminal VSC HVDC Systems with Wind Farms by Hierarchical Small-Signal Stability Constrained OPF", 電気学会共通英文論文誌(IEEJ Transactions on Electrical and Electronic Engineering), Vol. 15, No. 4, Apr. 2020 (*To be published*)

International Conference Papers

[4] (*Awarded*) Sangwon Kim, Akihiko Yokoyama, Tomihiro Takano, Hiroyuki Hashimoto, Yoshio Izui, "Economic Benefit Evaluation of Multi-Terminal VSC-HVDC Systems with Wind Farms based on Security-Constrained Optimal Power Flow", 12th IEEE PES PowerTech Conference, Manchester, pp.1-6, Jun. 2017

[5] Sangwon Kim, Akihiko Yokoyama, Tomihiro Takano, Hiroyuki Hashimoto, Yoshio Izui, "Small-Signal Stability Constrained Optimal Power Flow Analysis for Mixed AC and Multi-Terminal Voltage-Source Converter HVDC Systems", International Conference on Electrical Engineering 2017, Weihai, pp. 1-6, Jul. 2017

[6] Sangwon Kim, Akihiko Yokoyama, Tomihiro Takano, Yoshio Izui, Kazuyuki Mori, "Economic Benefit Analysis on Multi-Terminal VSC-HVDC System with Large-Scale Wind Farms based on Multi-Period Optimal Power Flow", International Conference on Electrical Engineering 2018, Seoul, pp. 1-6, Jun. 2018

[7] Sangwon Kim, Akihiko Yokoyama, Yusuke Takaguchi, Tomihiro Takano, Kazuyuki Mori, Yoshio Izui, “Economic Analysis on Multi-Terminal VSC HVDC Systems with Wind Farms based on Hierarchical Optimal Power Flow with Stability Constraint”, 13th IEEE PES PowerTech Conference, Milan, pp. 1-6, Jun. 2019

[8] Sangwon Kim, Akihiko Yokoyama, Yusuke Takaguchi, Tomihiro Takano, Kazuyuki Mori, Yoshio Izui, “Optimal Power Flow Analysis on Mixed AC / Multi-Terminal VSC HVDC System with Wind Farms with Stability Constraints”, International Conference on Electrical Engineering 2019, Hong Kong, pp. 1-6, Jul. 2019

Domestic Conference Papers / Symposiums

[9] (*Awarded*) Sangwon Kim, Akihiko Yokoyama, Tomihiro Takano, Yoshio Izui, Hiroyuki Hashimoto, “Economic Evaluations on Multi-Terminal VSC HVDC Systems based on Small-Signal Stability Constrained Optimal Power Flow Analysis”, International Workshop on Power Engineering in Remote Islands (IWPI2018), Okinawa, pp. 1-6, Feb. 2018

[10] Sangwon Kim, Akihiko Yokoyama, Tomihiro Takano, Yoshio Izui, Kazuyuki Mori, “Economic Benefit Analysis on Multi-Terminal VSC-HVDC System with Large-Scale Wind Farms based on Multi-Period Optimal Power Flow”, IEEJ P&ES-IEEE PES Thailand Joint Symposium Thailand, Krabi, pp. 1-6, Mar. 2018

[11] (*Awarded*) Sangwon Kim, Akihiko Yokoyama, Tomihiro Takano, Yoshio Izui, Kazuyuki Mori, “Design and Economic Load Dispatch of a Mixed AC / Multi-Terminal VSC HVDC System with Wind Farms by Hierarchical Optimal Power Flow”, The 2018 Annual Meeting of The Institute of Electrical Engineers of Japan （平成 30 年電気学会全国大会）, Fukuoka, pp. 1-2, Mar. 2018

[12] Sangwon Kim, Akihiko Yokoyama, Tomihiro Takano, Yoshio Izui, Kazuyuki Mori, “A Method for Capacity Determination of Multi−Terminal VSC−HVDC System with Large−Scale Wind Farms based on Multi−Period Small−Signal Stability Constrained Optimal Power Flow”, The 2018 Annual Conference of Power & Energy Society IEE of Japan（平成 30 年電気学会電力・エネルギー部門大会）, Tokushima, pp. 1-5, Sep. 2018

[13] Sangwon Kim, Akihiko Yokoyama, Tomihiro Takano, Kazuyuki Mori, Yusuke Takaguchi, “Transient Stability Constrained Optimal Power Flow Analysis in Mixed AC / Multi−Terminal VSC HVDC System”, The Papers of Joint Technical Meeting on Power Engineering and Power Systems Engineering IEE Japan （平成 30 年電力技術/電力系統技術合同研究会）, Nagoya, pp. 1-6, Sep. 2018

[14] Sangwon Kim, Akihiko Yokoyama, Yusuke Takaguchi, Tomihiro Takano, Kazuyuki Mori, Yoshio Izui, “A Novel Operation Method and Economic Analysis of Multi-Terminal VSC-HVDC System with Wind Farms by Optimal Power Flow”, The 2019 Annual Meeting of The Institute of Electrical Engineers of Japan（平成 31 年電気学会全国大会）, Sapporo, pp. 1-2, Mar. 2019 (in Japanese)
（金　相源, 横山　明彦, 高口　雄介, 高野　富裕, 森　一之, 泉井　良夫, “最適潮流計算を用いた風力連系多端子自励式直流送電システムの運用とその経済性評価”, 平成 31 年電気学会全国大会, 札幌, 2019 年 3 月）

[15] Sangwon Kim, Akihiko Yokoyama, Yusuke Takaguchi, Tomihiro Takano, Kazuyuki Mori, Yoshio Izui, “Optimal Power Flow Analysis on Mixed AC / Multi-Terminal VSC HVDC System with DC Grid Transient Stability”, The 2019 Annual Conference of Power & Energy Society IEE of Japan （令和元年電気学会電力・エネルギー部門大会）, Hiroshima, pp. 1-6, Sep. 2019

[16] Sangwon Kim, Akihiko Yokoyama, Yusuke Takaguchi, Tomihiro Takano, Kazuyuki Mori, Yoshio Izui, “Transient Stability Constrained Optimal Power Flow for Wind Power Transmission in a System with Multi-Terminal VSC HVDC”, The Papers of Joint Technical Meeting on Power Engineering and Power Systems Engineering IEE Japan（令和元年電力技術/電力系統技術合同研究会）, Okinawa, pp. 1-6, Sep. 2019

Appendix

A. SYSTEM CONVERGENCE CALCULATION

In Runge-Kutta method, the state variables at the *n+1*th time step are updated by differential equations using the state variables and other variables at the *n*th time step. The values of the variables except the state variables are calculated based on algebraic equations of a power system model using the state variables at the *n+1*th time step.

The system AC bus voltage values at the *n+1*th time step can be obtained using this principle. If the system admittance matrix *Y* is known, the system AC bus voltage values at the *n+1*th time step can be calculated using the nodal equations in (A.1), which can be utilized for updating the state variables at the next *n+2*th time step.

In case of the systems with a multi-terminal VSC HVDC system, since the current injections by the multi-terminal VSC HVDC system are modeled as the state variables, those values are updated and known at the *n+1*th time step. Therefore, the AC bus voltage values at the *n+1*th time step can also be obtained using the simple algebraic equation in (A.1). Regarding the AC load characteristics, this principle can also be applied if *Y* is fixed during the entire period of the time-domain simulation.

$$I_{AC} = Y_{AC} V_{AC} \tag{A.1}$$

Y_{AC} Admittance matrix in AC grid
V_{AC} Node voltage in AC grid
I_{AC} Current injection in AC grid

However, the system admittance matrix *Y* is not fixed with the consideration of the wind power plant models. Hence, the principle cannot be used for the AC bus voltage calculation in case of wind power plants installation in AC grid. In this dissertation, the system convergence calculation is adopted to calculate AC bus voltages during the time-domain simulation.

First of all, instead of obtaining the exact values of AC bus voltages, the estimated values of AC bus voltages V_{est} at the *n+1*th time step are determined. The voltage values at the previous *n*th time step can be used as the initial estimated voltage values.

As a result, the estimated system admittance matrix Y_{est} can be obtained. Here, Y_{est} is composed of three components as (A.2): the admittances of AC network transmission lines, loads with constant impedance characteristics, wind power plant models. To be specific, the admittance components of AC transmission lines and loads are fixed. The estimated admittances of wind power plant models can be obtained as (A.3).

$$Y_{est} = Y_{network} + Y_{load} + Y_{est,wind} \tag{A.2}$$

$$Y_{est,wind} = \frac{P_{wind}}{\left|V_{est,wind}\right|^2} \tag{A.3}$$

Since the internal voltage values of generators are handled as the state variables, those at the n+1th time step are already known. The current injection values of generators into AC grid can be estimated based on the estimated admittance, voltage values and the internal voltage values. It should be noted that all current injection values are represented in the synchronously rotating DQ axes. Equations (A.4) and (A.5) correspond to the nodal equations which can also be expressed as the reduction form with respect to generator buses in (A.6). The relation between generators' voltage and current is modeled as (A.7). By manipulating all these equations, it is summed up as (A.8) which reflects all generators and AC grid nodal equations with respect to generator buses. As a consequence, the estimated values of generators' current injections can be calculated using (A.9). It should be noted in (A.9) that i_s are state variables of the multi-terminal VSC HVDC system, those values are not needed to be estimated.

$$Y_{GG}V_G + Y_{Gs}v_s = I_G \tag{A.4}$$

$$Y_{sG}V_G + Y_{ss}v_{ss} = i_s \tag{A.5}$$

$$I_G = (Y_{GG} - Y_{Gs}Y_{ss}^{-1}Y_{sG})V_G + Y_{Gs}Y_{ss}^{-1}i_s \tag{A.6}$$

$$V_G = E_G - Z^* I_G \tag{A.7}$$

$$I_G = Y_G E_G + K_s i_s \tag{A.8}$$

$$I_{G,esi} = (Y_{GG,esi} - Y_{Gs,esi}Y_{ss,esi}^{-1}Y_{sG,esi})V_{G,esi} + Y_{Gs,esi}Y_{ss,esi}^{-1}i_s \tag{A.9}$$

where

G	Generator
s	PCC bus of multi-terminal VSC HVDC system
V_G	Generator bus voltage
v_s	PCC bus voltage of multi-terminal VSC HVDC system
I_G	Current injection by generators
i_s	Current injection by multi-terminal VSC HVDC system

$$Z^* = \begin{bmatrix} R + (X_d^{"} - X_q^{"})\sin\delta\cos\delta & -(X_d^{"}\cos^2\delta + X_q^{"}\sin^2\delta) \\ X_d^{"}\sin^2\delta + X_q^{"}\cos^2\delta & R - (X_d^{"} - X_q^{"})\sin\delta\cos\delta \end{bmatrix} \tag{A.10}$$

$$Y_G = (I + Y^* Z^*)^{-1} Y^* \tag{A.11}$$

$$K_s = (I + Y^* Z^*)^{-1} Y_{Gs} Y_{ss}^{-1} \tag{A.12}$$

$$Y^* = Y_{GG} - Y_{Gs}Y_{ss}^{-1}Y_{sG} \tag{A.13}$$

As the next step in (A.14), AC bus voltage can be re-calculated based on the estimated admittance matrix and the current injection values. In (A.14), it is assumed that there is no current injection into AC grid except generators and a multi-terminal VSC HVDC system. (A.14) can also be simplified as (A.15).

$$\begin{bmatrix} V_{G,check} \\ v_{s,check} \\ V_{L,check} \end{bmatrix} = \begin{bmatrix} Y_{GG,est} & Y_{Gs,est} & Y_{GL,est} \\ Y_{sG,est} & Y_{ss,est} & Y_{sL,est} \\ Y_{LG,est} & Y_{Ls,est} & Y_{LL,est} \end{bmatrix}^{-1} \begin{bmatrix} I_{G,est} \\ i_s \\ 0 \end{bmatrix} \quad \text{(A.14)}$$

$$V_{check} = Y_{est}^{-1} I_{est} \quad \text{(A.15)}$$

Finally, V_{est} and V_{check} are compared to check the feasibility of V_{est}. If the difference of those values $| V_{check} - V_{est} |$ are small enough, it is inferred that V_{est} satisfies all system behaviors from (A.4) to (A.8). Therefore, V_{est} can be adopted as the AC bus voltage values at the $n+1$th time step. If the difference is not negligible, V_{est} is adjusted to be $V_{est,new}$ as (A.16) and the same procedure is repeated until the feasible V_{est} is found. In this dissertation, V_{est} is adopted if the difference $| V_{check} - V_{est} |$ of all AC bus voltages are less than 0.001 *p.u.*. The adjustment ratio α is set to be 0.3 *p.u.*.

$$V_{est,new} = \alpha \times (V_{check} - V_{est}) \quad \text{(A.16)}$$

The entire process of the system convergence calculation is plotted in Fig. A.1.

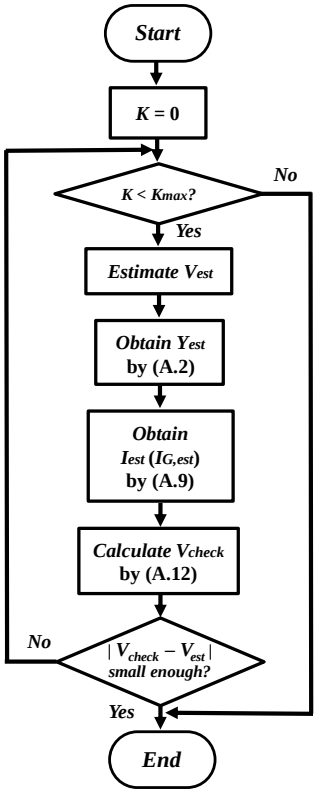

Fig. A.1. Algorithm of system convergence calculation

In cases of sudden AC grid changes and non-linear behaviors, the proper V_{est} values are often not found during the iterative calculation until K_{max}. In such cases, the operation point is classified as unstable and the OPF solution is not adopted.

B. SYSTEM MODEL LINEARIZATION

In order for the small-signal stability analysis, the eigenvalues of the system at an operating point are calculated. To this end, the integrated linear model which consists of synchronous generators, AC system, wind power plants, and a multi-terminal VSC-HVDC system is calculated.

x_g, x_{vsc}, and $x_{IDC,line}$ represent the state variables for each generator, VSC converter, and DC line respectively. x_{total} corresponds to the entire state variable vector. For instance, x_{total} is composed of 131 state variables when a system model consists of ten generators and four-terminal VSC-HVDC system model with three DC lines.

The linearized synchronous generator model is represented in (B.1) – (B.3). Equation (B.4) is the linearized AC network equation from (B.12). The linearized model of the multi-terminal VSC-HVDC system is obtained in (B.5) – (B.8). The integrated model of the linearized mixed AC / multi-terminal VSC-HVDC system with wind power plants corresponds to (B.9) and (B.10).

The eigenvalues of A_{total} matrix at the operating point are calculated for the small-signal stability analysis of the mixed AC / multi-terminal VSC-HVDC system. The notation '•' on the state variables represents the differentiation operator with respect to the time domain.

$$A_{ac}\Delta\dot{x}_g + B_{ac}\Delta V_G = C_{ac}\Delta x_g \tag{B.1}$$

$$\Delta I_G = Y_G\Delta V_G = D_{ac}\Delta x_g \tag{B.2}$$

$$\Delta x_g = [\Delta i_d\ \Delta i_q\ \Delta i_{fd}\ \Delta i_{kd}\ \Delta i_{fq}\ \Delta i_{kq}\ \Delta\delta\ \Delta\omega\ \Delta P_m\ \Delta v_f]^T \tag{B.3}$$

$$\begin{bmatrix}\Delta V_G\\ \Delta v_s\\ \Delta V_P\end{bmatrix} = \begin{bmatrix}Z_{GG} & Z_{GS} & Z_{GP}\\ Z_{SG} & Z_{SS} & Z_{SP}\\ Z_{PG} & Z_{PS} & Z_{PP}\end{bmatrix}\begin{bmatrix}\Delta I_G\\ \Delta i_s\\ \Delta I_P\end{bmatrix} \tag{B.4}$$

$$\Delta\dot{x}_{vsc} = A_{vsc1}\Delta x_{vsc} + A_{vsc2}\Delta v_s + A_{vsc3}\Delta I_{DC} \tag{B.5}$$

$$\Delta x_{vsc} = [\Delta i_{sd}\ \Delta i_{sq}\ \Delta V_{DC}\ \Delta z_1\ \Delta z_2\ \Delta z_3\ \Delta z_4]^T \tag{B.6}$$

$$\Delta\dot{x}_{I_{DC,line}} = L_{DC}^{-1}\Delta x_{vsc} - L_{DC}^{-1}R_{DC}\Delta x_{I_{DC,line}} \tag{B.7}$$

$$\Delta x_{I_{DC,line}} = [\Delta I_{DC,line}]^T \tag{B.8}$$

$$\begin{bmatrix}\Delta\dot{x}_g\\ \Delta\dot{x}_{vsc}\\ \Delta\dot{x}_{I_{DC,line}}\end{bmatrix} = \begin{bmatrix}A_{11} & A_{12} & A_{13}\\ A_{21} & A_{22} & A_{23}\\ A_{31} & A_{32} & A_{33}\end{bmatrix}\begin{bmatrix}\Delta x_g\\ \Delta x_{vsc}\\ \Delta x_{I_{DC,line}}\end{bmatrix} \tag{B.9}$$

$$\Delta\dot{x}_{total} = A_{total}\Delta x_{total} \tag{B.10}$$

where

$$I_{AC} = Y_{AC}V_{AC} \text{ or } V_{AC} = Y_{AC}^{-1}I_{AC} = Z_{AC}I_{AC}$$

$$\begin{bmatrix}V_G\\ v_s\\ V_P\\ V_r\end{bmatrix} = Z_{AC}\begin{bmatrix}I_G\\ i_s\\ I_P\\ 0\end{bmatrix} \tag{B.11}$$

$$\begin{bmatrix}V_G\\ v_s\\ V_P\end{bmatrix} = \begin{bmatrix}Z_{GG} & Z_{GS} & Z_{GP}\\ Z_{SG} & Z_{SS} & Z_{SP}\\ Z_{PG} & Z_{PS} & Z_{PP}\end{bmatrix}\begin{bmatrix}I_G\\ i_s\\ I_P\end{bmatrix} \tag{B.12}$$

$$A_{ac}=\begin{bmatrix} x_d & 0 & -x_{md} & -x_{md} & 0 & 0 & 0 & 0 & 0 & 0 \\ 0 & x_q & 0 & 0 & -x_{mq} & -x_{mq} & 0 & 0 & 0 & 0 \\ -x_{md} & 0 & x_{fd} & x_{md} & 0 & 0 & 0 & 0 & 0 & 0 \\ -x_{md} & 0 & x_{md} & x_{kd} & 0 & 0 & 0 & 0 & 0 & 0 \\ 0 & -x_{mq} & 0 & 0 & x_{fq} & x_{mq} & 0 & 0 & 0 & 0 \\ 0 & -x_{mq} & 0 & 0 & x_{mq} & x_{kq} & 0 & 0 & 0 & 0 \\ 0 & 0 & 0 & 0 & 0 & 0 & 1 & 0 & 0 & 0 \\ 0 & 0 & 0 & 0 & 0 & 0 & 0 & 2H & 0 & 0 \\ 0 & 0 & 0 & 0 & 0 & 0 & 0 & 0 & T_G & 0 \\ 0 & 0 & 0 & 0 & 0 & 0 & 0 & 0 & 0 & T_A \end{bmatrix} \tag{B.13}$$

$$B_{ac}=\begin{bmatrix} \sin\delta & -\cos\delta \\ \cos\delta & \sin\delta \\ 0_{7X1} & 0_{7X1} \\ \frac{R_{fd}}{x_{md}}\frac{K_A V_D}{v_t} & \frac{R_{fd}}{x_{md}}\frac{K_A V_Q}{v_t} \end{bmatrix} \tag{B.14}$$

$$C_{ac}=\begin{bmatrix} -R & x_q & 0 & 0 & -x_{mq} & -x_{mq} & -v_q & -\phi_q & 0 & 0 \\ -x_d & -R & x_{md} & x_{md} & 0 & 0 & v_d & \phi_d & 0 & 0 \\ 0 & 0 & -R_{fd} & 0 & 0 & 0 & 0 & 0 & 0 & 1 \\ 0 & 0 & 0 & -R_{kd} & 0 & 0 & 0 & 0 & 0 & 0 \\ 0 & 0 & 0 & 0 & -R_{fq} & 0 & 0 & 0 & 0 & 0 \\ 0 & 0 & 0 & 0 & 0 & -R_{kq} & 0 & 0 & 0 & 0 \\ 0 & 0 & 0 & 0 & 0 & 0 & 0 & 1 & 0 & 0 \\ \phi_q + x_d i_q & -\phi_d - x_q i_d & -x_{md} i_q & -x_{md} i_q & x_{mq} i_d & x_{mq} i_d & 0 & -T_m + D & 1 & 0 \\ 0 & 0 & 0 & 0 & 0 & 0 & 0 & -K_G & -1 & 0 \\ 0 & 0 & 0 & 0 & 0 & 0 & 0 & 0 & 0 & -1 \end{bmatrix} \tag{B.15}$$

$$D_{ac}=\begin{bmatrix} \sin\delta & \cos\delta & 0_{1X4} & -I_Q & 0_{1X3} \\ -\cos\delta & \sin\delta & 0_{1X4} & I_D & 0_{1X3} \end{bmatrix} \tag{B.16}$$

A_{ac}, B_{ac}, C_{ac}, D_{ac} Linearized model of synchronous generator with Park model in synchronously rotating DQ frame

$I_G = I_D + jI_Q$ Current injection at generator buses

$0_{m\times n}$ zero matrix with m rows and n columns

$$P_P = P_{P0}\left(\frac{V_P}{V_{P0}}\right)^m$$
$$Q_P = Q_{P0}\left(\frac{V_P}{V_{P0}}\right)^n \tag{B.17}$$

for wind power plants (constant power loads), $m = n = 0$

$$G_{RR}=\frac{P_{P0}}{V_{P0}^2}\left((m-2)\frac{V_{R0}^2}{V_{P0}^2}+1\right)+\frac{Q_{P0}}{V_{P0}^2}\left((n-2)\frac{V_{R0}V_{I0}}{V_{P0}^2}\right) \qquad B_{IR}=\frac{Q_{P0}}{V_{P0}^2}\left((n-2)\frac{V_{R0}^2}{V_{P0}^2}+1\right)-\frac{P_{P0}}{V_{P0}^2}\left((m-2)\frac{V_{R0}V_{I0}}{V_{P0}^2}\right)$$

$$B_{RI}=\frac{Q_{P0}}{V_{P0}^2}\left((n-2)\frac{V_{I0}^2}{V_{P0}^2}+1\right)+\frac{P_{P0}}{V_{P0}^2}\left((m-2)\frac{V_{R0}V_{I0}}{V_{P0}^2}\right) \qquad G_{II}=\frac{P_{P0}}{V_{P0}^2}\left((m-2)\frac{V_{I0}^2}{V_{P0}^2}+1\right)-\frac{Q_{P0}}{V_{P0}^2}\left((n-2)\frac{V_{R0}V_{I0}}{V_{P0}^2}\right) \tag{B.18}$$

where $V_{P0} = V_{R0} + jV_{I0}$

$$A_{11}=A_{ac}^{-1}(C_{ac}-B_{ac}Z_{GG}D_{ac}-B_{ac}K_1Y_PZ_{PG}D_{ac}) \qquad A_{12}=A_{ac}^{-1}(-B_{ac}Z_{GS}-B_{ac}K_1Y_PZ_{PS}) \qquad A_{13}: \text{zero matrix}$$
$$A_{21}=A_{vsc2}(Z_{SG}D_{ac}+K_2Y_PZ_{PG}D_{ac}) \qquad A_{22}=A_{vsc1}+A_{vsc2}(Z_{SS}+K_2Y_PZ_{PS}) \qquad A_{23}=-A_{vsc3}W_{DC}^T \tag{B.19}$$

A_{31} : zero matrix $\quad A_{32} = L_{DC}^{-1} W_{DC} \quad A_{33} = -L_{DC}^{-1} R_{DC}$

where $K_1 = Z_{GP}(I - Y_P Z_{PP})^{-1}$, $K_2 = Z_{SP}(I - Y_P Z_{PP})^{-1}$

A_{vsc1} matrix

$$A_{vsc1} = \begin{bmatrix} -\frac{(R_c + k_{pi,i})}{L_c} - \frac{k_{pi,i}k_{p,p,i}v_{sdi}}{L_c} & -\frac{k_{pi,i}k_{p,p,i}v_{sqi}}{L_c} & 0 & \frac{1}{L_c} & 0 & \frac{k_{pi,i}}{L_c} & 0 \\ \frac{k_{pi,i}k_{p,q,i}v_{sqi}}{L_c} & -\frac{(R_c + k_{pi,i})}{L_c} - \frac{k_{pi,i}k_{p,q,i}v_{sdi}}{L_c} & 0 & 0 & \frac{1}{L_c} & 0 & -\frac{k_{pi,i}}{L_c} \\ \frac{(-v_{cdi} + k_{pi,i}i_{sdi} - \omega L_c i_{sqi})}{C_{DC}V_{DC,i}} + \frac{k_{pi,i}k_{p,p,i}i_{sdi}v_{sdi}}{C_{DC}V_{DC,i}} - \frac{k_{pi,i}k_{p,q,i}i_{sqi}v_{sqi}}{C_{DC}V_{DC,i}} & \frac{(-v_{cqi} + k_{pi,i}i_{sqi} + \omega L_c i_{sdi})}{C_{DC}V_{DC,i}} + \frac{k_{pi,i}k_{p,p,i}i_{sdi}v_{sqi}}{C_{DC}V_{DC,i}} + \frac{k_{pi,i}k_{p,q,i}i_{sqi}v_{sdi}}{C_{DC}V_{DC,i}} & \frac{(v_{cdi}i_{sdi} + v_{cqi}i_{sqi})}{C_{DC}V_{DC,i}^2} & \frac{-i_{sdi}}{C_{DC}V_{DC,i}} & \frac{-i_{sqi}}{C_{DC}V_{DC,i}} & \frac{-i_{sdi}k_{pi,i}}{C_{DC}V_{DC,i}} & \frac{i_{sqi}k_{pi,i}}{C_{DC}V_{DC,i}} \\ -k_{ii,i} - k_{ii,i}k_{p,p,i}v_{sdi} & -k_{ii,i}k_{p,p,i}v_{sqi} & 0 & 0 & 0 & k_{ii,i} & 0 \\ k_{ii,i}k_{p,q,i}v_{sqi} & -k_{ii,i} - k_{ii,i}k_{p,q,i}v_{sdi} & 0 & 0 & 0 & 0 & -k_{ii,i} \\ -k_{i,p,i}v_{sdi} & -k_{i,p,i}v_{sqi} & 0 & 0 & 0 & 0 & 0 \\ -k_{i,q,i}v_{sqi} & k_{i,q,i}v_{sdi} & 0 & 0 & 0 & 0 & 0 \end{bmatrix}$$

for $P_s - Q_s$ control mode of VSC i

$$A_{vsc1} = \begin{bmatrix} -\frac{(R_c + k_{pi,i})}{L_c} & 0 & \frac{k_{pi,i}k_{p,DC,i}}{L_c} & \frac{1}{L_c} & 0 & -\frac{k_{pi,i}}{L_c} & 0 \\ \frac{k_{pi,i}k_{p,q,i}v_{sqi}}{L_c} & -\frac{(R_c + k_{pi,i})}{L_c} - \frac{k_{pi,i}k_{p,q,i}v_{sdi}}{L_c} & 0 & 0 & \frac{1}{L_c} & 0 & -\frac{k_{pi,i}}{L_c} \\ \frac{(-v_{cdi} + k_{pi,i}i_{sdi} - \omega L_c i_{sqi})}{C_{DC}V_{DC,i}} - \frac{k_{pi,i}k_{p,q,i}i_{sqi}v_{sqi}}{C_{DC}V_{DC,i}} & \frac{(-v_{cqi} + k_{pi,i}i_{sqi} + \omega L_c i_{sdi})}{C_{DC}V_{DC,i}} + \frac{k_{pi,i}k_{p,q,i}i_{sqi}v_{sdi}}{C_{DC}V_{DC,i}} & \frac{(v_{cdi}i_{sdi} + v_{cqi}i_{sqi} - k_{p,dc,i}k_{pi,i}V_{DC,i}i_{sdi})}{C_{DC}V_{DC,i}^2} & \frac{-i_{sdi}}{C_{DC}V_{DC,i}} & \frac{-i_{sqi}}{C_{DC}V_{DC,i}} & \frac{i_{sdi}k_{pi,i}}{C_{DC}V_{DC,i}} & \frac{i_{sqi}k_{pi,i}}{C_{DC}V_{DC,i}} \\ -k_{ii,i} & 0 & k_{ii,i}k_{p,DC,i} & 0 & 0 & -k_{ii,i} & 0 \\ k_{ii,i}k_{p,q,i}v_{sqi} & -k_{ii,i} - k_{ii,i}k_{p,q,i}v_{sdi} & 0 & 0 & 0 & 0 & -k_{ii,i} \\ 0 & 0 & -k_{i,DC,i} & 0 & 0 & 0 & 0 \\ -k_{i,q,i}v_{sqi} & k_{i,q,i}v_{sdi} & 0 & 0 & 0 & 0 & 0 \end{bmatrix}$$

for $V_{DC} - Q_s$ control mode of VSC i

$$A_{vsc1} = \begin{bmatrix} -\frac{(R_c + k_{pi,i})}{L_c} - \frac{k_{pi,i}k_{p,p,i}v_{sdi}}{L_c} & -\frac{k_{pi,i}k_{p,p,i}v_{sqi}}{L_c} & 0 & \frac{1}{L_c} & 0 & \frac{k_{pi,i}}{L_c} & 0 \\ 0 & -\frac{(R_c + k_{pi,i})}{L_c} & 0 & 0 & \frac{1}{L_c} & 0 & \frac{k_{pi,i}}{L_c} \\ \frac{(-v_{cdi} + k_{pi,i}i_{sdi} - \omega L_c i_{sqi})}{C_{DC}V_{DC,i}} + \frac{k_{pi,i}k_{p,p,i}i_{sdi}v_{sdi}}{C_{DC}V_{DC,i}} & \frac{(-v_{cqi} + k_{pi,i}i_{sqi} + \omega L_c i_{sdi})}{C_{DC}V_{DC,i}} + \frac{k_{pi,i}k_{p,p,i}i_{sdi}v_{sqi}}{C_{DC}V_{DC,i}} & \frac{(v_{cdi}i_{sdi} + v_{cqi}i_{sqi})}{C_{DC}V_{DC,i}^2} & \frac{-i_{sdi}}{C_{DC}V_{DC,i}} & \frac{-i_{sqi}}{C_{DC}V_{DC,i}} & \frac{-i_{sdi}k_{pi,i}}{C_{DC}V_{DC,i}} & \frac{-i_{sqi}k_{pi,i}}{C_{DC}V_{DC,i}} \\ -k_{ii,i} - k_{ii,i}k_{p,p,i}v_{sdi} & -k_{ii,i}k_{p,p,i}v_{sqi} & 0 & 0 & 0 & k_{ii,i} & 0 \\ 0 & -k_{ii,i} & 0 & 0 & 0 & 0 & k_{ii,i} \\ -k_{i,p,i}v_{sdi} & -k_{i,p,i}v_{sqi} & 0 & 0 & 0 & 0 & 0 \\ 0 & 0 & 0 & 0 & 0 & 0 & 0 \end{bmatrix}$$

for $P_s - v_s$ control mode of VSC i

$$A_{vsc1} = \begin{bmatrix} -\frac{(R_c + k_{pi,i})}{L_c} & 0 & \frac{k_{pi,i}k_{p,DC,i}}{L_c} & \frac{1}{L_c} & 0 & -\frac{k_{pi,i}}{L_c} & 0 \\ 0 & -\frac{(R_c + k_{pi,i})}{L_c} & 0 & 0 & \frac{1}{L_c} & 0 & \frac{k_{pi,i}}{L_c} \\ \frac{(-v_{cdi} + k_{pi,i}i_{sdi} - \omega L_c i_{sqi})}{C_{DC}V_{DC,i}} & \frac{(-v_{cqi} + k_{pi,i}i_{sqi} + \omega L_c i_{sdi})}{C_{DC}V_{DC,i}} & \frac{(v_{cdi}i_{sdi} + v_{cqi}i_{sqi} - k_{p,dc,i}k_{pi,i}V_{DC,i}i_{sdi})}{C_{DC}V_{DC,i}^2} & \frac{-i_{sdi}}{C_{DC}V_{DC,i}} & \frac{-i_{sqi}}{C_{DC}V_{DC,i}} & \frac{i_{sdi}k_{pi,i}}{C_{DC}V_{DC,i}} & \frac{-i_{sqi}k_{pi,i}}{C_{DC}V_{DC,i}} \\ -k_{ii,i} & 0 & k_{ii,i}k_{p,DC,i} & 0 & 0 & -k_{ii,i} & 0 \\ 0 & -k_{ii,i} & 0 & 0 & 0 & 0 & k_{ii,i} \\ 0 & 0 & -k_{i,DC,i} & 0 & 0 & 0 & 0 \\ 0 & 0 & 0 & 0 & 0 & 0 & 0 \end{bmatrix}$$

for $V_{DC} - v_s$ control mode of VSC i

(B.20)

A_{vsc2} matrix

$$A_{vsc2}=\begin{bmatrix} -\frac{k_{pi,i}k_{p,p,i}i_{sdi}}{L_c} & -\frac{k_{pi,i}k_{p,p,i}i_{sqi}}{L_c} \\ -\frac{k_{pi,i}k_{p,q,i}i_{sqi}}{L_c} & \frac{k_{pi,i}k_{p,q,i}i_{sdi}}{L_c} \\ \frac{(k_{pi,i}k_{p,p,i}i_{sdi}^2+k_{pi,i}k_{p,q,i}i_{sqi}^2)-i_{sdi}}{C_{DC}V_{DC,i}} & \frac{(k_{pi,i}k_{p,p,i}i_{sdi}i_{sqi}-k_{pi,i}k_{p,q,i}i_{sdi}i_{sqi})-i_{sqi}}{C_{DC}V_{DC,i}} \\ -k_{ii,i}k_{p,p,i}i_{sdi} & -k_{ii,i}k_{p,p,i}i_{sqi} \\ -k_{ii,i}k_{p,q,i}i_{sqi} & k_{ii,i}k_{p,q,i}i_{sdi} \\ -k_{i,p,i}i_{sdi} & -k_{i,p,i}i_{sqi} \\ k_{i,q,i}i_{sqi} & k_{i,q,i}i_{sdi} \end{bmatrix}$$

for $P_s - Q_s$ control mode of VSC i

$$A_{vsc2}=\begin{bmatrix} 0 & 0 \\ -\frac{k_{pi,i}k_{p,q,i}i_{sqi}}{L_c} & \frac{k_{pi,i}k_{p,q,i}i_{sdi}}{L_c} \\ \frac{k_{pi,i}k_{p,q,i}i_{sqi}^2-i_{sdi}}{C_{DC}V_{DC,i}} & \frac{-k_{pi,i}k_{p,q,i}i_{sdi}i_{sqi}-i_{sqi}}{C_{DC}V_{DC,i}} \\ 0 & 0 \\ -k_{ii,i}k_{p,q,i}i_{sqi} & k_{ii,i}k_{p,q,i}i_{sdi} \\ 0 & 0 \\ k_{i,q,i}i_{sqi} & k_{i,q,i}i_{sdi} \end{bmatrix}$$

for $V_{DC} - Q_s$ control mode of VSC i

$$A_{vsc2}=\begin{bmatrix} -\frac{k_{pi,i}k_{p,p,i}i_{sdi}}{L_c} & -\frac{k_{pi,i}k_{p,p,i}i_{sqi}}{L_c} \\ -\frac{k_{pi,i}k_{p,ac,i}v_{sdi}}{L_c\left|v_{s,i}\right|} & -\frac{k_{pi,i}k_{p,ac,i}v_{sqi}}{L_c\left|v_{s,i}\right|} \\ -\frac{(i_{sdi}\left|v_{s,i}\right|-k_{pi,i}k_{p,ac,i}i_{sqi}v_{sdi})}{C_{DC}V_{DC,i}\left|v_{s,i}\right|}+\frac{k_{pi,i}k_{p,p,i}i_{sdi}^2}{C_{DC}V_{DC,i}} & -\frac{(i_{sqi}\left|v_{s,i}\right|-k_{pi,i}k_{p,ac,i}i_{sqi}v_{sqi})}{C_{DC}V_{DC,i}\left|v_{s,i}\right|}+\frac{k_{pi,i}k_{p,p,i}i_{sdi}i_{sqi}}{C_{DC}V_{DC,i}} \\ -k_{ii,i}k_{p,p,i}i_{sdi} & -k_{ii,i}k_{p,p,i}i_{sqi} \\ -\frac{k_{ii,i}k_{p,ac,i}v_{sdi}}{\left|v_{s,i}\right|} & -\frac{k_{ii,i}k_{p,ac,i}v_{sqi}}{\left|v_{s,i}\right|} \\ -k_{i,p,i}i_{sdi} & -k_{i,p,i}i_{sqi} \\ -\frac{k_{i,ac,i}v_{sdi}}{\left|v_{s,i}\right|} & -\frac{k_{i,ac,i}v_{sqi}}{\left|v_{s,i}\right|} \end{bmatrix}$$

for $P_s - v_s$ control mode of VSC i

$$A_{vsc2}=\begin{bmatrix} 0 & 0 \\ -\frac{k_{pi,i}k_{p,ac,i}v_{sdi}}{L_c\left|v_{s,i}\right|} & -\frac{k_{pi,i}k_{p,ac,i}v_{sqi}}{L_c\left|v_{s,i}\right|} \\ -\frac{(i_{sdi}\left|v_{s,i}\right|-k_{pi,i}k_{p,ac,i}i_{sqi}v_{sdi})}{C_{DC}V_{DC,i}\left|v_{s,i}\right|} & -\frac{(i_{sqi}\left|v_{s,i}\right|-k_{pi,i}k_{p,ac,i}i_{sqi}v_{sqi})}{C_{DC}V_{DC,i}\left|v_{s,i}\right|} \\ 0 & 0 \\ -\frac{k_{ii,i}k_{p,ac,i}v_{sdi}}{\left|v_{s,i}\right|} & -\frac{k_{ii,i}k_{p,ac,i}v_{sqi}}{\left|v_{s,i}\right|} \\ 0 & 0 \\ -\frac{k_{i,ac,i}v_{sdi}}{\left|v_{s,i}\right|} & -\frac{k_{i,ac,i}v_{sqi}}{\left|v_{s,i}\right|} \end{bmatrix}$$

for $V_{DC} - v_s$ control mode of VSC i

(B.21)

A_{vsc3} matrix

$$A_{vsc3} = \begin{bmatrix} 0 & 0 & \dfrac{1}{C_{DC}} & 0 & 0 & 0 & 0 \end{bmatrix}^T \text{ for all VSC control modes} \tag{B.22}$$

$$W_{DC} = \begin{bmatrix} 1 & 0 & -1 & 0 \\ 0 & 1 & 0 & -1 \\ 0 & 0 & 1 & -1 \end{bmatrix} \tag{B.23}$$

for four-terminal VSC-HVDC system (from DC bus : 1, to DC bus : −1)

R_{DC}, L_{DC} : DC grid resistance and inductance matrix

C. SYSTEM DATA

Table C.1. Transmission line data of Base Case system

From bus	*To bus*	*R* [*p.u.*]	*X* [*p.u.*]	*Y/2* [*p.u.*]
1	11	0	0.0182	0
2	12	0	0.0116	0
3	13	0	0.0212	0
4	14	0	0.0116	0
5	15	0	0.0212	0
6	16	0	0.0116	0
7	17	0	0.0116	0
8	18	0	0.0182	0
9	19	0	0.0182	0
10	20	0	0.0255	0
50	48	0	0.0255	0
51	49	0	0.0255	0
22	38	0	0.0233	0
24	39	0	0.0117	0
27	40	0	0.0117	0
30	41	0	0.0117	0
33	42	0	0.0117	0
34	43	0	0.0233	0
25	44	0	0.0233	0
28	45	0	0.0233	0
31	46	0	0.02333	0
36	18	0	0.0311	0
37	19	0	0.0311	0
20	47	0	0.0311	0
11	21	0.00184	0.0427	0.0861
21	22	0.00115	0.0267	0.0538
21	23	0.00184	0.0427	0.0861
22	24	0.000920	0.0217	0.0430
23	24	0.00115	0.0267	0.0538
25	23	0.00184	0.0427	0.0861
12	13	0.000575	0.0136	0.108
13	25	0.000575	0.0136	0.108
25	26	0.000920	0.0217	0.0430
26	27	0.000575	0.0136	0.108

From bus	*To bus*	*R* [*p.u.*]	*X* [*p.u.*]	*Y/2* [*p.u.*]
27	24	0.00138	0.0320	0.0646
28	26	0.000920	0.0214	0.0430
14	15	0.000575	0.0134	0.108
15	28	0.000575	0.0134	0.108
28	29	0.000920	0.0214	0.0430
29	30	0.000575	0.0134	0.108
30	27	0.000920	0.0214	0.0430
31	29	0.000920	0.0214	0.0430
33	30	0.00138	0.0320	0.0646
31	32	0.00184	0.0427	0.0861
32	33	0.00115	0.0267	0.0538
35	32	0.00184	0.0427	0.0861
35	34	0.00115	0.0267	0.0538
34	33	0.000920	0.0214	0.0430
17	31	0.00115	0.0267	0.215
36	17	0.00230	0.0534	0.108
37	36	0.00460	0.107	0.215
20	48	0.00460	0.107	0.215
48	49	0.00460	0.107	0.215
49	37	0.00460	0.107	0.215
19	18	0.0154	0.353	0.0620
47	19	0.0154	0.353	0.0620
16	35	0.000920	0.0214	0.172

Table C.2. Synchronous generator data

Generator	X_d [*p.u.*]	X_d' [*p.u.*]	X_d'' [*p.u.*]	X_q [*p.u.*]	X_q' [*p.u.*]	X_q'' [*p.u.*]	X_l [*p.u.*]	T_d' [*sec*]	T_d'' [*sec*]
G1	1.70	0.350	0.250	1.70	0.350	0.250	0.225	4.90	0.0420
G2	1.70	0.380	0.280	1.70	0.380	0.280	0.252	6.75	0.0410
G3	1.20	0.350	0.260	0.720	0.350	0.260	0.234	8.96	0.0670
G4	1.70	0.350	0.250	1.70	0.350	0.250	0.225	4.90	0.0420
G5	1.20	0.350	0.260	0.720	0.350	0.260	0.234	8.96	0.0670
G6	1.70	0.350	0.250	1.70	0.350	0.250	0.225	4.90	0.0420
G7	1.70	0.380	0.280	1.70	0.380	0.280	0.252	6.75	0.0410
G8	1.70	0.350	0.250	1.70	0.350	0.250	0.225	4.90	0.0420
G9	1.70	0.350	0.250	1.70	0.350	0.250	0.225	4.90	0.0420
G10	1.70	0.350	0.250	1.70	0.350	0.250	0.225	4.90	0.0420

Generator	T_q' [*sec*]	T_q'' [*sec*]	R [*p.u.*]	K_{GOV} [*p.u.*]	T_{GOV} [*sec*]	K_{AVR} [*p.u.*]	T_{AVR} [*sec*]	D [*p.u.*]	H [*sec*]	***Rated capacity*** [*MVA*]
G1	0.981	0.0420	0	20.0	2.00	5.00	0.500	0	4.00	8240
G2	1.35	0.0420	0	20.0	2.00	5.00	0.500	0	4.00	12940
G3	1.07	0.0420	0	20.0	2.00	5.00	0.500	0	5.00	7060
G4	0.981	0.0420	0	20.0	2.00	5.00	0.500	0	4.00	12940
G5	1.07	0.0420	0	20.0	2.00	5.00	0.500	0	5.00	7060
G6	0.981	0.0420	0	20.0	2.00	5.00	0.500	0	4.00	12940
G7	1.35	0.0420	0	20.0	2.00	5.00	0.500	0	4.00	12940
G8	0.981	0.0420	0	20.0	2.00	5.00	0.500	0	4.00	8240
G9	0.981	0.0420	0	20.0	2.00	5.00	0.500	0	4.00	8240
G10	0.981	0.0420	0	20.0	2.00	5.00	0.500	0	4.00	5880

Table C.3. Generator types, fuel cost coefficients, and power production constraints

Generator	***Type***	***Fuel cost coefficients***			***Active power production* [MW]**	***Active power production limit* [MW]**	
		C_i [JPY / hour]	**B_i [JPY / MW × hour]**	**A_i [JPY / MW^2 × hour]**		***min***	***max***
G1	Thermal (LNG)	1170000	2400	0.04	*controllable*	140	7000
G2	Nuclear				11000		
G3	Pumped-storage hydro				5630		
G4	Thermal (coal)	6050000	400	0.063	*controllable*	330	11000
G5	Pumped-storage hydro				5800		
G6	Thermal (coal)	6050000	400	0.063	*slack*	330	11000
G7	Nuclear				11000		
G8	Thermal (oil)	2600000	5000	0.038	*controllable*	175	7000
G9	Thermal (oil)	2600000	5000	0.038	*controllable*	175	7000
G10	Thermal (oil)	2000000	5000	0.005	*controllable*	100	5000